

PERFORMANCE ENHANCEMENT TECHNIQUES FOR MICROSTRIP SQUARE RING ANTENNAS

By

Saeed Iftakhar Reza Latif

A Thesis

Submitted to the Faculty of Graduate Studies
in Partial Fulfillment of the Requirements
for the Degree of

DOCTOR OF PHILOSOPHY

**Department of Electrical and Computer Engineering
The University of Manitoba
Winnipeg, Manitoba, Canada**

© November, 2008

THE UNIVERSITY OF MANITOBA
FACULTY OF GRADUATE STUDIES

COPYRIGHT PERMISSION

Performance Enhancement Techniques for Microstrip Square Ring Antennas

BY

Saeed Iftakhar Reza Latif

**A Thesis/Practicum submitted to the Faculty of Graduate Studies of The University of
Manitoba in partial fulfillment of the requirement of the degree**

Of

Doctor of Philosophy

Saeed iftakhar Reza latif © 2008

Permission has been granted to the University of Manitoba Libraries to lend a copy of this thesis/practicum, to Library and Archives Canada (LAC) to lend a copy of this thesis/practicum, and to LAC's agent (UMI/ProQuest) to microfilm, sell copies and to publish an abstract of this thesis/practicum.

This reproduction or copy of this thesis has been made available by authority of the copyright owner solely for the purpose of private study and research, and may only be reproduced and copied as permitted by copyright laws or with express written authorization from the copyright owner.

Dedicated to the memory of

My parents

ABSTRACT

This thesis discusses microstrip square ring antenna, a miniaturized antenna, which is one of the basic shapes of its class. Singly fed stacked square ring antennas are presented for circular polarization (CP), which have not been studied before. Narrow CP bandwidth is a common problem for single-feed square ring antennas, and in this thesis, several perturbation schemes are used in stacked square rings to obtain a wider axial ratio bandwidth. A novel hybrid perturbation scheme is investigated for wideband CP stacked square ring antennas, which has the capability of providing wide angular coverage in the upper hemisphere, particularly desirable for global positioning systems (GPS).

The inner slot area of the square ring antenna is utilized by employing another smaller square ring, thus having three resonators in two layers to be operated at multiple frequencies, more specifically, at three frequencies. Capacitive feeding is used to excite the rings, which enables to increase the slot size, thus miniaturize the antenna.

Multi-frequency operation is also obtained from single-layer probe-fed square ring antenna by loading it with a gap or slit. Two unloaded modes are excited around the dominant TM_{11} mode of the square ring, equally spaced on the spectrum. To excite these multiple modes, the loading has to be symmetric on one arm, however the excitation has to be off-centered on another arm. These modes are investigated in greater detail with a parametric study. Simulation results are confirmed by measurements.

By choosing the location of the loading on vertical or horizontal arm, the polarization of each mode can be controlled. One of the loaded mode frequencies is much lower than the dominant mode frequency of the square ring, indicating a miniaturization to a great extent. The inner slot of the loaded square ring antenna is modified to further lower the loaded mode frequency. However, poor gain and efficiency are the main problems of such miniaturized antennas, because of high ohmic losses.

Using a planar laminated conductor system, it is shown that using multiple laminated conductors, instead of a single conductor, losses can be reduced. The same concept is used in miniaturized square ring antennas in order to reduce ohmic losses. This enhances the gain of these antennas significantly. Experimental investigations are conducted to confirm the simulated results.

Acknowledgements

I would like to express my deep sense of appreciation, heartiest respect and gratitude to my supervisor Professor Lotfollah Shafai for his scholastic advice, valuable guidance, enthusiasm, and continuous encouragement. I am indebted to him for his kindness and patience during numerous discussions for the thesis work and during my study at the University of Manitoba. I have to acknowledge that, because of his constant educational, moral and financial support, my endeavor to obtain the highest academic degree has come to a success.

I am thankful to my Ph.D. advisory committee members: Dr. S. Noghanian and Dr. P. N. Shivakumar for their valuable suggestions and comments, and for their time and effort. I would also like to thank the external examiner Dr. Rodney Vaughan from Simon Fraser University to serve on the examining committee. His comments and valuable suggestions have improved the thesis.

I am also thankful to Nandaka Jayasekera, Dr. Malcolm Ng Kehn, Dr. Alireza Forozoosh, Mehran Fallah-Rad, Zahra Allahgholipour, Ali Momen Mehrabani, Mohammad Qudrat-E-Maula Alireza Motieifar, Farshad Kaymaram, Abdelhalim Mohamed and many other friends in the research group and in the department for their kind help and advice during different stages of this work.

I would like to thank several professors in the department of Electrical and Computer Engineering at the University of Manitoba: Dr. Cyrus Shafai, Dr. Greg Bridges, Dr. I. M. R. Ciric, Dr. Vladimir Okhmatovski, Dr. Behzad Kordi, Dr. Shahin

Filizadeh, and Dr. E. Hossain. I learnt engineering and discipline from them, and received guidance for professional development during my study at the University of Manitoba.

Special thanks to Mr. B. Tabachnick and Mr. Cory Smit for their generous help for the prototype fabrication and experimental measurements. Extended thanks to Ms. Shelly Girardin for her kind help whenever it was required.

It is also my pleasure to thank all other support staff members in the department of Electrical and Computer Engineering at the University of Manitoba, especially Mr. Mount-First Ng, and Mr. Guy Jonatschick for their kind help and cooperation when it was needed.

This work would not have been possible without the continual support, encouragement and understanding of my family: my brothers, my only sister, my extended family members, my friends, and above all, my beloved wife, Humaira Khair. I am truly grateful to my wife, for her kind support and generous love, and for taking good care of our only son when I was busy.

Finally, I would like to remember my parents at this special time of my life. They passed away; however, their memories are still woven in my heart. They would be the most happiest to see this achievement of mine. I am dedicating this thesis to their memory.

Table of Contents

Abstract	i
Acknowledgements	iii
Table of Contents	v
List of Symbols	x
List of Figures	xii
List of Tables	xxvi
 CHAPTER ONE	
Introduction	1
1.1 Motivation	1
1.2 Objective of the research	2
1.3 Organization of the thesis	7
 CHAPTER TWO	
Background Study: Antenna Miniaturization and Microstrip Ring	
Antennas	9
2.1 Introduction	9
2.2 Antenna miniaturization techniques	9
2.2.1 Loading with lumped elements	10

2.2.2 Loading with dielectric material	10
2.2.3 Using short circuits	11
2.2.4 Modifying antenna geometry	13
2.3 Major disadvantages of miniaturized antennas	14
2.4 Microstrip ring antennas	18
2.5 Conclusion	21

CHAPTER THREE

Stacked Square Ring Antennas for Wideband Circular Polarization	23
3.1 Introduction	23
3.2 Circular polarization from DLSRA with corner perturbation	24
3.2.1 Microstrip dual layer square-ring antenna (DLSRA)	24
3.2.2 Effect of perturbing either parasitic or driven ring	25
3.2.3 Broadband CP performance from the DLSRA by negative perturbation	28
3.2.4 CP from DLSRA by outward positive perturbation	31
3.2.5 CP from DLSRA by inward positive perturbation	34
3.2.6 A novel approach: CP from DLSRA by hybrid perturbation	36
3.3 Effects of finite ground plane on CP performance of the DLSRA	42
3.3.1 Ground plane size	42
3.3.2 Asymmetric antenna position on the ground plane	45
3.4 Experimental study	48
3.5 Conclusion	54

CHAPTER FOUR

Square Ring Antenna for Multi-Frequency Operation	55
4.1 Introduction	55
4.2 General design guideline for multi-frequency operation from stacked square ring antenna	55
4.3 Confirmation by Ansoft HFSS	62
4.4 A design for tri-frequency global positioning system (GPS)	64
4.5 Conclusion	71

CHAPTER FIVE

Loaded Square Ring Antenna	73
5.1 Introduction	73
5.2 Gap loaded square ring antenna	74
5.2.1 Vertical gap loading	76
5.2.2 Horizontal gap loading	81
5.3 Parametric study of the loaded square ring antenna	85
5.3.1 Effect of probe position (X_F , Y_F)	85
5.3.2 Effect of substrate parameters	87
5.3.3 Effect of ring width (W)	89
5.3.4 Effect of gap length (g)	91
5.4 Design guideline	92
5.5 Antenna miniaturization by loading	94

5.6 Experimental study	96
5.7 Modified gap-loaded square ring antenna	99
5.8 Conclusion	103

CHAPTER SIX

Gain Improvement of Miniaturized Square Ring Antennas	105
6.1 Introduction	105
6.2 Multi-layered planar conductor to reduce loss	107
6.3 Multi-layered patches to enhance miniaturized antenna gain	123
6.3.1 Square ring antenna	124
6.3.2 H-shaped miniaturized antenna	127
6.3.3 Miniaturized loaded square ring antenna	130
6.4 Choice of laminating dielectric material	134
6.5 Experimental study	138
6.6 Conclusion	142

CHAPTER SEVEN

Conclusion	144
7.1 Summary	144
7.2 Future research	148

Appendices	150
Appendix A: Glossary of Important Terms	150
Appendix B: MATLAB code to calculate the power lost in single lossy material with normal incidence of uniform plane wave	153
Appendix C: MATLAB code to calculate the power lost in multiple laminated conducting materials with normal incidence of uniform plane wave	155
Appendix D: Skin Depth for Different Conductivity	158
Appendix E: Reduction in Antenna Gain Due to Mismatch Loss	160
References	161

List of Symbols

ϵ_0	Free-space permittivity
ϵ_{eff}	Effective dielectric constant
ϵ_r	Relative permittivity of the dielectric material
ϵ_m	Relative permittivity of the conducting material
ϵ_l	Relative permittivity of the laminating dielectric material
f	Frequency
λ	Wavelength
λ_0	Wave length in free space
λ_d	Wave length in the dielectric substrate
G	Gain of the antenna
Q	Quality factor of the antenna
J_s	Current density
E	Electric Field
H	Magnetic Field
k	Propagation constant
k_0	Propagation constant in the free-space
k_l	Propagation constant in the laminating dielectric material
k_m	Propagation constant in the metal conductor
t_m	Thickness of the conducting material
t_l	Thickness of the laminating dielectric material
t_c	Thickness of the laminated conductor

μ_0	Permeability of air
μ_m	Relative permeability of the conducting material
μ_l	Relative permeability of the laminating dielectric material
σ	Conductivity
σ_m	Conductivity of the conducting material
σ_l	Conductivity of the laminating dielectric material
δ	Skin depth
α	Attenuation constant
η	Wave impedance

List of Figures

CHAPTER TWO

- Fig. 2.1:** Loading techniques: (a) inductive, (b) capacitive (c) conductive. 10
- Fig. 2.2:** (a) Monopole, and (b) dielectric loaded monopole. h is the height of the monopole, λ_o is the free space wavelength, ϵ_r and ϵ_{eff} are the relative and effective dielectric constant of the substrate material, respectively. 11
- Fig. 2.3:** (a) A half-wavelength microstrip antenna, and (b) a shorted microstrip antenna: λ_o is the free space wavelength, and ϵ_r and ϵ_{eff} are the relative and effective dielectric constant of the substrate material, respectively. 12
- Fig. 2.4:** (a) The monopole antenna, length: $L \approx \lambda_o/4$, (b) the inverted-L antenna, length: $L_1 + L_2 \approx \lambda_o/4$, and (c) the inverted-F antenna, length $L_3 + L_4 < \lambda_o/4$. λ_o is the free space wavelength. 13
- Fig. 2.5:** Current flow path on (a) a microstrip patch antenna, and (b) a patch antenna with H-shaped slot. ϵ_r and ϵ_{eff} are the relative and effective dielectric constant of the substrate material, respectively. 14
- Fig. 2.6:** Imaginary spherical boundary fully enclosing the antenna. 16
- Fig. 2.7:** (a) Square, (b) annular, and (c) triangular ring antennas derived from regular- shaped patch antennas. 19
- Fig. 2.8:** Geometry of a (a) square loop, (b) square ring and (c) regular square patch. $\lambda_{eff} = \frac{\lambda_o}{\sqrt{\epsilon_{eff}}}$ is the wavelength in the dielectric, and ϵ_r and ϵ_{eff}

are the relative and effective dielectric constant of the substrate material, respectively. 19

CHAPTER THREE

Fig. 3.1: (a) 3-D view and (b) side view of the dual-layer square-ring antenna (DLSRA), and (c) its return loss. 25

Fig. 3.2: Geometry of the driven and parasitic rings of the DLSRA with negative perturbation. 27

Fig. 3.3: Simulated axial ratio of the DLSRA with perturbing either parasitic ring or driven ring. 27

Fig. 3.4: (a) Return loss plot and (b) axial ratio and RHCP gain vs. frequency plot of the DLSRA with negative perturbation [Fig. 3.2]. The antenna parameters are tabulated in Table 3.2. 30

Fig. 3.5: Simulated CP gain patterns in the (a) $\phi = 0^\circ$ and (b) $\phi = 90^\circ$ planes, at 1.575 GHz, of the DLSRA antenna with negative perturbation [Fig. 3.2]. The antenna parameters are tabulated in Table 3.2. 31

Fig. 3.6: (a) Geometry of the driven and parasitic rings of the DLSRA with outward positive perturbation, and its simulated (b) return loss plot, and (c) axial ratio and RHCP gain vs. frequency plot. The antenna parameters are tabulated in Table 3.2. 33

Fig. 3.7: (a) Geometry of the driven and parasitic rings of the DLSRA with inward positive perturbation, and its simulated (b) return loss plot, and (c) axial ratio and RHCP gain vs. frequency plot. The antenna parameters are tabulated in Table 3.2. 35

Fig. 3.8: (a) Geometry of the DLSRA with hybrid perturbation, and its simulated (b) return loss plot, and (c) axial ratio and RHCP gain vs. frequency plot. The antenna dimensions are tabulated in Table 3.2. 39

Fig. 3.9: The variations of axial ratio with elevation angle, in the $\phi = 0^\circ$ plane, for the DLSRA with positive perturbation (inward and outward), negative perturbation and hybrid perturbation, at 1.556 GHz. 40

Fig. 3.10: The variation of axial ratio with frequency, due to different ground plane sizes for the DLSRA antenna with positive perturbation in Fig. 3.6(a). Antenna parameters (in mm) are: $L_1 = 59$, $L_2 = 37$, $L_3 = 44.5$, $L_4 = 14.5$, $p_a = 5$, $q_a = 6$, $\epsilon_r = 3.2$, $h_1 = 1.6$, $h_2 = 11$. Gr=80 means ground plane size = $80 \times 80 \text{ mm}^2$, Gr=100 means ground plane size = $100 \times 100 \text{ mm}^2$ and so on. 43

Fig. 3.11: The effects of finite ground plane sizes on the (a) axial ratio and (b) RHCP gain of the DLSRA antenna with positive perturbation in Fig. 3.6(a). Antenna parameters are mentioned in Table 3.3. Gr=80 means ground plane size = $80 \times 80 \text{ mm}^2$, Gr=100 means ground plane size = $100 \times 100 \text{ mm}^2$ and so on. 44

Fig. 3.12: Antenna geometry with the ground plane in order to study the effects of asymmetric antenna position on the ground plane on the axial ratio of the DLSRA with positive perturbation, Fig. 3.6(a). Antenna parameters (in mm) are: $L_1 = 59$, $L_2 = 37$, $L_3 = 44.9$, $L_4 = 14.9$, $P_a = 5$, $q_a = 6$, $\epsilon_r = 3.2$, $h_1 = 1.6$, $h_2 = 12.8$. Ground plane size = $100 \times 100 \text{ mm}^2$. 46

Fig. 3.13: The effects of asymmetric antenna position on the ground plane on the axial ratio of the DLSRA with positive perturbation, in Fig. 3.12: (a) when asymmetric about y -axis, with $X_g = 0$, (b) when asymmetric about x -axis, with $Y_g = 0$, and (c) when asymmetric about both x - and y - axes. 47

Fig. 3.14: Comparison between simulated and measured (a) return loss and (b) axial ratio and RHCP gain of the DLSRA, with positive perturbation [Fig. 3.6(a)]. The antenna parameters are (in mm): $\epsilon_r = 3.2$, $h_1 = 1.6$, $h_2 = 11$, $L_1 = 59$, $L_2 = 37$, $L_3 = 44.5$, $L_4 = 14.5$, $p_a = 5$, $q_a = 6$. The finite ground plane size is $160 \times 160 \text{ mm}^2$. 50

Fig. 3.15: The measured gain patterns in (a) $\phi = 0^\circ$, and (b) $\phi = 90^\circ$ planes at 1.56 GHz of the DLSRA, with positive perturbation [Fig. 3.6(a)]. 51

Fig. 3.16: Comparison between simulated and measured (a) return loss and (b) axial ratio and RHCP gain of the DLSRA, with hybrid perturbation [Fig. 3.8(a)]. The antenna parameters are (in mm): $\epsilon_r = 3.2$, $h_1 = 1.6$, $h_2 = 11$, $L_1 = 59$, $L_2 = 39.2$, $L_3 = 44.7$, $L_4 = 14.7$, $p_c = 5$, $q_a = 6$. The finite ground plane size is $160 \times 160 \text{ mm}^2$. 52

Fig. 3.17: Measured and simulated axial ratios with elevation angle, in the $\phi = 0^\circ$ plane, of the DLSRA with hybrid perturbations. 53

CHAPTER FOUR

Fig. 4.1: Geometry of the proposed antenna with capacitively-fed multiple square rings for multi-frequency operation: (a) 3-D view, (b) side view, (c) top and bottom rings. 58

Fig. 4.2: Simulated scattering parameters of the antenna in Fig. 4.1, showing three resonances and good isolation between two ports.	59
Fig. 4.3: Radiation patterns at $f_1 = 1.161$ GHz in two principal planes of the antenna in Fig. 4.1 with design parameters mentioned in Table 4.1.	61
Fig. 4.4: Radiation patterns at $f_2 = 1.219$ GHz in two principal planes of the antenna in Fig. 4.1 with design parameters mentioned in Table 4.1.	61
Fig. 4.5: Radiation patterns at 1.56 GHz in two principal planes of the antenna in Fig. 4.1 with design parameters mentioned in Table 4.1.	62
Fig. 4.6: Simulated scattering parameters, using Ansoft HFSS (Finite Element Method-based software package), of the antenna in Fig. 4.1.	63
Fig. 4.7: Return loss of the antenna in Fig. 4.1 with the antenna parameters mentioned in Table 4.3.	67
Fig. 4.8: Dual-feed arrangement of the multiple square ring antenna [Fig. 4.1] to obtain circular polarization for GPS system.	68
Fig. 4.9: Axial ratio of the multiple square ring antenna with orthogonal capacitive feeding. The antenna configuration is shown in Fig. 4.8 and antenna parameters are mentioned in Table 4.3.	68
Fig. 4.10: CP gains of the multiple square ring antenna with orthogonal capacitive feeding. The antenna configuration is shown in Fig. 4.8 and antenna parameters are mentioned in Table 4.3.	69

Fig. 4.11: CP gains of the multiple square ring antenna with orthogonal capacitive feeding at 1176 MHz in two principal planes. The antenna configuration is shown in Fig. 4.8 and antenna parameters are mentioned in Table 4.3. 70

Fig. 4.12: CP gains of the multiple square ring antenna with orthogonal capacitive feeding at 1227 MHz in two principal planes. The antenna configuration is shown in Fig. 4.8 and antenna parameters are mentioned in Table 4.3. 70

Fig. 4.13: CP gains of the multiple square ring antenna with orthogonal capacitive feeding at 1575 MHz in two principal planes. The antenna configuration is shown in Fig. 4.8 and antenna parameters are mentioned in Table 4.3. 71

CHAPTER FIVE

Fig. 5.1: (a) Geometry of the square ring antenna on an infinite ground plane, and its (b) return loss plot and (c) current distribution. The antenna parameters are: $L_1 = 35$ mm, $L_2 = 17.5$ mm, $W = 8.75$ mm. Substrate parameters: $\epsilon_r = 2.5$, $h = 1.57$ mm, and $\tan\delta = 0.0019$. Probe position: $X_F = -10.5$ mm, $Y_F = 0$ mm. 75

Fig. 5.2: Radiation patterns of the square ring antenna at $f_u = 2.082$ GHz. The antenna parameters are given in the caption of Fig. 5.1. 77

Fig. 5.3: (a) Geometry of the loaded square ring antenna on an infinite ground plane with a vertical gap, (b) its return loss plot, and current distributions of the antenna at (c), f_{L1} , (d) f_u , (e) f_{L2} . The antenna parameters are: $L_1 = 35$ mm, $L_2 = 17.5$ mm, $W = 8.75$ mm. Gap size, $g = 1$ mm. Substrate parameters: $\epsilon_r = 2.5$, $h = 1.57$ mm, and $\tan\delta = 0.0019$. Probe position: $X_F = -10.5$ mm, $Y_F = 2.5$ mm. 78

Fig. 5.4: Radiation patterns of the loaded square ring antenna with a vertical gap at $f_{L1} = 1.043$ GHz. The antenna parameters are given in the caption of Fig. 5.3. 79

Fig. 5.5: Radiation patterns of the loaded square ring antenna with a vertical gap at $f_u = 2.086$ GHz. The antenna parameters are given in the caption of Fig. 5.3. 79

Fig. 5.6: Radiation patterns of the loaded square ring antenna with a vertical gap at $f_{L2} = 3.0$ GHz. The antenna parameters are given in the caption of Fig. 5.3. 80

Fig. 5.7: (a) Geometry of the loaded square ring antenna on an infinite ground plane with a horizontal gap, current distributions of the antenna at (b), f_{L1} , (d) f_u , (e) f_{L2} , and (e) its return loss plot. The antenna parameters are: $L_1 = 35$ mm, $L_2 = 17.5$ mm, $W = 8.75$ mm. Gap size, $g = 1$ mm. Substrate parameters: $\epsilon_r = 2.5$, $h = 1.57$ mm, and $\tan\delta = 0.0019$. Probe position: $X_F = -10.5$ mm, $Y_F = 2.5$ mm. 82

- Fig. 5.8:** Radiation patterns of the loaded square ring antenna with a horizontal gap at $f_{L1} = 1.043$ GHz. The antenna parameters are given in the caption of Fig. 5.7. 83
- Fig. 5.9:** Radiation patterns of the loaded square ring antenna with a horizontal gap at $f_u = 2.086$ GHz. The antenna parameters are given in the caption of Fig. 5.7. 83
- Fig. 5.10:** Radiation patterns of the loaded square ring antenna with a horizontal gap at $f_{L2} = 3.0$ GHz. The antenna parameters are given in the caption of Fig. 5.7. 84
- Fig. 5.11:** The effects of different probe locations on the impedance of the loaded mode frequency f_{L1} of the square ring antenna in Fig. 5.7(a): (a) varying Y_F with $X_F = -10.5$ mm. (b) varying X_F with $Y_F = 2.5$ mm. The antenna parameters are: $L_1 = 35$ mm, $L_2 = 17.5$ mm, $W = 8.75$ mm. Gap size, $g = 1$ mm. Substrate parameters: $\epsilon_r = 2.5$, $h = 1.57$ mm, and $\tan\delta = 0.0019$. 86
- Fig. 5.12:** The effects of varying ϵ_r on the frequency of the loaded square ring antenna in Fig. 5.7(a). The antenna parameters are the same as in the caption of Fig. 5.11. 87
- Fig. 5.13:** The effects of varying h on the loaded and unloaded mode frequencies of the loaded square ring antenna in Fig. 5.7(a). The antenna parameters are the same as in the caption of Fig. 5.11. 88

Fig. 5.14: Current distributions, at f_{L2} , of the loaded square ring antenna in Fig.

5.7(a) for (a) $h = 0.8$ mm and (b) $h = 10$ mm. The antenna parameters

are the same as in the caption of Fig. 5.11.

89

Fig. 5.15: The effects of varying width (W) on the return loss of the loaded

square ring antenna in Fig. 5.7(a). The antenna parameters are: $L_1 = 35$

mm, Gap size, $g = 1$ mm, substrate parameters: $\epsilon_r = 2.5$, $h = 1.57$ mm,

and $\tan\delta = 0.0019$. Probe location: $X_F = 10.5$ mm, $Y_F = 2.5$ mm.

90

Fig. 5.16: The effects of varying g on the return loss of the loaded square ring

antenna in Fig. 5.7(a), with $L_2 = 17.5$ mm. Other antenna parameters

are the same as in the caption of Fig. 5.15.

91

Fig. 5.17: Return loss plot of the gap-loaded annular ring antenna on an infinite

ground plane, with its geometry. The antenna parameters are: inner

diameter = 12 mm, outer diameter = 21 mm, probe position: $X_F = -15.5$

mm, $Y_F = 2$ mm, Foam substrate thickness = 0.8 mm.

94

Fig. 5.18: The simulated and measured return losses of the gap-loaded square

ring antenna in Fig. 5.7(a). Antenna parameters are: $L_1 = 35$ mm, $L_2 =$

17 mm, $W = 9$ mm, foam thickness, $h = 10$ mm, gap, $g = 2$ mm,

probe location: $X_F = 12.5$ mm, $Y_F = 1.5$ mm.

96

Fig. 5.19: Simulated and measured return loss plots of the square ring antenna

loaded with a horizontal gap at loaded mode frequency, $f_{L1} = 1.64$

GHz. The antenna parameters are (in mm): $L_1 = 34$, $L_2 = 17.1$, $W =$

8.45, $g = 2$. Foam substrate thickness, $h = 10$.

97

Fig. 5.20: (a) simulated and (b) measured gain patterns in the $\phi = 0^\circ$ plane of the square ring antenna loaded with a horizontal gap at loaded mode frequency, $f_{LI} = 1.64$ GHz. The antenna parameters are the same as in caption of Fig. 5.19. 98

Fig. 5.21: (a) simulated and (b) measured gain patterns in the $\phi = 90^\circ$ plane of the square ring antenna, loaded with a horizontal gap, at loaded mode frequency, $f_{LI} = 1.64$ GHz. The antenna parameters are the same as in caption of Fig. 5.19. 98

Fig. 5.22: Modified open square ring antenna geometries: antennas # (a) and (b) are from [23, 24]. For antenna # (c), $a = 2$ mm. 100

Fig. 5.23: Return losses of the modified open square ring antennas in Fig. 5.22. 101

Fig. 5.24: Gain patterns in two principal planes of the modified open square ring antenna [Antenna # (a), Fig. 5.22(a)]. 101

Fig. 5.25: Gain patterns in two principal planes of the modified open square ring antenna [Antenna # (a), Fig. 5.22(b)]. 102

Fig. 5.26: Gain patterns in two principal planes of the modified open square ring antenna [Antenna # (a), Fig. 5.22(c)]. 102

CHAPTER SIX

Fig. 6.1: Current distributions on the square ring antennas with wide and narrow strip widths, at their resonance frequencies. 106

Fig. 6.2: Planar lossy material with plane wave incidence. 107

- Fig. 6.3:** Power loss vs. frequency for the lossy material in Fig. 6.2 for thickness of $a = 200 \mu\text{m}$. 111
- Fig. 6.4:** Planar conductor with alternating laminating material with normal plane wave incidence: three layers. 112
- Fig. 6.5:** Planar conductor with alternating laminating material with normal plane wave incidence: ' n ' number of layers. 115
- Fig. 6.6:** Loss reduction due to the use of multiple laminated conductors instead of a single conducting layer, with $t_c = 20 \mu\text{m}$. Skin depth at 1 GHz is $50.3 \mu\text{m}$ for $\sigma_m = 10^5$. 121
- Fig. 6.7:** Loss reduction due to the use of many laminated conductor layers with smaller thickness of each layer: $\sigma_m = 10^3$, $t = 1 \text{ mm}$. Skin depth at 1 GHz is $503 \mu\text{m}$ for $\sigma_m = 10^3$. 122
- Fig. 6.8:** Loss reduction due to the use of many laminated conductor layers with smaller thickness of each layer: $\sigma_m = 10^5$, $t = 100 \mu\text{m}$. Skin depth at 1 GHz is $50.3 \mu\text{m}$ for $\sigma_m = 10^5$. 122
- Fig. 6.9:** Loss reduction due to the use of many laminated conductor layers with smaller thickness of each layer: $\sigma_m = 10^5$, $t = 300 \mu\text{m}$. Skin depth at 1 GHz is $50.3 \mu\text{m}$ for $\sigma_m = 10^5$. 123
- Fig. 6.10:** Geometry of the square-ring antenna on foam substrate: (a) top view, (b) side view. Antenna parameters: $L_1 = 60 \text{ mm}$, $W = 5 \text{ mm}$, $L_2 = 50$, $h = 1 \text{ mm}$. 125

- Fig. 6.11:** Side view of a square ring antenna on a foam substrate, (a) with a single solid conductor, (b) with multiple thin laminated conductor layers. 125
- Fig. 6.12:** Variations of the gain of the ring antenna in Fig. 6.10 for multiple laminated conductor layers at 1.41 GHz in the $\phi = 0^\circ$ plane: $t_c = 1 \mu\text{m}$. 126
- Fig. 6.13:** Variations of the gain of the ring antenna in Fig. 6.10 for multiple laminated conductor layers at 1.41 GHz in the $\phi = 0^\circ$ plane: $t_c = 3 \mu\text{m}$. 127
- Fig. 6.14:** Geometry of the H-shaped microstrip antenna, on a substrate having $\epsilon_r = 2.5$, $\tan \delta = 0.0019$ and $h_2 = 1.6 \text{ mm}$, with antenna dimensions. 128
- Fig. 6.15:** Gain patterns, in $\phi = 0^\circ$ plane, of the H-shaped antenna in Fig. 6.14 at 2 GHz, in order to calculate the conductor and dielectric losses. 129
- Fig. 6.16:** Gain patterns, in $\phi = 0^\circ$ plane, of the H-shaped antenna in Fig. 6.14 at 2 GHz, with multiple laminated conductor with $t_c = 0.5 \mu\text{m}$. 129
- Fig. 6.17:** Geometry of the modified loaded square ring antenna, on a substrate having $\epsilon_r = 2.5$, thickness = 0.79 mm, and $\tan \delta = 0.0019$. 130
- Fig. 6.18:** Gain patterns at 2.185 GHz, in the $\phi = 0^\circ$ plane, of the modified square ring antenna in Fig. 6.17, in order to calculate the conductor and dielectric losses. 131
- Fig. 6.19:** Variations of the gain at 2.185 GHz of the multi-layered modified loaded square ring antenna in Fig. 6.17, in the $\phi = 0^\circ$ plane: $t_c = 0.5 \mu\text{m}$. 133

Fig. 6.20: Variations of the gain, at 2.185 GHz in the $\phi = 0^\circ$ plane, of the ring antenna for multiple laminated conductor layers, with perfect electric conductor (PEC) and copper conductor: $t_c = 0.5 \mu\text{m}$. (a) 2 layers, (c) 3 layers and (e) 4 layers showing ohmic losses, and (b) 2 layers, (d) 3 layers and (f) 4 layers, with copper losses added to the gain. 133

Fig. 6.21: Variation on the return loss of the modified loaded square ring antenna with multiple laminated conductor layers, in Fig. 6.17, with different laminating dielectric material thickness, t_l . $\epsilon_r = 1$. 134

Fig. 6.22: Variation on the gain of the modified loaded square ring antenna with multiple laminated conductor layers, in Fig. 6.17, with different laminating dielectric material thickness, t_l . $\epsilon_r = 1$. 135

Fig. 6.23: Variation on the return loss of the modified loaded square ring antenna with multiple laminated conductor layers, in Fig. 6.17, with different laminating dielectric materials (varying ϵ_l). $t_l = 100 \mu\text{m}$. 136

Fig. 6.24: Variation on the gains of the modified loaded square ring antenna with multiple laminated conductor layers, in Fig. 6.17, with different laminating dielectric materials (ϵ_l). $t_l = 100 \mu\text{m}$. 137

Fig. 6.25: Simulated return loss plots of the modified loaded square ring antenna with multiple laminated conductor layers, in Fig. 6.17, with RT/Duroid 5880 as the laminating dielectric: thickness = $254 \mu\text{m}$, relative permittivity = 2.2, and $\tan\delta = 0.0009$. 140

Fig. 6.26: Simulated gain patterns of the modified loaded square ring antenna with multiple laminated conductor layers, in Fig. 6.17, with RT/Duroid 5880 as the laminating dielectric: thickness = 254 μm , relative permittivity = 2.2, and $\tan\delta = 0.0009$. 140

Fig. 6.27: Measured return losses of the modified loaded square ring antenna with multiple laminated conductor layers, in Fig. 6.17, with RT/Duroid 5880 as the laminating dielectric: thickness = 254 μm , relative permittivity = 2.2, and $\tan\delta = 0.0009$. 141

Fig. 6.28: Measured gain patterns of the modified loaded square ring antenna with multiple laminated conductor layers, in Fig. 6.17, with RT/Duroid 5880 as the laminating dielectric: thickness = 254 μm , relative permittivity = 2.2, and $\tan\delta = 0.0009$. 141

APPENDICES

Fig. A1: Microstrip patch antenna on a substrate with fringing electric field lines. 152

List of Tables

CHAPTER THREE

Table 3.1: DLSRA CP performance, obtained using corner perturbation in either driven or parasitic ring	28
Table 3.2: DLSRA antenna for CP: Optimized antenna parameters and simulated results (Foam height = 11 mm, Probe position: $X_F = 21$ mm, $Y_F = 0$)	41
Table 3.3: Positively perturbed DLSRA CP antenna [Fig. 3.6(a)] with finite ground plane: optimized antenna parameters and simulated results. Other antenna parameters: $L_1 = 59$ mm, $L_2 = 37$ mm, $p_a = 5$ mm, $q_a = 6$ mm	45
Table 3.4: Comparison of simulated and measured results of the stacked square ring antenna with hybrid perturbations	53

CHAPTER FOUR

Table 4.1: Design parameters for the antenna with multiple rings (Fig. 4.1) for tri-frequency operation	60
Table 4.2: Simulation results of the stacked square ring antenna for multi-frequency operation, Fig. 4.1, from two software packages: Ansoft Designer and Ansoft HFSS. Antenna parameters are mentioned in Table 4.1	63

Table 4.3: Multiple square ring antenna [Figs. 4.1] parameters for GPS frequencies	66
---	----

CHAPTER FIVE

Table 5.1: Polarization and accepted gain of unloaded square ring antenna. The antenna parameters are provided in the caption of Fig. 5.1	75
--	----

Table 5.2: Polarization and accepted gain of the square ring antenna loaded with a vertical gap. The antenna parameters are provided in the caption of Fig. 5.3	80
--	----

Table 5.3: Polarization and accepted gain of the square ring antenna loaded with a horizontal gap. The antenna parameters are provided in the caption of Fig. 5.7	84
--	----

Table 5.4: The effect of varying ring width (W) on f_{L1} of the square ring antenna in Fig. 5.7(a). The antenna parameters are mentioned in the caption of Fig. 5.15	90
--	----

Table 5.5: Performance properties of the modified open square ring antennas in Fig. 4.10 on infinite ground plane	103
--	-----

CHAPTER SIX

Table 6.1: Multiple laminated conductor layers to enhance the gain of the square ring antenna in Fig. 6.10 with $t_c = 1 \mu\text{m}$	126
--	-----

Table 6.2: Effects of multiple laminated conductor layers on the gain of the modified loaded square ring antenna in Fig. 6.17: $t_c = 0.5 \mu\text{m}$	132
Table 6.3: Laminated conductor thickness and the gain of the modified loaded square ring antenna in Fig. 6.17 for two-layer case with different laminating dielectric thickness t_l	135
Table 6.4: Laminated conductor thickness and the gain of the modified loaded square ring antenna in Fig. 6.17 for two-layer case with different laminating dielectric material (varying ϵ_l). $t_l = 100 \mu\text{m}$ and $t = 200 \mu\text{m}$.	138
Table 6.5: Simulated and measured return losses and gains of the modified loaded square ring antenna in Fig. 6.17, using multiple laminated conductors. Laminating dielectric: RT/Duroid 5880: $t_c = 254 \mu\text{m}$, $\epsilon_r = 2.2$, and $\tan\delta = 0.0009$.	143

APPENDICES

Table D.1: Skin depths for frequencies with $\sigma = 10$	158
Table D.2: Skin depths for frequencies with $\sigma = 10^2$	158
Table D.3: Skin depths for frequencies with $\sigma = 10^3$	158
Table D.4: Skin depths for frequencies with $\sigma = 10^4$	159
Table D.5: Skin depths for frequencies with $\sigma = 10^5$	159
Table D.6: Skin depths for frequencies with $\sigma = 10^6$	159
Table D.7: Skin depths for frequencies with $\sigma = 10^7$	159
Table E: Reduction in gain due to mismatch loss	160

CHAPTER ONE

Introduction

1.1 Motivation

Antennas are used in many applications such as wireless systems, mobile and satellite communications, microwave imaging and other biomedical applications, or remote sensing. Microstrip antennas are one of many antenna types, and are widely used in most applications, and therefore, have attracted the attention of researchers in industry and academia for the past few decades. Their most common shapes are rectangle, circle, and triangle. Besides these shapes, numerous geometries are possible that can also be chosen. However, microstrip antennas with common geometric shapes are easy to analyze mathematically, and their performances as antennas, such as, input impedance, radiation patterns and polarizations, can be predicted almost precisely. One reason for their popularity is small size.

The drastic size reduction of integrated circuits and other electronic components has enabled the design of miniaturized communication hardware, especially small mobile or hand-held units [1]. However, antenna engineers and researchers are still challenged with this trend of miniaturization. Though microstrip antennas are considered low profile, lightweight, low-cost, and compact [2, 3], their conventional geometries progressively appear somewhat large for modern small-sized wireless units [4]. In order to employ

microstrip antennas in miniaturized wireless units, researchers have applied the concept of small antennas and other innovative ideas. Perhaps the first variation of a square patch antenna is a square ring antenna, which has evolved from the square patch by removing a central metal portion from it. This resulting geometry is definitely a miniaturized version of the typical square patch antenna, since it will resonate at a frequency lower than the typical half-wavelength square patch antenna [5]. The square ring antenna is the topic of this thesis.

The square ring antenna was previously studied by Pedram and Shafai [5], and has been an attractive subject of research for the past decade. Its general properties and applications have been well documented in the literature, and will be discussed as the background study in the second chapter of this thesis. In an effort to better understand square ring antennas, a new study is carried out in this thesis. It provides new information on different aspects of these antennas like bandwidth, polarization, miniaturization, and gain enhancement.

1.2 Objective of the research

The main objectives of this research are two fold. First, to investigate microstrip square ring antennas beyond the research conducted so far, in order to contribute new knowledge and understanding of these antennas. Second, to enhance the performance of miniaturized versions of microstrip square ring antennas.

The microstrip square ring antenna is a miniaturized antenna, the resonant wavelength of which is approximately equal to the average circumferential ring length. Therefore, a $\lambda/4 \times \lambda/4$ microstrip antenna may be obtained with a square ring antenna [5, 6]. Removal of the central portion from the antenna creates a slot on the patch that lengthens the current flow path, which, in turn, lowers its resonance frequency. The resonant modes in a square ring antenna are TM_{mn0} and its lowest order mode is TM_{11} mode [7]. Its resonance frequency, due to the lowest order mode, can be made much lower by increasing the perforation, or in other words, by having narrow strip width. i.e. the narrower the width of the ring is, the more miniaturized the antenna is. However, when the width of the ring is narrow, a square ring microstrip antenna has a high input impedance, therefore, it is difficult to match to a $50\text{-}\Omega$ input circuit. Now, the performance of any antenna is evaluated based on its impedance bandwidth, radiation resistance, gain and efficiency, etc., and miniaturized antennas inherently are associated with several problems, such as narrow impedance bandwidth, poor radiation resistance, low gain and efficiency, and high cross-polarization. However, unlike other miniaturized antennas, square ring antennas, as long as their width is within certain limit, do not have significant loss in gain. Nevertheless, they suffer from narrow impedance bandwidth similar to other miniaturized antennas.

In order to overcome the problem of narrow impedance bandwidth of the square ring antenna, a stacked-resonator concept is used in [5] to generate double-tuned resonance configuration [8-13], and wideband performance is achieved successfully. First, a combination of square ring and square patch is considered, where the square ring is fed by a $50\text{ }\Omega$ probe, and the square patch is parasitically excited. In another attempt,

square rings are used as both parasitic and driven resonators, and again, good impedance matching and wide impedance bandwidth have been achieved. The polarization of the square ring antennas studied in [5] is linear.

Circular polarization (CP) using a stacked-ring configuration, with a single feed, has not been attempted yet, which motivates the author to conduct research on stacked square ring antennas for CP. It is necessary to mention here that circularly polarized antennas are more suitable in mobile and satellite communications because of their inherent capabilities of reduced multi-path fading, improved coverage and fixed polarization [14, 15]. Developing methods to obtain circular polarization (CP) from microstrip antennas became very popular in the last few decades. Axial ratio (AR) is the measure of the purity of CP, and the frequency band where the axial ratio is below 3-dB is normally accepted as the axial ratio bandwidth. It is always desired that the impedance bandwidth is significantly greater than the axial ratio bandwidth to ensure the uninterrupted CP radiation. For a singly-fed microstrip antenna, the axial ratio bandwidth is very narrow. When small antennas are used for the CP purpose, it has been observed that their 3-dB axial ratio bandwidth is even narrower. For example, CP from probe-fed single-layer microstrip square ring antennas has been obtained by truncating diagonal corners [16, 17], by feeding the ring diagonally [7] and using crossed strips [18], but the axial ratio bandwidths are even narrower in these miniaturized single-feed cases, compared to regular patch antennas.

Again, for some mobile and satellite communication applications, such as global positioning system (GPS), the required coverage zone is very broad and is about the

entire upper hemisphere. In such cases, the antenna must have a broad coverage for CP. This is difficult with microstrip antennas, as their axial ratio beamwidth is normally narrow, and is restricted around the antenna boresight. These issues of circular polarization are addressed in the study of stacked square ring antennas in this thesis.

Like a typical stacked microstrip antenna, stacked square ring antennas can also be operated as a dual-band antenna, by selecting the dimensions of the parasitic and driven ring such that each ring operates at two distinct frequencies. However, it has the advantage of accommodating more rings or patches inside driven and parasitic rings that regular stacked microstrip antennas do not have. In the case of annular ring antennas, two additional concentric rings are used in the same layer mainly to increase its bandwidth using the resulting new resonant bands [19]. A similar attempt has been made for a triangular ring antenna [20]. In both cases, rings are electromagnetically fed by a transmission line on a different layer. In this thesis, in addition to two rings in the stacked configuration, a third ring is placed concentrically with the parasitic ring to obtain tri-band operation. In general, challenges and problems to excite this additional ring, along with the original stacked square rings, are discussed.

Multi-frequency operation can be obtained from a single layer square ring antenna when it is loaded with a narrow gap or slit. This phenomenon is discussed in detail in this thesis. Originally ring resonators were loaded with stub, notch or slit to overcome its typical problems of high input impedance for narrow width [6], to increase its bandwidth [21], or to reduce the cross-polarization level at its dominant mode [22]. However, an asymmetric gap loading excites multiple resonances, which are analyzed rigorously in

this thesis. One of the resonances in this case is much lower than the lowest mode frequency of a typical square ring antenna, which indicates a dramatic size reduction of the antenna. In fact, an even further miniaturized antenna size can be found, when the remaining slot of the gap-loaded square ring antenna is modified [23, 24]. Apparently, one can have much smaller antenna, but the high price one has to pay is in gain and efficiency reduction. In these small microstrip antennas, due to a higher concentration of currents, the ohmic losses are too high, consequently the gain is very low.

In order to enhance the gain of the miniaturized antennas mentioned above, a novel technique is developed, where the conductor of the square ring antennas is formed by depositing multiple conductor layers separated by dielectric lamination, having thickness smaller or of the order of the skin depth of the conductor. The idea of using multiple laminated conductor layers for the center conductor of the coaxial cable was first presented in 1951 [25], and the same technique was discussed for the transmission line in [26], mainly to reduce the skin effect losses. In this thesis, it has been shown using analytical solutions that, for a stacked laminated conductor system, power lost in the conductor is less when the laminating dielectric layers are introduced with the metal conductor. The concept is used for enhancing the gain of several miniaturized antennas having poor gain.

1.3 Organization of the thesis

As mentioned earlier, the thesis deals with square ring antennas. Unfortunately, a probe-fed square ring antenna has no practical use, when its width is narrow. Therefore, applying innovative techniques to improve its characteristics is obvious. A brief discussion about microstrip square ring antennas is already presented in this chapter. More background review is provided in chapter two, especially on the feeding mechanism of high-impedance square ring antennas. In addition to that, antenna miniaturization, along with associated problems of miniaturization, will be discussed in brief. For the convenience of the reader, important terms related to antennas and used in this thesis are defined and discussed in Appendix A.

Chapter three provides a detailed study of the singly-fed microstrip square ring antenna, where broadband circular polarization radiation performance has been achieved using stacked square rings with positive or negative corner perturbations. Different perturbation schemes have been discussed, one of which is a novel approach using a combination of positive and negative perturbations [27, 28]. For this case, the capability of providing wide angular coverage is described [29].

Chapter four discusses multi-frequency operation using stacked square rings, where an additional ring is accommodated inside the parasitic ring [30]. Narrow width of the rings is used in order to fit the third ring, which leads to feeding problem. Capacitive feeding is proposed in this situation, allowing a narrow strip width.

Chapter five deals with loaded microstrip square ring antenna for its multi-band, polarization and antenna miniaturization performance. Further miniaturized antennas are presented, obtained by modifying the ring slot. Because of miniaturization, severe gain and efficiency losses are noticed and explained briefly.

In chapter six, more analysis is carried out to understand the reason for gain and efficiency drop for several miniaturized antennas. The concept of multi-layered laminated conductor is introduced to address the problem of reduced gain. To establish the concept, a multi-layered laminated planar conductor is analyzed. Experimental results are presented to prove the concept.

Finally, the research is summarized in chapter seven. This chapter also concludes the thesis with recommendations and directions for future work.

CHAPTER TWO

Background Study: Antenna Miniaturization and Microstrip Ring Antennas

2.1 Introduction

Since the size of electronic components has been reduced significantly in recent years, the need for miniaturized and low profile antennas has increased in communication systems and other wireless applications. Consequently, in the recent past, there has been extensive research on miniaturization of antennas, which is a challenging task, as it leads to reduced impedance bandwidth and gain, high reactance, and higher cross-polarization. In this chapter, first different miniaturization techniques are reviewed, and their effects on the antenna performance are briefly discussed. Then, microstrip ring antennas, which are a type of miniaturized antennas, are discussed in greater detail. The feeding mechanism and loading of ring resonators are also reviewed.

2.2 Antenna miniaturization techniques

For efficient radiation, the length of a linear antenna like dipole or patch should be half a wavelength or larger according to the physics of electromagnetic wave. For

certain applications, half-wavelength antennas are considered to be large. Therefore, in recent years, there has been increasing research to miniaturize antennas. Several techniques to miniaturize antennas are available in the literature. These can be generalized in the following:

2.2.1 Loading with lumped elements:

Miniaturized antennas have strong reactive input impedance, which can be compensated for by loading with resistive (R) or reactive (L or C) components, or by adding conductive parts as shown in Fig. 2.1. It is the simplest method to make antennas smaller than a resonant length, still keeping resonant behaviors. However, if the lumped element has losses, the efficiency of the antenna will decrease. On the other hand, if the loss is less, the quality factor will increase resulting in a reduction in the bandwidth [4].

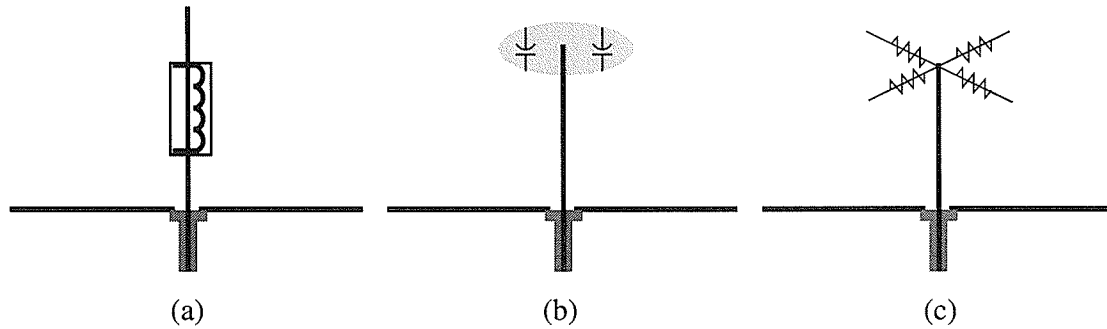


Fig. 2.1: Loading techniques: (a) inductive, (b) capacitive (c) conductive.

2.2.2 Loading with dielectric material

Loading with a dielectric material, to reduce the antenna size, is another simple method. Previously, its use was limited by the availability of appropriate substrates and their cost. With the advancement of substrate technology, very high permittivity ($\epsilon_r > 40$)

and low-loss substrates are available now. Since the wavelength is smaller in a high permittivity substrate, the antenna size reduces when loaded with such substrates, as indicated in Fig. 2.2 [4]. However, in high permittivity materials, the electric fields are trapped inside the substrate making radiation more difficult, which in turn enhances the quality factor because of increased stored energy. As a result, the bandwidth decreases. The gain is also affected due to the size reduction and high dielectric losses. ϵ_{eff} is defined in Appendix A.

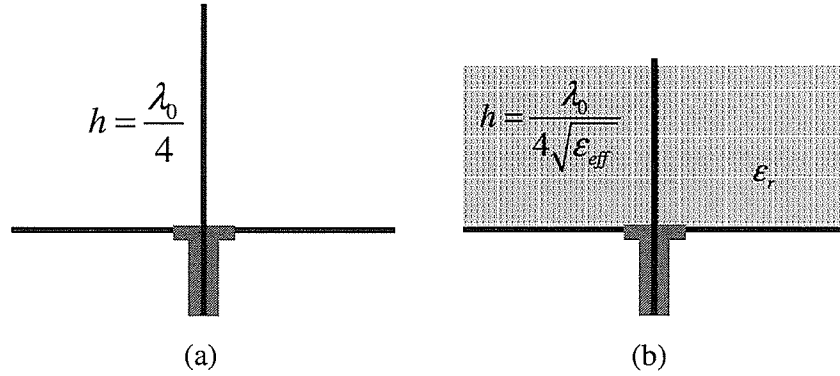


Fig. 2.2: (a) Monopole, and (b) dielectric loaded monopole. h is the height of the monopole, λ_o is the free space wavelength, ϵ_r and ϵ_{eff} are the relative and effective dielectric constant of the substrate material, respectively.

2.2.3 Using short circuits

For antenna miniaturization, this is the most popular technique. In the case of a half-wavelength dipole, its length can be halved by replacing one dipole arm by a ground plane, which acts like a mirror and creates an image of the existing half-dipole arm [4]. The antenna still remains resonant at the same frequency, but its size reduces by half. In the case of rectangular microstrip antennas, miniaturization can be obtained by placing a short circuit at the center where electric field is zero for the fundamental TM_{10} mode [2],

without affecting its resonant frequency, as shown Fig. 2.3. Thus, at a given operating frequency, the patch dimensions can be significantly reduced [3, 4]. The shorted quarter-wave patch has lower gain and efficiency, as the radiating element is smaller in size. It has a high input impedance at its radiating edge, and as such, is difficult to feed via a microstrip line. Also, it has a narrower impedance bandwidth. As the substrate is cut to place the short circuit plate, this antenna becomes mechanically weak. Instead of using a complete shorting wall, partial short is also used, which provides further miniaturization, because the effective current flow path becomes longer [1].

Shoring pins can also be used as an alternative to shorting walls, which is convenient from fabrication point of view. The important features of using shorting pins are well documented in references [31-33]. It has been found that the use of a very small number of shoring pins, instead of a complete short circuit, reduces the size of the quarter-wavelength antenna considerably, without affecting its performance. In fact, the maximum reduction in physical size can be achieved with only a single shoring post. This is due to the fact that the current tends to move diagonally, increasing the path length. However, the cross-polarization increases significantly because of the shoring pin.

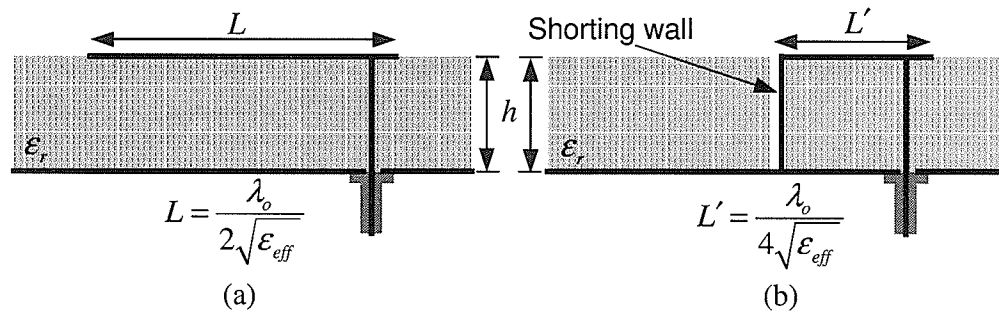


Fig. 2.3: (a) A half-wavelength microstrip antenna, and (b) a shorted microstrip antenna: λ_o is the free space wavelength, and ϵ_r and ϵ_{eff} are the relative and effective dielectric constant of the substrate material, respectively.

2.2.4 Modifying antenna geometry

The most widely used technique, by means of which many designs have been proposed, is based on modifying the antenna geometry and shape. The idea here is to meander the surface current, so that the current flow path becomes longer, resulting in a reduction in the resonant frequency, which represents a reduction in the antenna size. A good example of the antenna geometry modification is the inverted-L antenna, which was derived from the monopole by bending its wire. When a short circuit is added to the inverted-L antenna, the inverted-F antenna is found [4]. These modifications are shown in Fig. 2.4(a-c).

The above idea is extended to the microstrip antenna to reduce its size, where slots are inserted into the microstrip patch to force the surface currents (J_s) to meander, thus the effective current flow path length gets longer, and the antenna size is reduced. One example is given in Fig. 2.5.

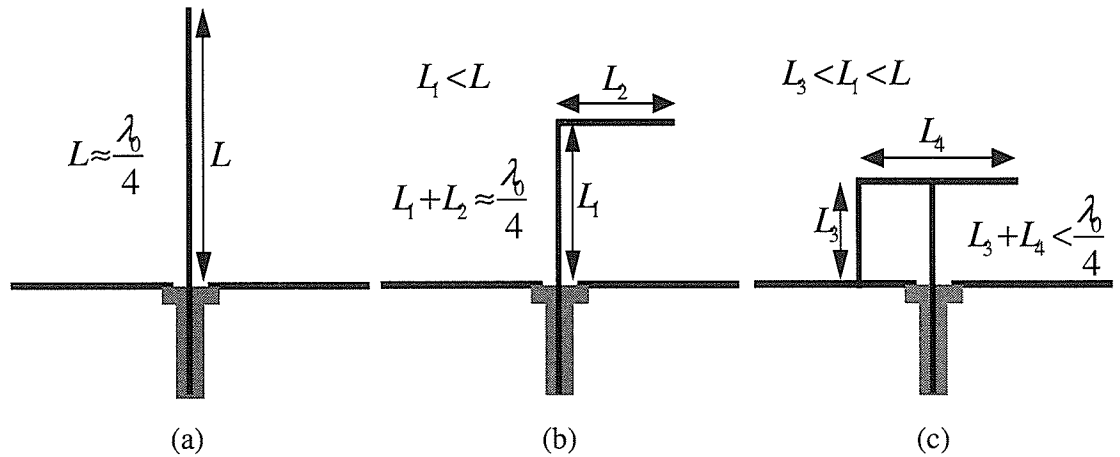


Fig. 2.4: (a) The monopole antenna, length: $L \approx \lambda_o/4$, (b) the inverted-L antenna, length: $L_1 + L_2 \approx \lambda_o/4$, and (c) the inverted-F antenna, length $L_3 + L_4 < \lambda_o/4$. λ_o is the free space wavelength.

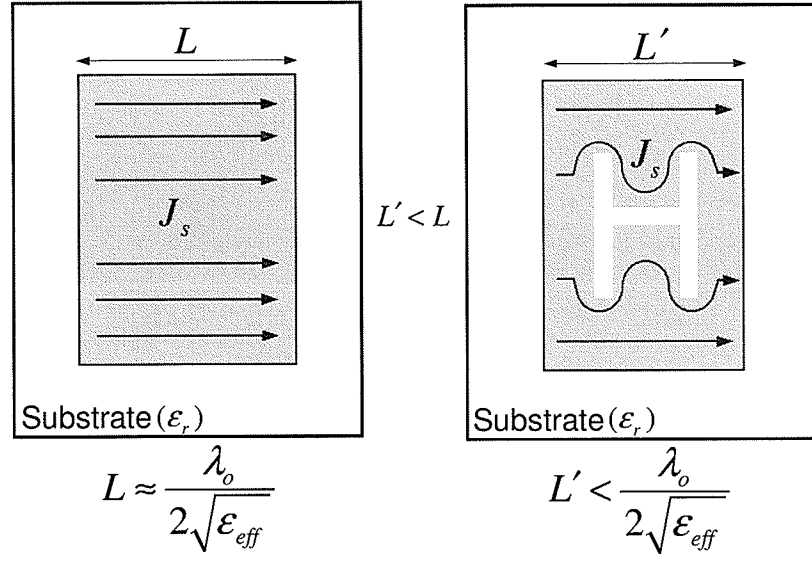


Fig. 2.5: Current flow path on (a) a microstrip patch antenna, and (b) a patch antenna with H-shaped slot. ϵ_r and ϵ_{eff} are the relative and effective dielectric constant of the substrate material, respectively.

In the case of microstrip antennas, for a fixed ground plane size, the antenna metalization area can be reduced by modifying antenna geometry. This will provide more space for electronic circuitry to be needed for practical applications. Later in this thesis, miniaturized microstrip antennas are to be considered as small metalization area of the patch conductors.

2.3 Major disadvantages of miniaturized antennas

The problems associated with miniaturized antennas, as discussed earlier, can be explained by referring to the fundamental limits of small antennas. These limits are

completely related to the minimum quality factor (Q) of the small antennas. Therefore, we first look at the generally accepted definition of the antenna quality factor, Q [34]:

$$Q = \text{Max} \left\{ \frac{2\omega\tilde{W}_e}{P_{\text{rad}} + P_{\text{loss}}}, \frac{2\omega\tilde{W}_m}{P_{\text{rad}} + P_{\text{loss}}} \right\} \quad (2.1)$$

where $\omega = 2\pi f$ is the frequency, \tilde{W}_e and \tilde{W}_m are the time-averaged stored electric and magnetic energy respectively, P_{rad} is the total radiated power of the antenna, and P_{loss} is the power loss due to resistive and dielectric losses.

Wheeler was the first to draw the attention to the fundamental limits of ‘small antennas’ in 1947 [35, 36]. He introduced the term ‘radiansphere’, which is a spherical volume of radius $\lambda/2\pi$ enclosing the antenna, and defined the small antenna as one occupying a small fraction of a radiansphere in space. He also used the term ‘radiation power factor’, which expresses the radiation from a small antenna taking a much larger volume of the reactive power, and related this to the bandwidth and efficiency of the small antenna [37]. Chu then generalized the concept of small antennas in [38] where he considered a spherical volume enclosing the antenna, as shown in Fig. 2.6, and gave an approximate expression for the Q of a linearly polarized lossless omni-directional antenna:

$$Q = \frac{1 + 2(ka)^2}{(ka)^3 + [1 + (ka)^3]} \quad (2.2)$$

where k is the wave number and a is the radius of the smallest sphere enclosing the antenna. All other researchers later considered a spherical boundary to enclose antennas to determine their fundamental limits [39].

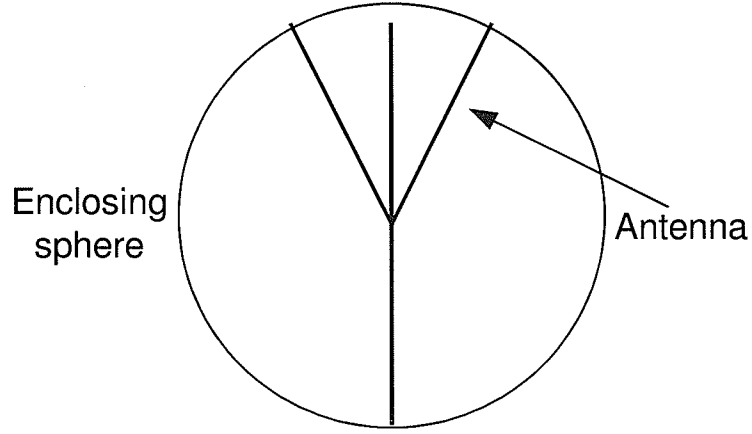


Fig. 2.6: Imaginary spherical boundary fully enclosing the antenna.

Harrington extended the idea to include the losses of the antenna, and related the gain of the antenna with the smallest possible volume enclosing the antenna, as given by the following equation [40]:

$$G = (ka)^2 + 2ka \quad (2.3)$$

McLean re-examined the expression for Q introduced by Chu-Harrington, and derived the exact expression for a linearly polarized antenna with a lowest order single mode (TE or TM) [34]:

$$Q = \frac{1}{(ka)^3} + \frac{1}{ka} \quad (2.4)$$

For a circularly polarized small antenna, the Q has the form [34]:

$$Q = \frac{1}{2} \left[\frac{1}{(ka)^3} + \frac{2}{ka} \right] \quad (2.5)$$

It is well known that the fractional bandwidth of an antenna is:

$$BW = \frac{f_u - f_L}{f_0} = \frac{\Delta f}{f_0} = \frac{1}{Q} \quad (2.6)$$

where f_L and f_u are the lower and upper frequencies of the frequency band of the antenna. The relationship of bandwidth and Q is based on the half-power bandwidth. The bandwidth based on voltage standing wave ratio ($VSWR$) ≤ 2 is given by

$$BW = \frac{f_u - f_L}{f_0} = \frac{\Delta f}{f_0} = \frac{VSWR - 1}{Q\sqrt{VSWR}} \quad (2.7)$$

Note that the bandwidth based on $VSWR \leq 2$ is about 78% of the half-power bandwidth [10]. Moreover, $VSWR = 2$ refers to a return loss (RL) of about 9.54 dB, and thus, sometimes impedance bandwidth is defined in terms of 10-dB return loss value. The relationship between $VSWR$ and return loss is given by [41]:

$$VSWR = \frac{\sqrt{RL} + 1}{\sqrt{RL} - 1} \quad (2.8)$$

Interested readers can find different methods for evaluating antenna Q in [42-47].

Based on the above discussion, we can easily notice the practical limits of the performance properties of miniaturized antennas and the reasons behind the major disadvantages associated with them as explained below.

Effect on gain: Equation (2.3) gives a practical upper limit for the gain of a small antenna, while still having a reasonable bandwidth. So, a very small antenna is not practical if an appreciable gain is needed.

Effect on efficiency: A miniaturized antenna will show a higher concentration of surface currents toward one point. Thus, ohmic losses will be enhanced, and consequently the efficiency of the antenna will decrease.

Effect on bandwidth: The quality factor, Q , of a small antenna can be determined from the size of the antenna, using equations (2.4) and (2.5). On the other hand, equation (2.6) shows the inverse relationship between frequency bandwidth and Q . Thus, the more miniaturized the antenna is, the less the impedance bandwidth will be.

Effect on polarization purity: In many cases, miniaturization of an antenna affects the polarization purity. As mentioned earlier, in small antennas the concentration of the surface current is higher toward one point, which leads to cross-polarization radiation.

Feed problem: In the case of small antennas, sometimes it is difficult to correctly feed them. From manufacturing point of view, small antennas are complicated to feed properly.

2.4 Microstrip ring antennas

Ring antennas are derived from regular patch antennas, using the miniaturization technique of modifying antenna geometry, discussed in Section 2.2.4. In ring resonators, the current flow path is longer because of the removal of the central metal portion, which indicates miniaturization of antennas. Microstrip ring antennas can be of many shapes, e.g. square, circular, triangular etc., as shown in Fig. 2.7. They are, in fact, electrically and geometrically intermediate configurations between printed patches and printed loops, as indicated in Fig. 2.8. A microstrip ring antenna is significantly smaller than a regular

patch antenna. Its smallness is dependent on the width of the ring. On the other hand, its input impedance is also dependent on the width too. Since it is a miniaturized antenna, its bandwidth is narrower compared to a regular patch antenna.

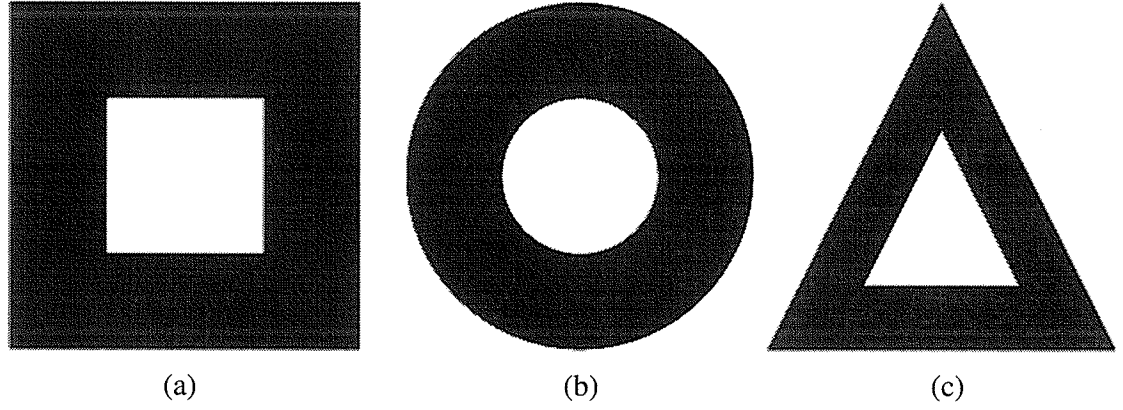


Fig. 2.7: (a) Square, (b) annular, and (c) triangular ring antennas derived from regular-shaped patch antennas.

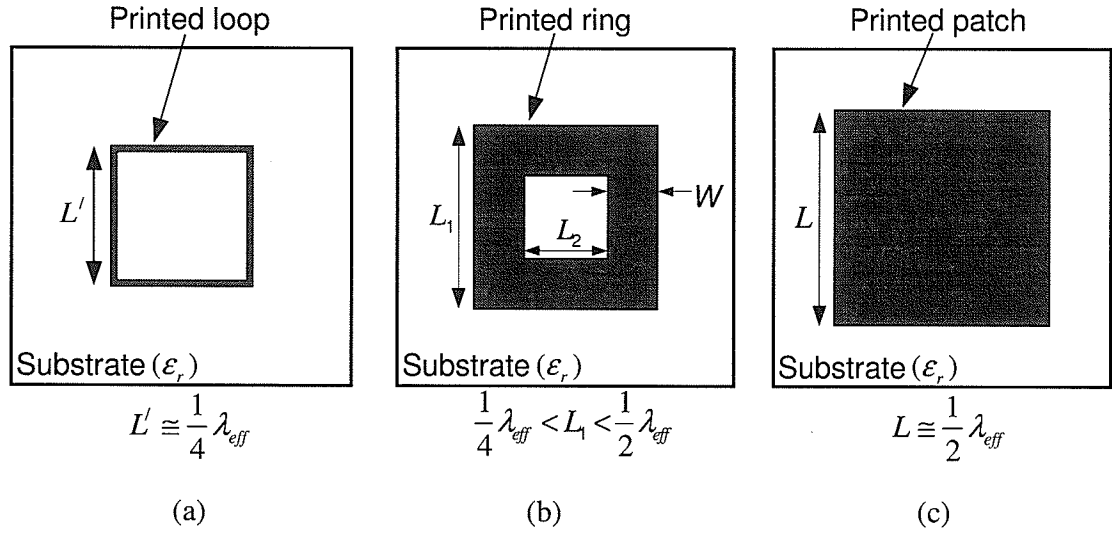


Fig. 2.8: Geometry of a (a) square loop, (b) square ring and (c) regular square patch.

$\lambda_{eff} = \frac{\lambda_0}{\sqrt{\epsilon_{eff}}}$ is the wavelength in the dielectric, and ϵ_r and ϵ_{eff} are the relative and effective dielectric constant of the substrate material, respectively.

As a first ring resonator, the microstrip annular ring was proposed. Analysis of annular ring resonators is an old research topic, and several analysis methods are available in the literature [48-50]. The triangular ring antenna is not very popular and discussed in [20]. A rectangular ring antenna is analyzed using segmentation technique and cavity model in [51]. Characteristics of microstrip square ring antennas are extensively studied in [5]. Since, this thesis deals with the square ring antenna, more discussion is provided on it, rather than circular and triangular rings.

The width of the ring can be found from the geometry of the square ring antenna shown in Fig. 2.8(b):

$$W = (L_1 - L_2) / 2 \quad (2.9)$$

where L_1 and L_2 are the outer and inner lengths of the square ring antenna, respectively. Then, the average circumferential length of the square ring antenna, denoted by L_{avg} , can be expressed as:

$$L_{avg} = (L_2 + W) \times 4 \quad (2.10)$$

In general, L_{avg} of the ring is equal to the wavelength in the dielectric used for the antenna. Thus, the resonance frequency for the dominant mode of the square ring antenna can be found from the following equation:

$$f_r = \frac{c}{L_{avg} \sqrt{\epsilon_{eff}}} \quad (2.11)$$

where ϵ_{eff} is the effective permittivity of the microstrip structure.

Narrow strip width of the square ring antenna is desired in order to have compactness. However, when the width is narrow, its input impedance becomes few

thousands ohms. It has been found in [5] that the ratio L_2/L_1 has to be less than 0.4 in order to be able to use 50-Ω SMA probe to excite the square ring. This miniaturized antenna has narrow impedance bandwidth as well. A straightforward approach to use probe-feed and obtain wider impedance bandwidth is to use stacked ring resonators [5].

If $L_2/L_1 > 0.4$, i.e. the width of the strip is narrow, probe-feed becomes impractical because of high input impedance of the ring antenna. In this case, capacitive feeding [22, 52, 53] can be used, or the ring can be loaded with stub or gap [6, 21]. In the case of capacitive feeding, a metal strip is placed in close proximity of the ring, which is excited. Energy is coupled to the ring from the strip and excites the ring. The width of the feeding strip is not that important for impedance matching, rather its length and separation are responsible for the input reactance at the feed. Stub loading also improves the impedance matching, and increases the bandwidth. However, both these techniques contribute to higher cross-polarization because several other modes are excited. Interestingly, for regular square ring antennas, the gain loss is not that significant, even though it's a miniaturized antenna. However, when smaller antennas are attempted by modifying square ring antennas, significant drop in the gain is noticed [23].

2.5 Conclusion

In this chapter, the main disadvantages of miniaturized antennas were discussed which were governed by the fundamental limits of small antennas. The quality factor, Q , of the antenna was affected when different miniaturization techniques were applied, and

consequently the electrical performance of the antenna deteriorated. It is of utmost importance to obtain small antennas alleviating these disadvantages. Microstrip ring antennas are miniaturized antennas, obtained by modifying the geometry of regular patch antennas. Single-feed single-layer square ring antennas cannot be used efficiently when the strip width of the ring is narrow, because they come with typical problems of miniaturized antennas, such as, narrow impedance bandwidth, and high cross-polarization. To achieve wider bandwidths, stacked rings are used. Since, the stacked ring configuration with a single feed has not been studied yet for circular polarization, it will be discussed in the next chapter. Later in the thesis, other variations of square ring antennas on single and dual layers are discussed with a view to overcome the typical problems of such miniaturized antennas.

CHAPTER THREE

Stacked Square Ring Antennas for Wideband Circular Polarization

3.1 Introduction

In this chapter, we present a broadband single probe-fed square ring antenna for circular polarization (CP) using stacked rings, where CP is obtained with corner perturbation. The perturbation can be of the form of cutting diagonal corners, called negative perturbation, or adding metal stubs to the diagonal corners, known as positive perturbation [3]. Several perturbation schemes, namely positive perturbation, negative perturbation or hybrid perturbation (a combination of positive and negative perturbations), are presented for this dual-layer square ring antenna (DLSRA). In order to achieve wider axial ratio (AR) bandwidth compared to a singly-fed single-layer square ring antenna, a systematic design approach is followed as presented in [54]. The problem of narrow axial ratio beamwidth is addressed with hybrid perturbation scheme. The effects of finite ground plane on the CP performance of this small antenna are also discussed.

3.2 Circular polarization from DLSRA with corner perturbation

If only one probe-feed is to be used for the square ring antenna, then to generate CP, either nearly square rings can be used, or the geometry of the ring has to be perturbed, or the ring has to be fed diagonally [2, 3]. We chose the perturbation technique to obtain CP from stacked square ring antennas. First, we will discuss the wideband performance of stacked square rings.

3.2.1 Microstrip dual layer square-ring antenna (DLSRA)

The stacked square ring antenna is shown in Fig. 3.1. The substrate for the driven ring has a dielectric constant (ϵ_r) of 3.2 and thickness (h_1) of 1.6 mm. A dual-layer square ring antenna on this substrate has an impedance bandwidth of 88 MHz (1532 to 1620 MHz), or 5.6%, for the design frequency of 1.575 GHz, with $L_1 = 59$ mm, $L_2/L_1 = 0.67$, $L_3 = 47$ mm, $L_4/L_3 = 0.32$, probe-position: $(X_F, Y_F) = (21 \text{ mm}, 0 \text{ mm})$. These parameters are defined in Fig. 3.2. Since the width of the parasitic ring is narrow, the separation between the driven and parasitic ring is selected judiciously ($h_2 = 8$ mm) to achieve good impedance match. The foam, which has relative permittivity approximately equal to air, is used between the two rings. It can be shown from the dimensions of the antenna that the average circumferential length of each ring is about one-wavelength on the respective substrate.

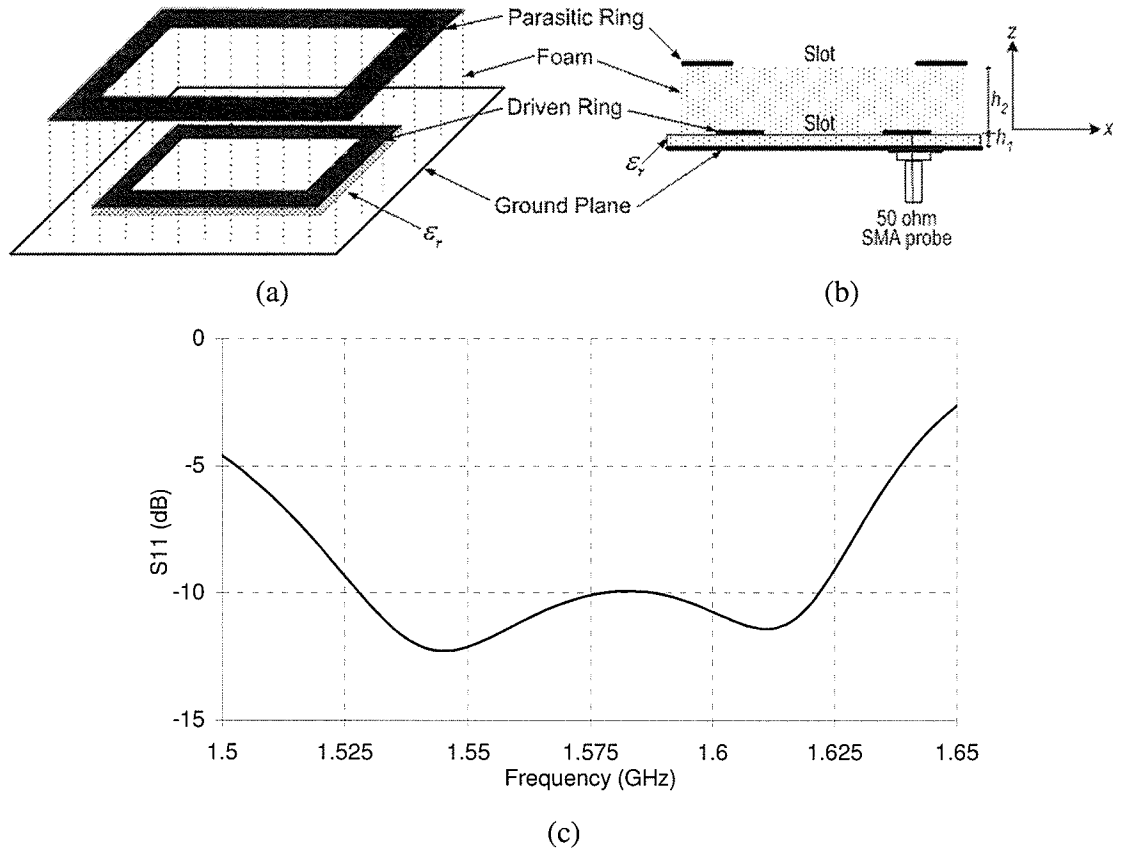


Fig. 3.1: (a) 3-D view and (b) side view of the dual-layer square-ring antenna (DLSRA), and (c) its return loss.

3.2.2 Effect of perturbing either parasitic or driven ring

The above-mentioned antenna will transmit or receive linearly polarized signals. Owing to two resonators, two resonances are observed for the DLSRA antenna based on minimum S_{11} value: the first resonance at 1.545 GHz due to the parasitic ring, and the second resonance at 1.6125 GHz for the driven ring. As mentioned in [7], the resonant modes in square ring antenna are TM_{mn0} , and to generate CP in DLSRA, two degenerate

modes with orthogonal polarization, TM_{10} and TM_{01} , are to be excited. This can be done by perturbing diagonal corners of the square ring. In this case, perturbation is applied by cutting equal parts from the diagonal corners of the parasitic or driven ring, as shown in Fig. 3.2. As the parasitic ring is responsible for the first resonance, when corner truncation is applied to that ring, good CP can be obtained around this frequency, as can be seen in the axial ratio plot in Fig. 3.3. With corner truncation, $p_c = 11.5$ mm, the axial ratio at 1.524 GHz is 0.25 dB with 3-dB axial ratio bandwidth (BW) of 11.5 MHz (1517.5 to 1529 MHz). However, the second resonance suffers from bad axial ratio. The perturbation on the parasitic ring also disturbs the return loss of the antenna, and as such impedance bandwidth goes down, as mentioned in Table 3.1.

Typically, a single square patch antenna with corner truncation, on the same substrate, operating at 1.575 GHz, has a 3-dB axial ratio bandwidth (AR BW) of approximately 6 MHz (0.4%), with right-hand circular polarization (RHCP) gain at 1.575 GHz of 6.19 dBic, which can be easily demonstrated by simulation. Apparently, the DLSRA antenna shows wider axial ratio bandwidth, however, not around 1.575 GHz, which is the desired operating frequency. Again, if only two diagonal corners of the driven ring are cut, good CP can be achieved near the second resonance, as can be seen in Fig. 3.3. In this case, the first resonance has high axial ratio value. In both cases, the axial ratio at 1.575 GHz is much higher.

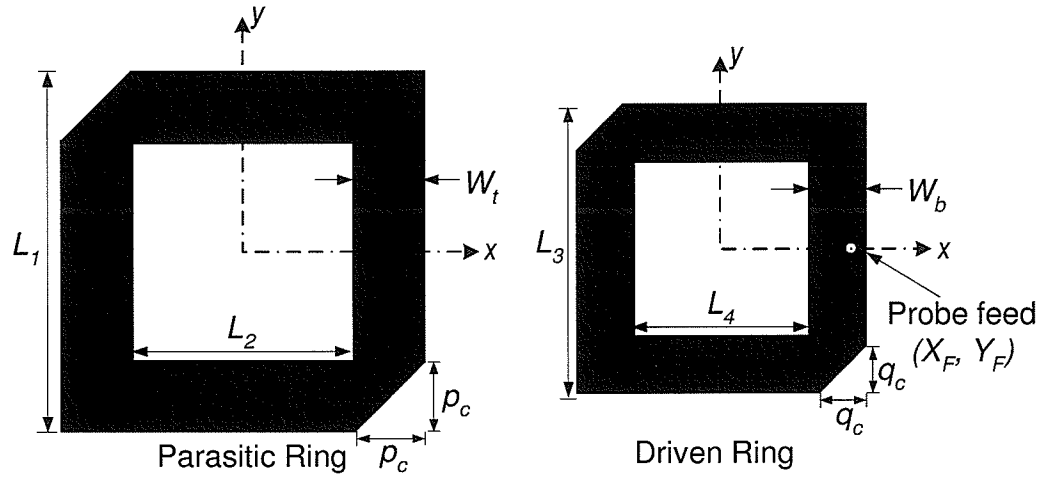


Fig. 3.2: Geometry of the driven and parasitic rings of the DLSRA with negative perturbation.

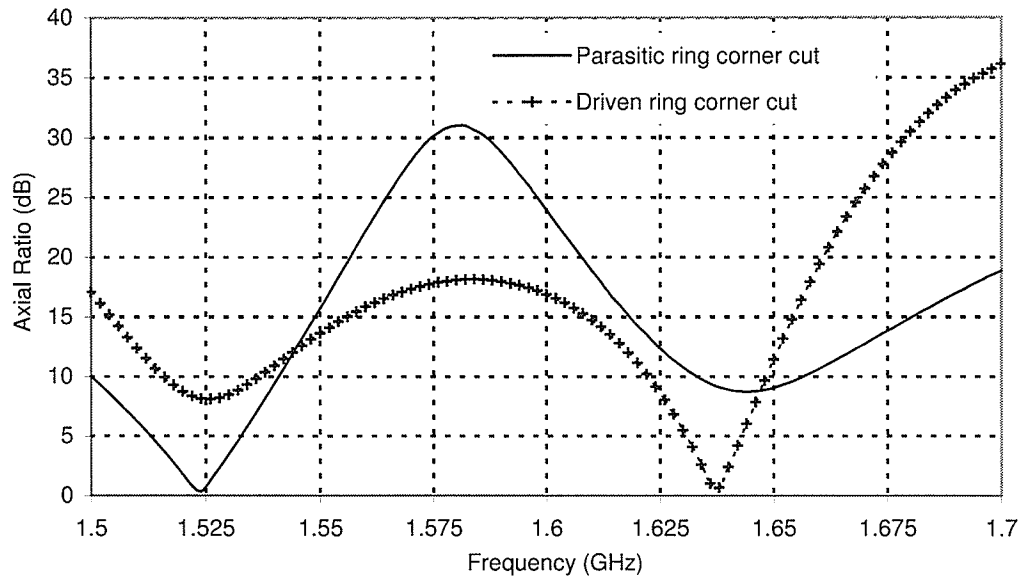


Fig. 3.3: Simulated axial ratio of the DLSRA with perturbing either parasitic ring or driven ring.

Table 3.1: DLSRA CP performance, obtained using corner perturbation in either driven or parasitic ring

Parasitic ring cut (mm)	Driven ring cut (mm)	10-dB return loss BW (MHz)	Axial ratio (AR) at $\theta = 0^\circ$		3-dB axial ratio BW (MHz)	Right hand CP Gain at f_{AR} (dBic)
			f_{AR} (MHz)	AR (dB)		
$p_c = 0$	$q_c = 0$	1532-1620 = 88	-	-	-	-
$p_c = 11.5$	$q_c = 0$	1493-1555 = 62	1524	0.25	1517.5-1529.2 (= 11.7)	7.85
$p_c = 0$	$q_c = 5.5$	1623.5-1650.5 = 27	1637	0.28	1633.5-1640 (= 6.5)	9.45

3.2.3 Broadband CP performance from the DLSRA by negative perturbation

In [54], a systematic design procedure is demonstrated to obtain broadband CP performance from stacked patch antennas, where perturbation is introduced in both parasitic and driven patches. A similar approach is adopted for the DLSRA, with an aim to achieve wide axial ratio bandwidth. The ring sizes, the separation between parasitic and driven rings, and the perturbation amount are the influencing parameters, the judicial selection of which gives wide axial ratio and impedance bandwidths.

At first, the very common technique, negative perturbation, in the form of cutting corners, is applied to the diagonal corners of both rings, in order to achieve good axial

ratio bandwidth around the design frequency of 1.575 GHz. The separation between the two rings, or the foam thickness (h_2), has to be selected in such a way as to ensure effective coupling between the two square-rings, which is also an important parameter for circularly polarized stacked patch antennas [55]. Again, this separation, as well as the perturbation, has effect on the quality factor (Q) of the antenna, which determines the axial ratio bandwidth, according to the following relationship [56]:

$$BW_{AR} = \frac{AR_{max} - 1}{\sqrt{AR_{max}} Q} \quad (3.1)$$

where AR_{max} is the maximum allowable axial ratio that defines the bandwidth. Typically, AR_{max} is $\sqrt{2}$ (3-dB). Therefore, the foam thickness (h_2) is optimized to obtain wide impedance and axial ratio bandwidths, which is found to be 11 mm. The perturbation amount is also optimized, in both parasitic and driven rings, for low axial ratio value. In this case, corners are cut with respect to the probe position such that right-hand circular polarization (RHCP) is achieved, as shown in Fig. 3.2. It is evident at this point that, in order to get left-hand circular polarization (LHCP), the location of the cuts has to be changed to the other diagonal corners. The optimized antenna parameters are tabulated in detail in Table 3.2.

Because of the perturbation, two orthogonal modes are excited on each ring, and the two central adjacent modes are merged together due to the optimized parameters. Thus, we can see only three resonances on the return loss plot of Fig. 3.4(a). Consequently, the impedance bandwidth has increased, which is 160 MHz (1510 to 1670 MHz). Due to the perturbation in both rings, it can be seen from Fig. 3.4(b) that, the axial ratio plot has two dips close to each other, thus, significantly increasing 3-dB axial ratio

bandwidth to 72 MHz (1541 to 1613 MHz), which is much larger than that of the single-layer square ring antenna. RHCP gain is above 7 dBic in the frequency range of 1505 to 1677 MHz, as can be seen in the same figure. The simulated CP gain patterns of this antenna, in the two principal planes, are shown in Fig. 3.5 at the design frequency. The antenna shows a peak RHCP gain of about 8.74 dBic along the boresight. However, gain is below 0 dBic after $\pm 60^\circ$ of the boresight.

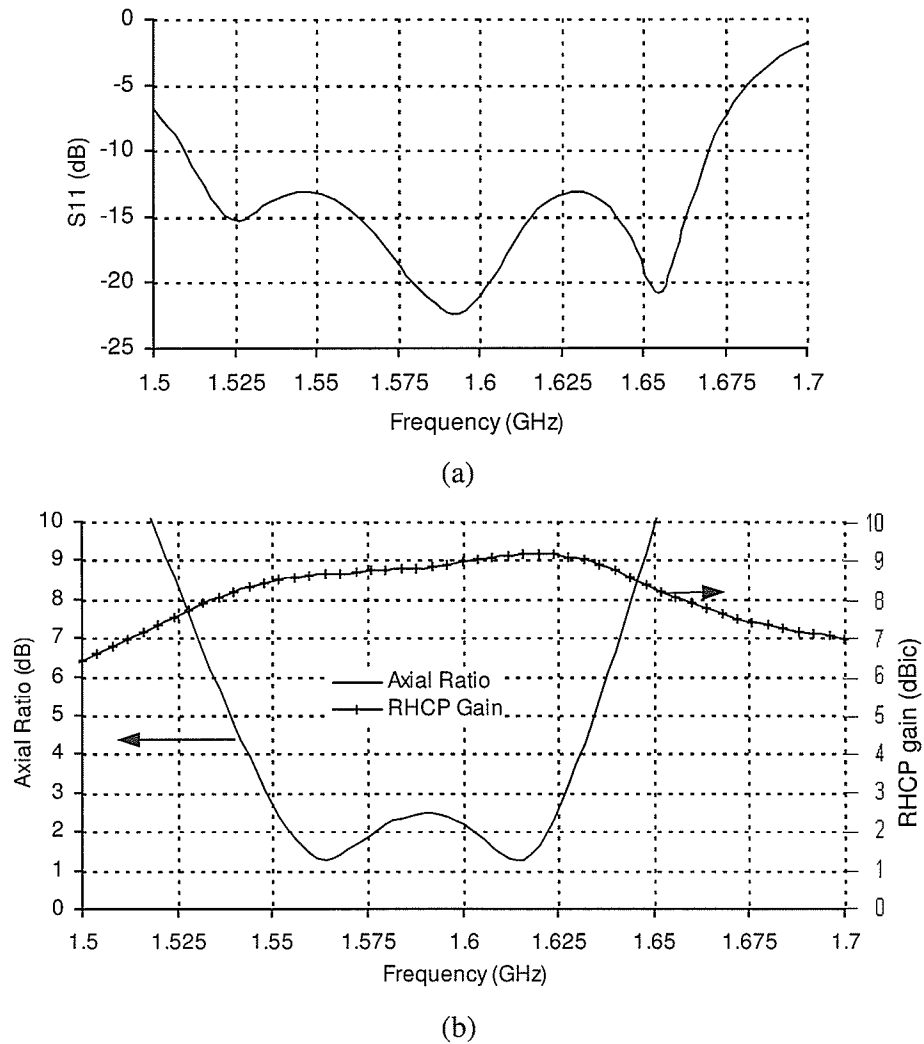


Fig. 3.4: (a) Return loss plot and (b) axial ratio and RHCP gain vs. frequency plot of the DLSRA with negative perturbation [Fig. 3.2]. The antenna parameters are tabulated in Table 3.2.

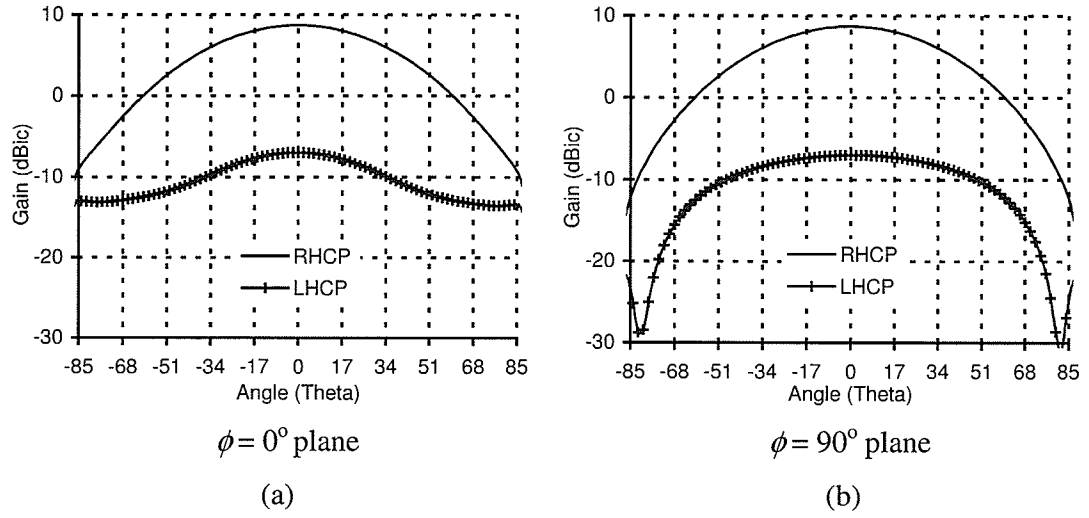


Fig. 3.5: Simulated CP gain patterns in the (a) $\phi = 0^\circ$ and (b) $\phi = 90^\circ$ planes, at 1.575 GHz, of the DLSRA antenna with negative perturbation [Fig. 3.2]. The antenna parameters are tabulated in Table 3.2.

3.2.4 CP from DLSRA by outward positive perturbation

Another popular technique, to achieve CP from microstrip antennas, is protruding metal stubs to the diagonal corners, which can be called positive perturbation. In the case of DLSRA, metal strips are protruded to the outward direction of the diagonal corners of both rings, as shown in Fig. 3.6(a). Keeping the parasitic ring size and the foam thickness fixed at what was in the previous case ($L_1 = 59$ mm, $h_2 = 11$ mm), the perturbation area, ring widths and the driven ring size are optimized, to achieve wider impedance and axial ratio bandwidths around the design frequency. Adding metal stubs to the diagonal corners increases the overall antenna size.

The antenna parameters, optimized for wide axial ratio bandwidth, are indicated in Table 3.2, and the simulated return loss, for this case, is shown in Fig. 3.6(b). 10-dB return loss bandwidth of 173 MHz (1510 to 1683 MHz) is obtained, which is slightly larger than the previous case, and 3-dB AR bandwidth is also slightly higher, 79 MHz (1545 to 1624 MHz), compared to the previous case. 7-dBic RHCP gain bandwidth is 187 MHz (1505 to 1692 MHz), as shown in Fig. 3.6(c). The slight improvement in the bandwidths is due to the increase in the overall antenna size. Because of the added stub to the parasitic ring, the overall size of the antenna increases from $L_I = 59$ mm to $L_5 = 66$ mm, which indicates an increase in the overall area of about 25.4%, with reference to the negatively perturbed case.

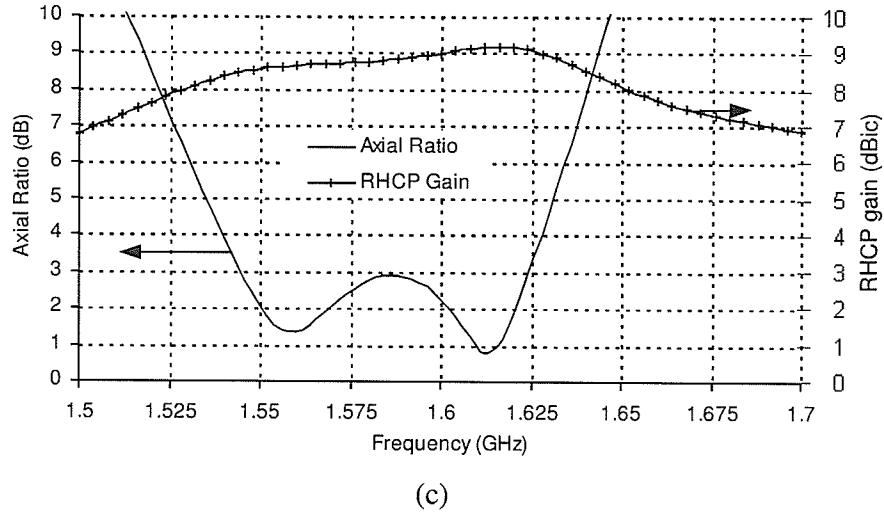
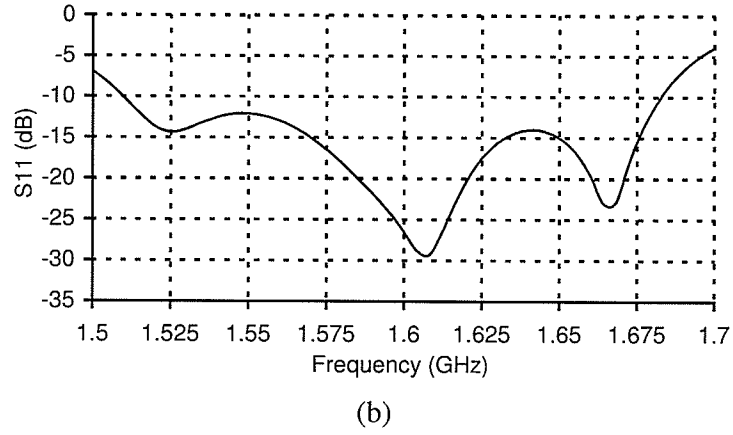
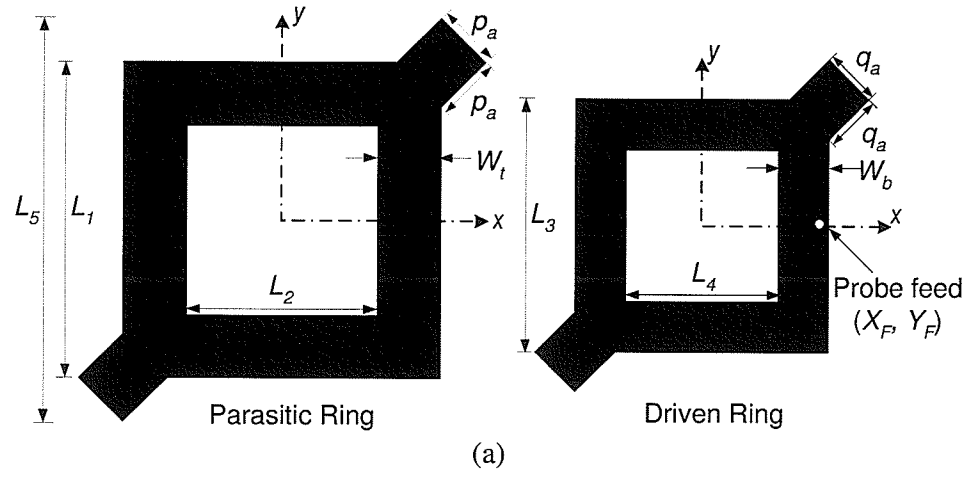
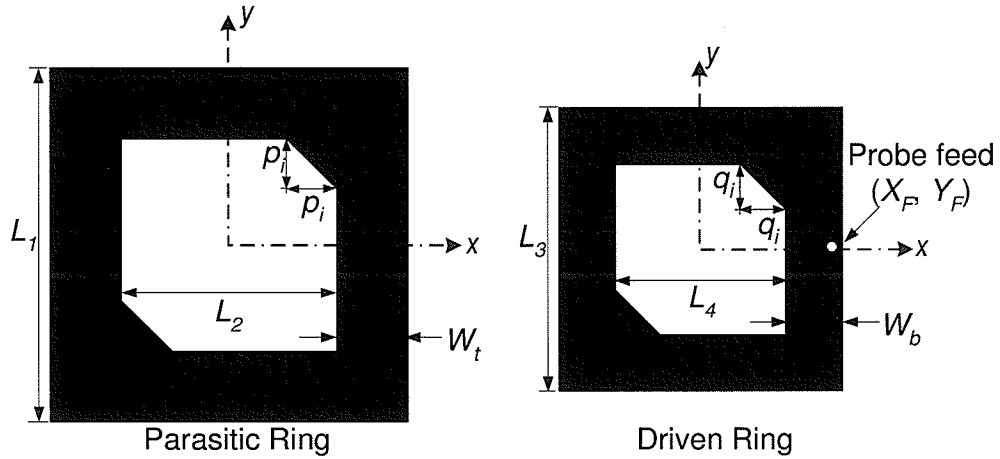


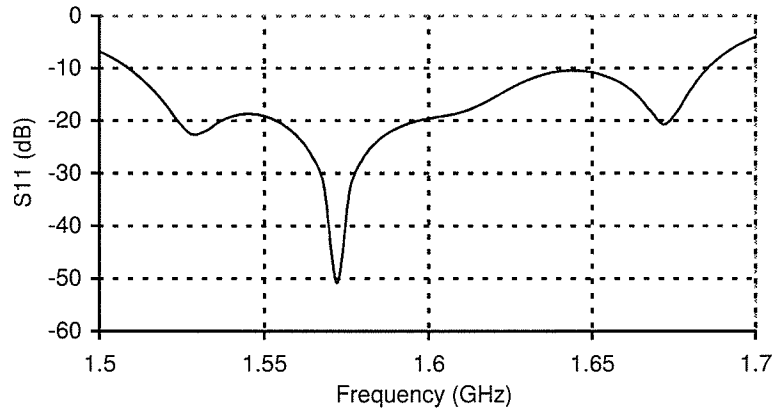
Fig. 3.6: (a) Geometry of the driven and parasitic rings of the DLSRA with outward positive perturbation, and its simulated (b) return loss plot, and (c) axial ratio and RHCP gain vs. frequency plot. The antenna parameters are tabulated in Table 3.2.

3.2.5 CP from DLSRA by inward positive perturbation

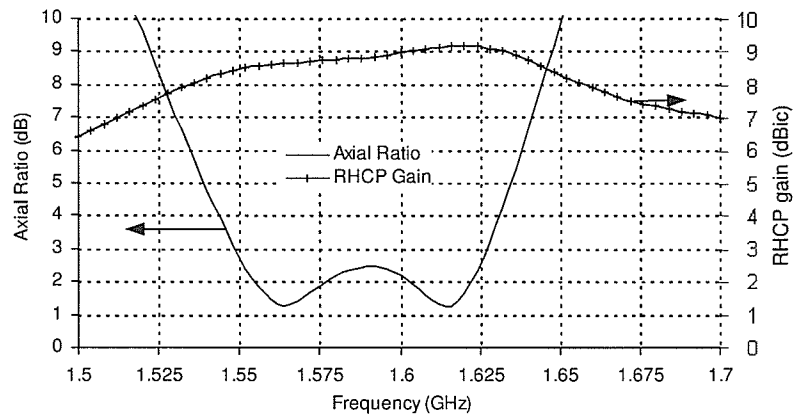
Positive perturbation can also be realized by adding metal stubs to the inward direction of the diagonal corners of the square rings, as shown in Fig. 3.7(a). Again, Table 3.2 summarizes the optimized antenna parameters, and obtained impedance, axial ratio and RHCP gain bandwidths. The simulated return loss plot is shown in Fig. 3.7(b), and 10-dB return loss bandwidth is 177 MHz (1509 to 1686 MHz). 3-dB axial ratio bandwidth of 78 MHz (1549 to 1627 MHz) and 7-dBic RHCP gain bandwidth of 186 MHz (1513 to 1699 MHz) are obtained, as shown in Fig. 3.7(c). It is evident that both types of positive perturbation give similar results, however, the inward positive perturbation case has the advantage of not increasing the overall size of the antenna, as the metal strips are added in the slot portion inside the square rings.



(a)



(b)



(c)

Fig. 3.7: (a) Geometry of the driven and parasitic rings of the DLSRA with inward positive perturbation, and its simulated (b) return loss plot, and (c) axial ratio and RHCP gain vs. frequency plot. The antenna parameters are tabulated in Table 3.2.

3.2.6 A novel approach: CP from DLSRA by hybrid perturbation

Typically, a similar perturbation type (either positive or negative) is used to achieve CP from microstrip antennas, as used in the previous sections in the case of square ring antennas. In this section, a novel technique is presented for stacked square ring, where a combination of positive and negative perturbations, which can be called hybrid perturbation, is introduced to the diagonal corners of the driven and parasitic rings respectively, for several advantages.

It has been mentioned earlier that circularly polarized microstrip antennas suffer from narrow axial ratio beamwidth. This is also common for the DLSRA CP antennas with corner perturbation, as shown in Table 3.2. Specially, the antenna with negative perturbation has only 118° (off the boresight) of angular coverage. In the case of microstrip arrays, this problem has been overcome by using a sequential rotation of the array elements [58]. In this configuration, each subsequent element of an N -element array is rotated physically by an angle of $p(n-1)\pi/N$, and its excitation phase is corrected by the same angle, where p is an integer between 1 and $(N-1)$. Here, the idea of sequential rotation is applied to perturbed stacked square ring microstrip antennas for CP, which essentially widens the angular coverage of the antenna. If we assume the stacked microstrip square ring antenna as a 2-element array, the rotation angle will be $\pi/2$. However, in stacked rings only the lower element is fed. The upper element is parasitically coupled to the lower one. Since only one of the rings is fed, the phase correction to compensate for the rotation must be done geometrically.

To achieve a right hand circular polarization (RHCP) using negative perturbation from stacked square rings, the diagonal corners of both patches, to the left of the feed point, were cut at 45° . To implement the sequential rotation, one of the rings must be rotated by 90° , meaning that the corner perturbation will now be on the right side of the feed point. Since this form of corner perturbation generates a left hand circular polarization, the combined antenna of two stacked ring patches will become linearly polarized. Thus, for maintaining the circular polarization, one now must use a corner stub (a positive perturbation). The resulting stacked antenna geometry is shown in Fig. 3.8(a).

The principle of operation is as follows. The corner perturbations of the parasitic and driven rings will excite two degenerate orthogonally polarized TM_{10} and TM_{01} modes. With similar perturbations on both ring patches (either positive or negative), the correct phase relationship between the two modes is maintained for both rings. However, in the proposed design, rotating one of the ring patches alters the phase relationship of the modes. Thus, a positive perturbation of the other ring patch, as shown in Fig. 3.8(a), is needed to re-establish the correct phase relationship of the orthogonal modes.

The optimized antenna shows wide impedance bandwidth of 152 MHz (1517 to 1669 MHz), as well as, broad 3-dB AR bandwidth of 77 MHz (1547 to 1624 MHz), as can be found from Figs. 3.8(b) and 3.8(c). Compared to the outward positive perturbation case (Section 3.2.4), this design has the advantage of smaller antenna area due to the fact that, the driven ring is smaller in size than the parasitic ring due to the higher ϵ_r ,

dielectric material, and the addition of metal stubs to diagonal corners of the driven ring does not increase the overall antenna size.

The important advantage of this design is in the improvement in the angular coverage, which can be visualized by looking at the variations of axial ratio with elevation angle for all four cases. In Fig. 3.9, they are plotted at 1.556 GHz in the $\phi = 0^\circ$ plane. The angular ranges for which the axial ratio is below 3-dB are given in Table 3.2 for all of them. It is clear that the antenna with hybrid perturbation has a wider angular coverage, for which the 3-dB axial ratio beamwidth is 154° , from -77° to $+77^\circ$ off the boresight. However, in the $\phi = 90^\circ$ plane, all four cases have very similar performance.

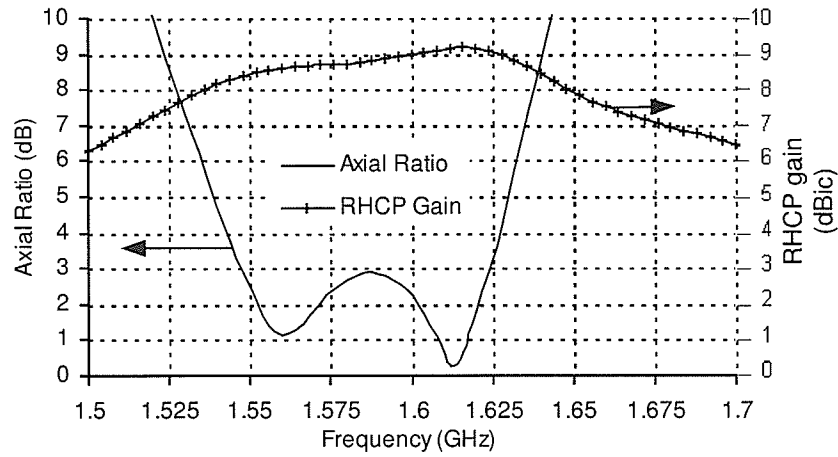
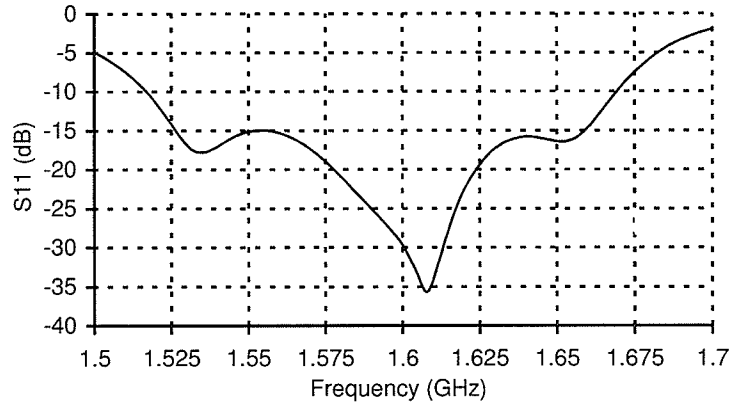
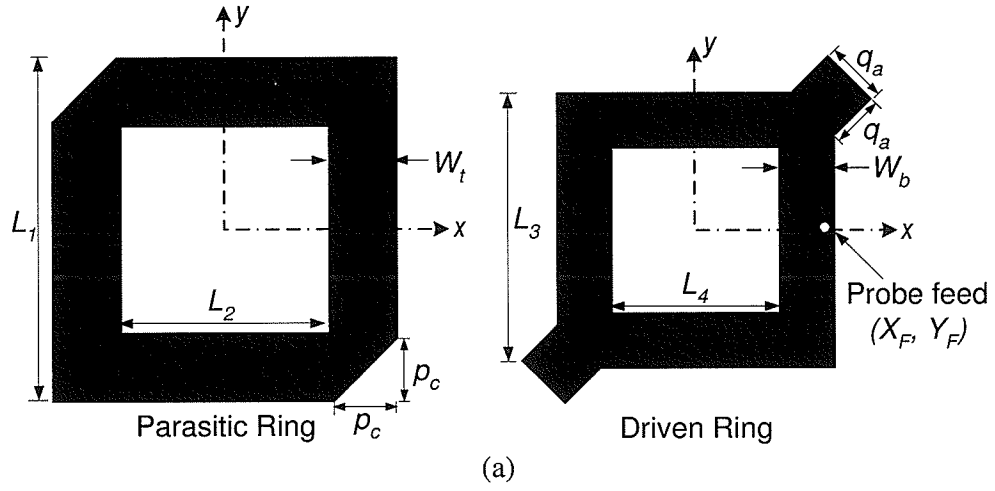


Fig. 3.8: (a) Geometry of the DLSRA with hybrid perturbation, and its simulated (b) return loss plot, and (c) axial ratio and RHCP gain vs. frequency plot. The antenna dimensions are tabulated in Table 3.2.

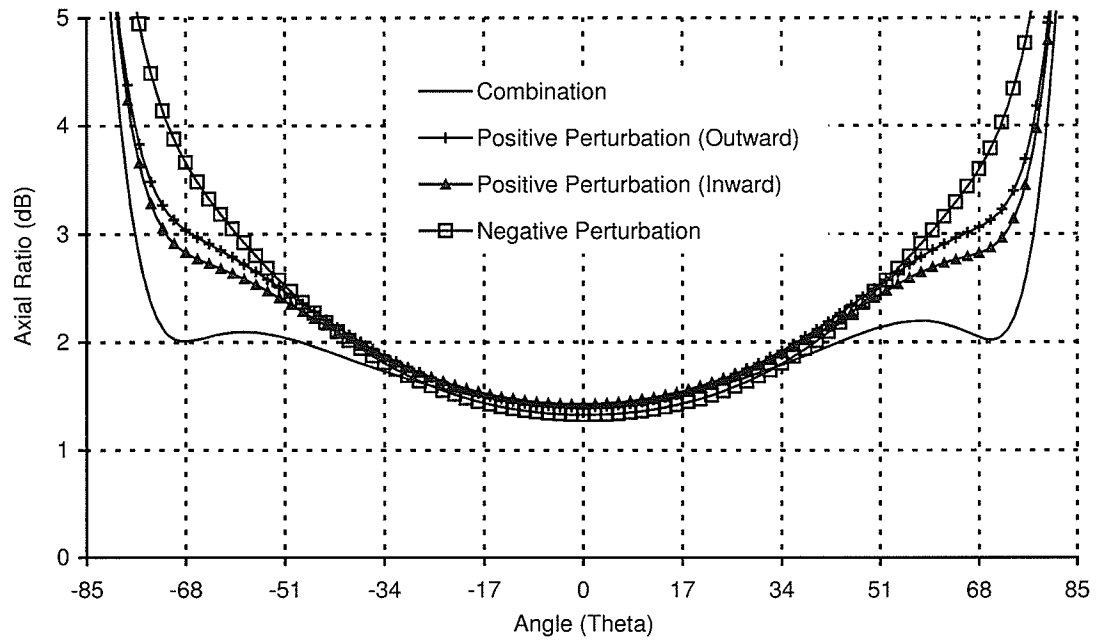
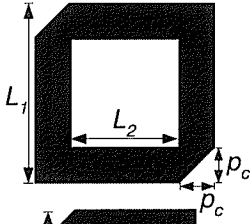
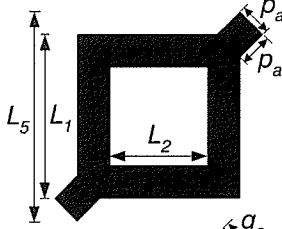
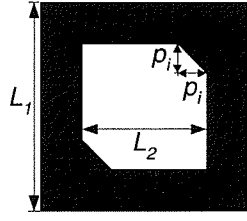
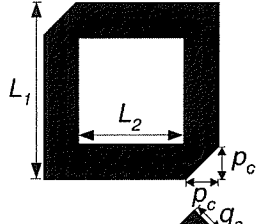
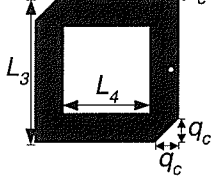
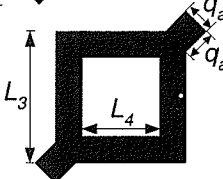
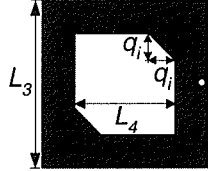
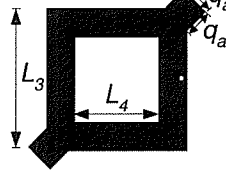


Fig. 3.9: The variations of axial ratio with elevation angle, in the $\phi = 0^\circ$ plane, for the DLSRA with positive perturbation (inward and outward), negative perturbation and hybrid perturbation, at 1.556 GHz.

Table 3.2: DLSRA antenna for CP: Optimized antenna parameters and simulated results (Foam height = 11 mm, Probe position: $X_F = 21$ mm, $Y_F = 0$)

Type	Negative Perturbation	Outward Positive Perturbation	Inward Positive Perturbation	Hybrid Perturbation
Geometry:				
Parasitic ring				
Driven ring				
Maximum Dimension (mm)	$L_1 = 59$	$L_5 = 66$	$L_1 = 59$	$L_1 = 59$
Square Ring Size (mm)	$L_1 = 59, L_3 = 47.3$	$L_1 = 59, L_3 = 44.7$	$L_1 = 59, L_3 = 47.3$	$L_1 = 59, L_3 = 44.7$
Slot Size (mm)	$L_2 = 40, L_4 = 15.3$	$L_2 = 37.3, L_4 = 14.7$	$L_2 = 39, L_4 = 15.3$	$L_2 = 39.2, L_4 = 14.7$
Perturbation (mm)	$p_c = 6.5, q_c = 8.5$	$p_a = 4.5, q_a = 6$	$p_i = 5, q_i = 6$	$p_c = 5, q_a = 6$
10-dB RL BW (MHz)	1510 to 1670 = 160	1510 to 1683 = 173	1509 to 1686 = 177	1517 to 1669 = 152
% RL BW	10.1%	10.8%	11.1%	9.5%
3-dB AR BW (MHz)	1541 to 1613 = 72	1545 to 1624 = 79	1549 to 1627 = 78	1547 to 1624 = 77
% AR BW	4.6%	5%	4.9%	4.9%
7-dBic RHCP Gain (MHz)	1505 to 1677 = 172	1505 to 1692 = 187	1513 to 1699 = 186	1515 to 1678 = 163
3-dB Beamwidth (at 1.556 GHz) [$\phi=0^\circ$ plane]	$118^\circ (-59^\circ \text{ to } +59^\circ)$	$134^\circ (-67^\circ \text{ to } +67^\circ)$	$144^\circ (-72^\circ \text{ to } +72^\circ)$	$154^\circ (-77^\circ \text{ to } +77^\circ)$

3.3 Effects of finite ground plane on CP performance of the DLSRA

3.3.1 Ground plane size

In the above simulation studies, an infinite ground plane was considered. For practical applications, however, a finite ground plane has to be used, and it will obviously affect the axial ratio and CP gain of the antenna. Fig. 3.10 shows the variation of axial ratio with frequency, of the antenna with outward positive perturbation [see Fig. 3.6(a) for the geometry], for different ground plane sizes. Here, the antenna is symmetrically placed at the center of the ground plane. The axial ratio deteriorates by decreasing the ground plane size. Between the two dips in the axial ratio plot, caused by the perturbations on both rings, the second dip suffers the most, which moves to higher frequencies and shows poor axial ratio. In order to improve the axial ratio, for different ground plane sizes, the driven ring is adjusted mainly because, the second dip is due to the driven ring. At the same time, the foam thickness is also increased to achieve lower values of the axial ratio. Thus, by further optimizing the driven ring size, and the separation between the two rings, good CP performance can be recovered even for smaller ground plane sizes, while keeping the parasitic ring size and perturbations fixed.

The simulation results are listed in Table 3.3, for the optimized cases for different ground plane sizes. Since the driven ring size is increased in all cases, a shift of axial ratio plot, to the lower frequency region, can be observed in Fig. 3.11(a). When the ground plane size decreases, RHCP gain decreases, as can be seen in Fig. 3.11(b). For a

ground plane size of $80 \times 80 \text{ mm}^2$, the peak RHCP gain is 7.89 dBic, whereas it is 9.2 dBic when the ground plane size is $160 \times 160 \text{ mm}^2$, as it is evident in Fig. 3.11(b).

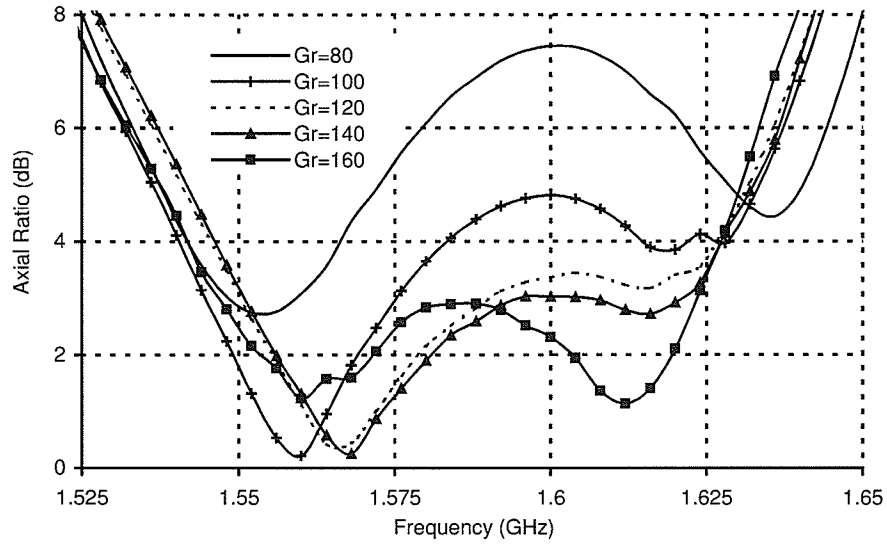


Fig. 3.10: The variation of axial ratio with frequency, due to different ground plane sizes for the DLSRA antenna with positive perturbation in Fig. 3.6(a). Antenna parameters (in mm) are: $L_1 = 59$, $L_2 = 37$, $L_3 = 44.5$, $L_4 = 14.5$, $p_a = 5$, $q_a = 6$, $\epsilon_r = 3.2$, $h_1 = 1.6$, $h_2 = 11$. Gr=80 means ground plane size = $80 \times 80 \text{ mm}^2$, Gr=100 means ground plane size = $100 \times 100 \text{ mm}^2$ and so on.

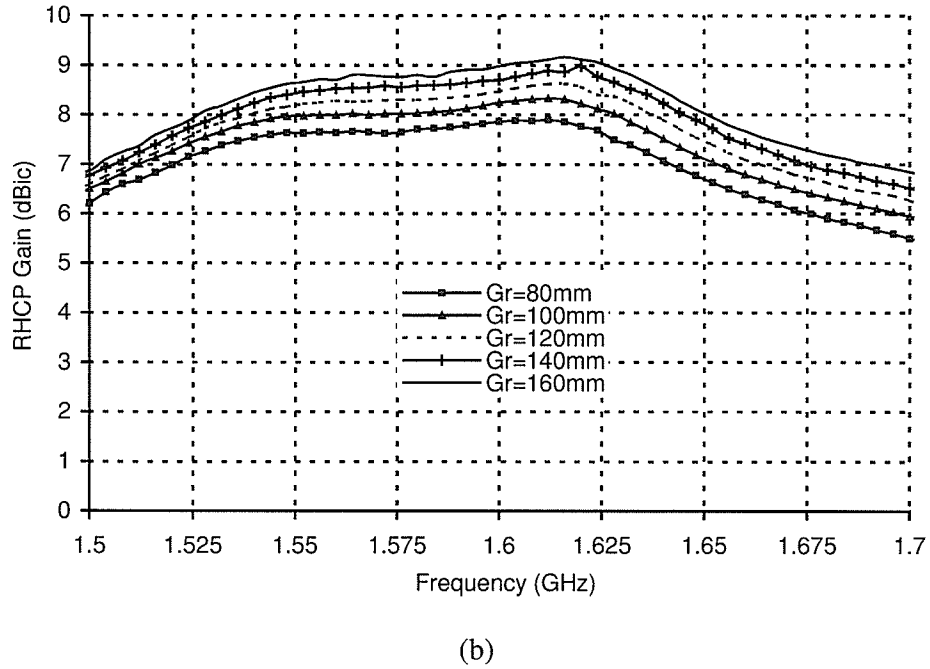
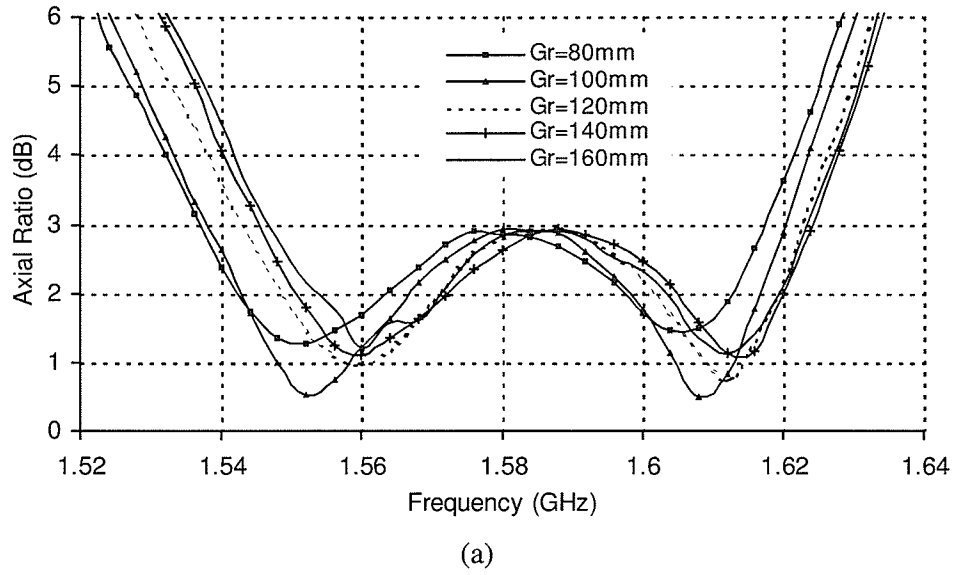


Fig. 3.11: The effects of finite ground plane sizes on the (a) axial ratio and (b) RHCP gain of the DLSRA antenna with positive perturbation in Fig. 3.6(a). Antenna parameters are mentioned in Table 3.3. Gr=80 means ground plane size = $80 \times 80 \text{ mm}^2$, Gr=100 means ground plane size = $100 \times 100 \text{ mm}^2$ and so on.

Table 3.3: Positively perturbed DLSRA CP antenna [Fig. 3.6(a)] with finite ground plane: optimized antenna parameters and simulated results. Other antenna parameters: $L_1 = 59$ mm, $L_2 = 37$ mm, $p_a = 5$ mm, $q_a = 6$ mm

Driven ring size (mm)	Ground Plane (mm ²)	Foam Height (mm)	10-dB RL BW (MHz)	3-dB axial ratio BW (MHz)	7-dBic RHCP Gain (MHz)
$L_3 = 44.5$ $L_4 = 14.5$	160×160 ($0.84\lambda_o$)	11mm	1516-1688 =172	1547-1624 =77	1502-1690 =188
$L_3 = 44.7$ $L_4 = 14.7$	140×140 ($0.74\lambda_o$)	11.2mm	1511-1682 =171	1545-1624 =79	1506-1674 =168
$L_3 = 44.8$ $L_4 = 14.8$	120×120 ($0.63\lambda_o$)	11.5mm	1508-1679 =171	1543-1623 =80	1510-1664 =154
$L_3 = 44.9$ $L_4 = 14.9$	100×100 ($0.53\lambda_o$)	12.8mm	1509-1673 =164	1538-1620 =82	1512-1653 =141
$L_3 = 45$ $L_4 = 15$	80×80 ($0.42\lambda_o$)	16.7mm	1502-1667 =165	1537-1618 =81	1520-1642 =122

3.3.2 Asymmetric antenna position on the ground plane

In the ground plane size study in Section 3.3.1, a symmetric antenna position on the ground plane was considered. In order to see the effects of asymmetric locations, the DLSRA CP antenna is positioned asymmetrically on the ground plane as shown in Fig. 3.12. Considering $P(X_g, Y_g)$ as the center of the ground plane, when the antenna on the ground plane is asymmetric about the y-axis (with $X_g = 0$ mm), the axial ratio performance does not deteriorate much, as can be seen in Fig. 3.13(a). Here, $X_g = 0$ mm,

$Y_g = 0$ mm, indicates the symmetric case, and $X_g = 0$ mm, and $Y_g = 18$ mm means the DLSRA antenna is at one side of the ground plane. When the antenna is asymmetric about the x -axis (keeping $Y_g = 0$ mm), the axial ratio performance degrades significantly, as shown in Fig. 3.13(b). Similarly, when the antenna is asymmetrically positioned about both x - and y - axes, the axial ratio suffers significantly, as shown in Fig. 3.13(c).

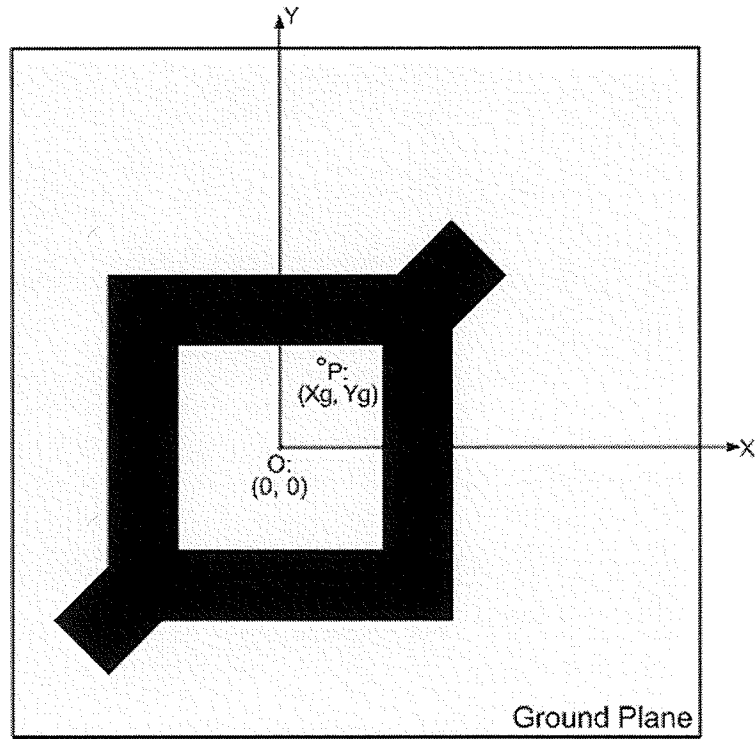


Fig. 3.12: Antenna geometry with the ground plane in order to study the effects of asymmetric antenna position on the ground plane on the axial ratio of the DLSRA with positive perturbation, Fig. 3.6(a). Antenna parameters (in mm) are: $L_1 = 59$, $L_2 = 37$, $L_3 = 44.9$, $L_4 = 14.9$, $P_a = 5$, $q_a = 6$, $\epsilon_r = 3.2$, $h_1 = 1.6$, $h_2 = 12.8$. Ground plane size = $100 \times 100 \text{ mm}^2$.

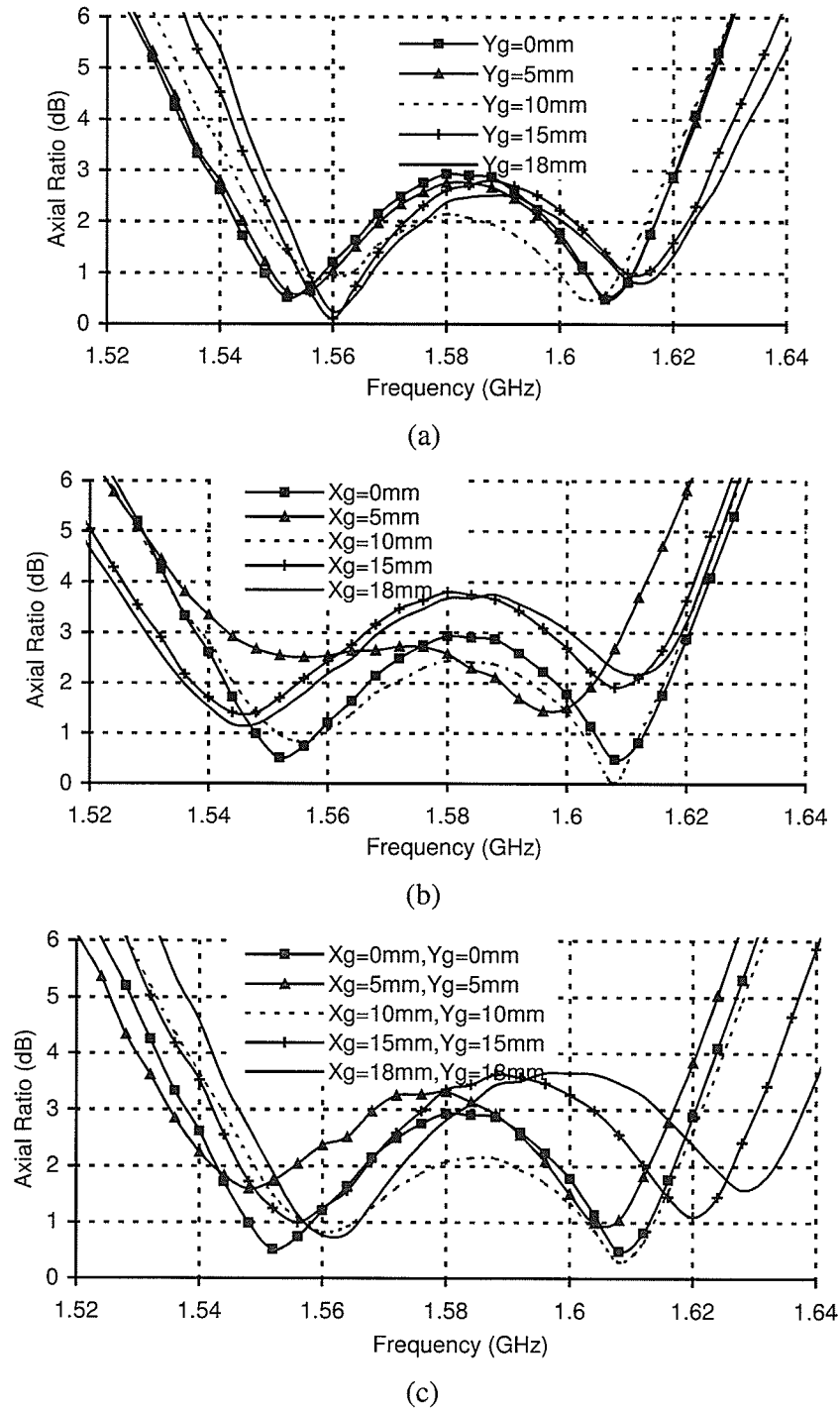


Fig. 3.13: The effects of asymmetric antenna position on the ground plane on the axial ratio of the DLSRA with positive perturbation, in Fig. 3.12: (a) when asymmetric about y-axis, with $X_g = 0$, (b) when asymmetric about x-axis, with $Y_g = 0$, and (c) when asymmetric about both x- and y- axes.

3.4 Experimental study

In the previous sections, miniaturized microstrip ring antennas are investigated, and thus the ground plane is also made small. The simulation studies showed that the antenna performance, especially the gain and axial ratio, depend strongly on the ground plane size. It is important, therefore, to study experimentally the performance of a fabricated antenna, which will be influenced by both fabrication tolerances and the presence of nearby objects, as the ground plane is small to shield the antenna. Thus, a CP DLSRA CP antenna, with outward positive perturbations [Fig. 3.6(a)], was fabricated, where a substrate with dielectric permittivity $\epsilon_r = 3.2$, and thickness $h_1 = 1.6$ mm, is used for the driven ring, and foam ($h_2 = 11$ mm) for separating the parasitic ring. The other dimensions of the antenna are (in mm): $L_1 = 59$, $L_2 = 37$, $L_3 = 44.5$, $L_4 = 14.5$, $p_a = 5$, $q_a = 6$. The bottom ring was excited at $X_F = 21$ mm, $Y_F = 0$ mm, using a 50- Ω SMA probe. The parasitic ring was made from a copper tape, hand cut to its shape, and placed over the foam, which was kept on the lower substrate by tapes around its edges.

The antenna was tested in the Antenna Laboratory at the University of Manitoba. The return loss was measured by ANRITSU ME7808A Network Analyzer, and compared in Fig. 3.14(a) with the simulation results obtained from Ansoft Ensemble 8.0. For measurement, a finite ground plane (160×160 mm²) was used, which is also considered in the simulation. The measured S_{11} is slightly different from simulation, but the variations are below -10 dB, making the corresponding bandwidths about the same, Fig.

3.14(a). Considering the tolerances of the hand cut and taped parasitic ring, the S_{11} results are satisfactory.

The measured and simulated axial ratio and RHCP gains are compared in Fig. 3.14(b). The measured 3-dB axial ratio bandwidth is larger (81 MHz) than the simulated one (76 MHz) and it also has lower minima, as low as 0.32 dB at 1.565 GHz. In other words, the fabrication tolerances have improved the axial ratio performance.

The measured gains also agree well with simulations, and are somewhat higher at low frequencies. There are small oscillations in the measured gain, which could be due to calibration errors, fabrication tolerances or interactions between the antenna and its support. A sample of the measured radiation patterns, using a rotating linear source, is shown in Fig. 3.15. The boresight CP performance is quite good, but deteriorates gradually with increasing angle, a common characteristic of CP antennas.

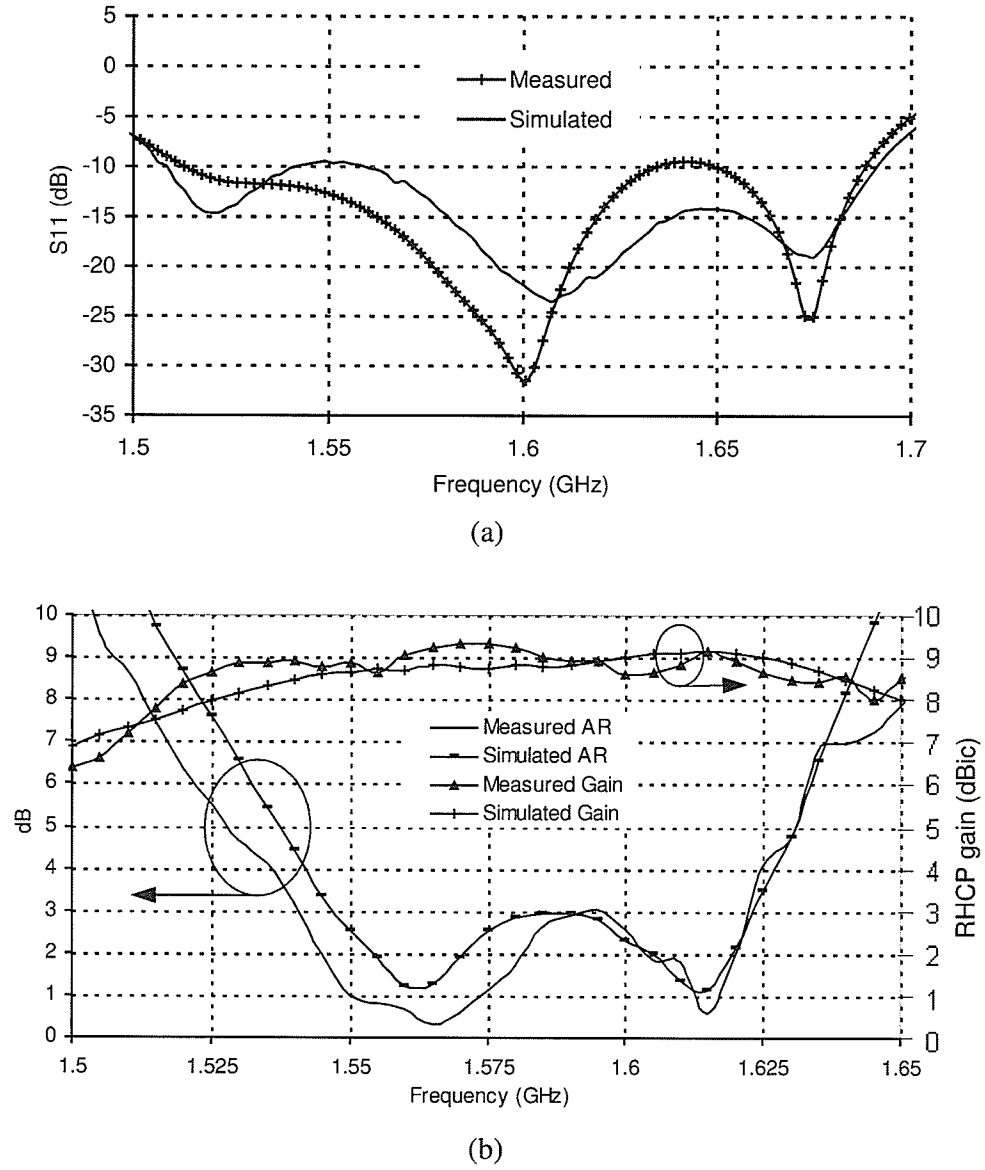


Fig. 3.14: Comparison between simulated and measured (a) return loss and (b) axial ratio and RHCP gain of the DLSRA, with positive perturbation [Fig. 3.6(a)]. The antenna parameters are (in mm): $\epsilon_r = 3.2$, $h_1 = 1.6$, $h_2 = 11$, $L_1 = 59$, $L_2 = 37$, $L_3 = 44.5$, $L_4 = 14.5$, $p_a = 5$, $q_a = 6$. The finite ground plane size is 160×160 mm².

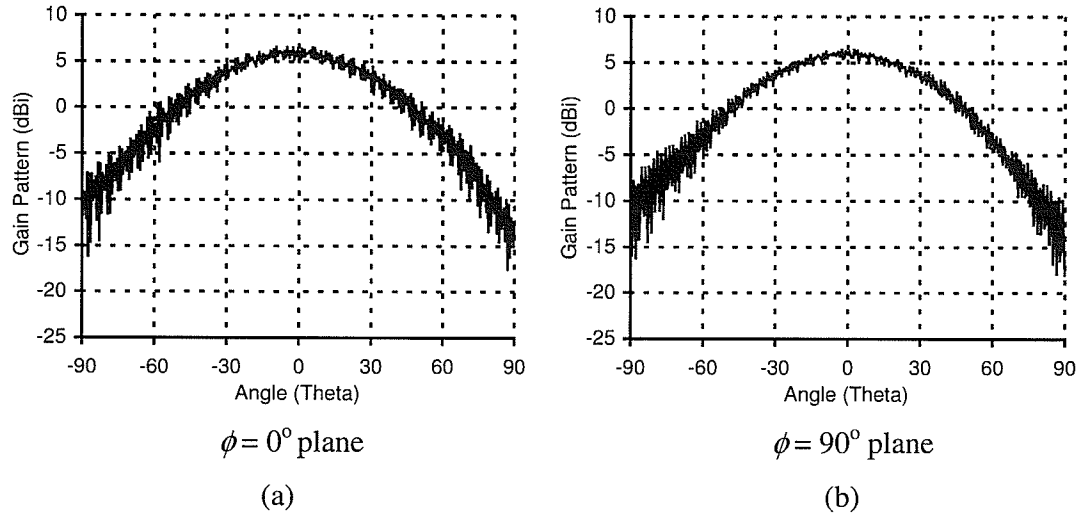
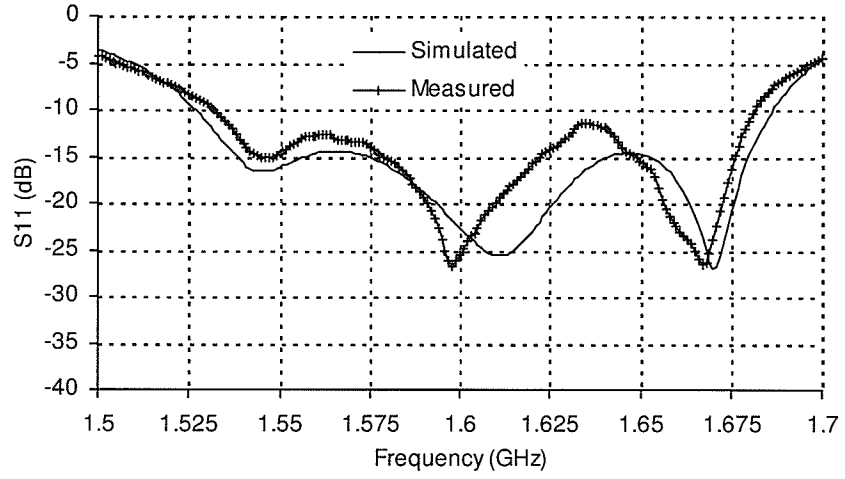
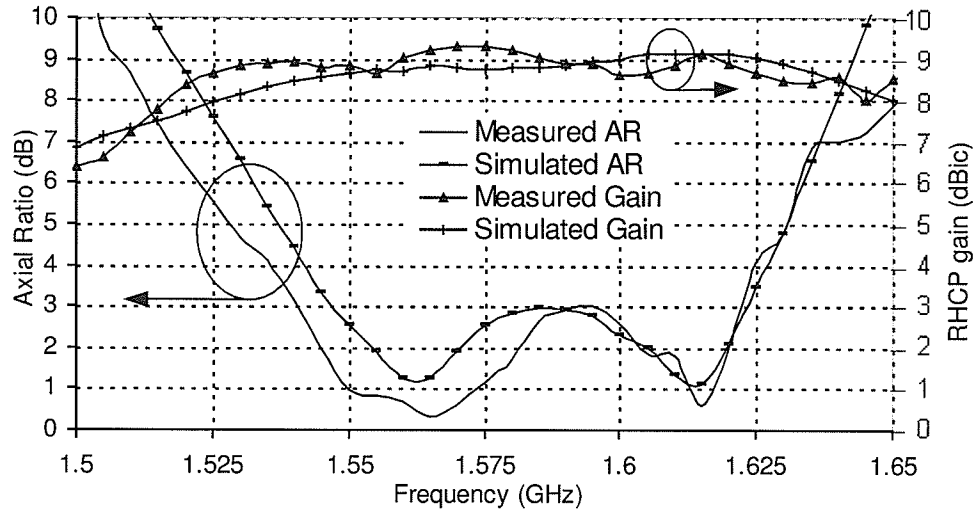


Fig. 3.15: The measured gain patterns in (a) $\phi = 0^\circ$, and (b) $\phi = 90^\circ$ planes at 1.56 GHz of the DLSRA, with positive perturbation [Fig. 3.6(a)].

Secondly, the DLSRA CP antenna with hybrid perturbation, as shown in Fig. 3.8(a), was fabricated following the same method, and tested and compared with the simulated results, as shown Fig. 3.16, which show good agreement as the first example. In order to confirm the wide axial ratio beamwidth property of this hybrid-perturbed stacked square ring antenna, its measured and simulated axial ratios against the elevation angle are plotted in Fig. 3.17 at 1.556 GHz. The comparisons are tabulated in Table 3.4, showing that the stacked square ring antenna with hybrid perturbation shows wide impedance and axial ratio bandwidths similar to the negatively perturbed antenna, and wider axial ratio beamwidth around the boresight direction. The peak RHCP gain is 9.75 dBic.



(a)



(b)

Fig. 3.16: Comparison between simulated and measured (a) return loss and (b) axial ratio and RHCP gain of the DLSRA, with hybrid perturbation [Fig. 3.8(a)]. The antenna parameters are (in mm): $\epsilon_r = 3.2$, $h_1 = 1.6$, $h_2 = 11$, $L_1 = 59$, $L_2 = 39.2$, $L_3 = 44.7$, $L_4 = 14.7$, $p_c = 5$, $q_a = 6$. The finite ground plane size is $160 \times 160 \text{ mm}^2$.

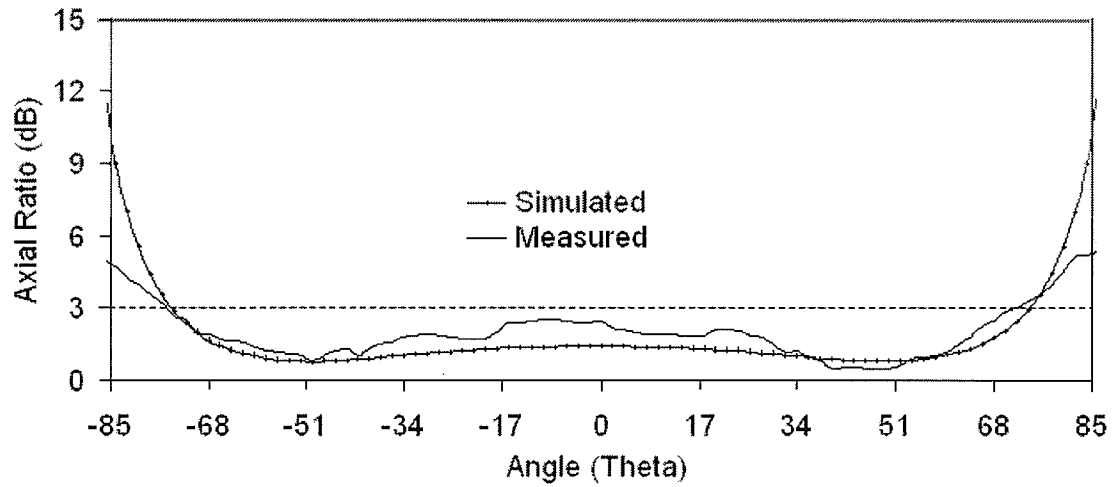


Fig. 3.17: Measured and simulated axial ratios with elevation angle, in the $\phi = 0^\circ$ plane, of the DLSRA with hybrid perturbations.

Table 3.4: Comparison of simulated and measured results of the stacked square ring antenna with hybrid perturbations

	Simulated results	Measured results
10-dB RL Bandwidth	1527 to 1687 MHz = 160 MHz (10%)	1.532 to 1.682 MHz = 150 MHz (9.33%)
3-dB AR Bandwidth	1559 to 1635 MHz = 76 MHz (4.8%)	1551 to 1637 MHz = 86 MHz (5.4%)
7-dBic RHCP Gain Bandwidth	1515 to 1710 MHz = 195 MHz	1508 to 1698 MHz = 190 MHz
3-dB AR Beamwidth (1.556 GHz) ($\phi = 0^\circ$ plane)	148.5° (from -74.5° to +74°)	147° (from -75° to +72°)

3.5 Conclusion

Achieving a wide axial ratio bandwidth from a singly-fed microstrip antenna is a challenging problem. Dealing with a microstrip square-ring antenna with a single-point feed, for circular polarization, is even more challenging, because it is a miniaturized antenna, which inherently has a very narrow axial ratio bandwidth. In this chapter, wide axial ratio bandwidths are achieved with the help of stacking square rings and introducing perturbations to both driven and parasitic rings.

A novel approach, called hybrid perturbation scheme, is also presented to broaden the axial ratio bandwidth. In this case, the sequential rotation method was used to rotate one ring by 90° . This rotation required its corner perturbation to be of the opposite sense, to maintain the circular polarization of the stacked configuration. The simulated and measured axial ratios of prototype antenna, with hybrid corner perturbations, confirmed its wide axial ratio beamwidth. It was shown that small ground plane sizes deteriorate the circular polarization performance of the DLSRA, which can be recovered by further optimizing the antenna parameters and by increasing the separation between the two rings. It was found that it is important to have a symmetric ground plane for the CP antenna, and the asymmetric position of the antenna on the ground plane degrades the CP performance.

CHAPTER FOUR

Square Ring Antenna for Multi-Frequency Operation

4.1 Introduction

Stacked square ring antennas, presented in the previous chapter, can perform both wideband and dual band operation. In this chapter, the study is extended to achieve tri-band operation from the square ring antenna. By taking advantage of accommodating the third ring within the parasitic ring of the dual square ring antenna (DLSRA) configuration, the antenna can be operated at three different frequencies. In this chapter, a generalized design method is discussed to obtain an antenna that can be operated at three different frequencies. The feeding mechanism is described briefly. Then, its performance is discussed with its limitations and problems. A representative design example is presented to cover three GPS frequencies to show its practical application.

4.2 General design guideline for multi-frequency operation from stacked square ring antenna

As mentioned earlier, like the stacked microstrip antenna, the stacked square ring antenna can perform both broadband and dual band operations. However, the stacked

square ring antenna has an advantage of having perforation at the middle of each ring, where a third ring can be accommodated which will give another resonance. To fit this ring, both the parasitic ring and the inner ring have to be made narrower for particular frequencies; and this leads to the problem of impedance mismatch. It was mentioned earlier that the width of the ring has to be a certain value ($L_2/L_1 < 0.4$) to enable the excitation by a 50- Ω SMA probe-feed. Moreover, the feeding of the third ring itself is another challenging issue, because of the presence of the driven ring in the bottom layer. In [53], an inside capacitive feeding technique has been suggested, where the feed strip is located inside the ring, thus not requiring any extra antenna real estate. The width of the ring is also narrow in this case.

Based on the above discussion, an antenna design has been developed. The three dimensional configuration of the antenna is depicted in Fig. 4.1(a) and important antenna parameters are labeled in Figs. 4.1(b) and 4.1(c) for better understanding. It consists of a square ring (ring # 1) on a grounded dielectric substrate having dielectric constant ϵ_{r_1} , and thickness h_1 , and two concentric square rings on another substrate layer having dielectric constant ϵ_{r_2} and thickness of h_2 . In this design, the bottom ring (ring # 1) is capacitively excited by a feed line located outside the ring at a distance d_1 . The inner ring on the top layer (ring # 3) is also excited in a similar fashion using an inside feed line separated by a distance d_2 from one arm of the ring. A small hole can be created on ring # 1 to pass the probe to excite the feed line for ring # 3, if needed. The outer ring on the top layer (ring # 2) can be electromagnetically excited by ring # 1, as a parasitic resonator.

The ring sizes are chosen such that rings # 1, 2 and 3 operate at three frequencies: f_1 , f_2 and f_3 , respectively, where $f_1 < f_2 < f_3$.

The simulated scattering parameters of such an antenna, obtained from ‘Method of Moments’- based commercial software ‘Ansoft Designer version 3’, are plotted in Fig. 4.2. Here, for each ring TM_{11} mode gets excited. Note that f_1 and f_2 are close due to the fact that rings # 1 and 2 work as stacked antenna configuration. Therefore, their sizes are chosen to be close so that the driven ring is efficiently coupled to the parasitic ring. Since, ring # 3 is inside ring # 2, its physical size is limited and its frequency of operation for the fundamental mode must be greater than that of ring # 2, i.e. $f_3 > f_2$. Moreover, it has been found that its impedance properties do not change much due to changes in other rings. This indicates that, along with its feed line, this antenna can be designed independently to operate at a higher frequency than ring # 2.

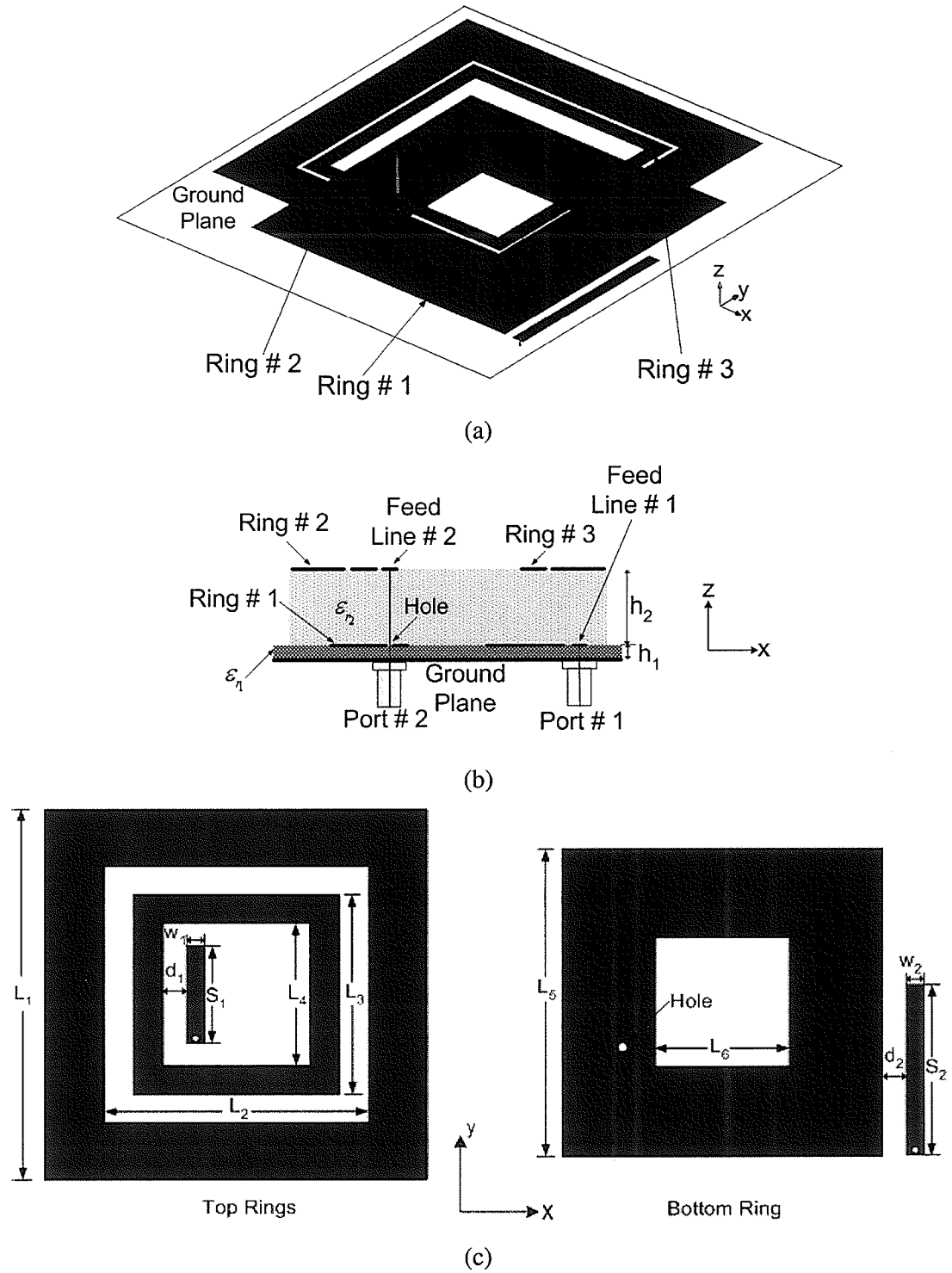


Fig. 4.1: Geometry of the proposed antenna with capacitively-fed multiple square rings for multi-frequency operation: (a) 3-D view, (b) side view, (c) top and bottom rings.

As an example, the antenna parameters for three frequencies, $f_1 = 1.161$ GHz, $f_2 = 1.219$ GHz and $f_3 = 1.56$ GHz are mentioned in Table 4.1. First, sizes of rings # 1 and 2 are determined based on their dielectric substrate and required frequencies. Substrate parameters chosen are $\epsilon_r = 2.5$, $h_1 = 1.57$ mm, and $\tan\delta = 0.0019$, and $\epsilon_r = 1.07$. When capacitive feeding is used, a narrower width of the ring can be chosen. For example, in this case, $L_2/L_1 = 0.78$ and $L_6/L_5 = 0.52$, (the ratios are greater than 0.4). Now, the size of the third ring can be chosen such that it fits inside ring # 2 on the top layer. For this ring, $L_3/L_4 = 0.83$, which indicates a very narrow width of the ring. Finally, the length and width of feed for ring # 3 are optimized to obtain better impedance matching for all three square rings to be operated at three frequencies, as shown in Fig. 4.2. The isolation between the two ports in the two layers is below -30 dB.

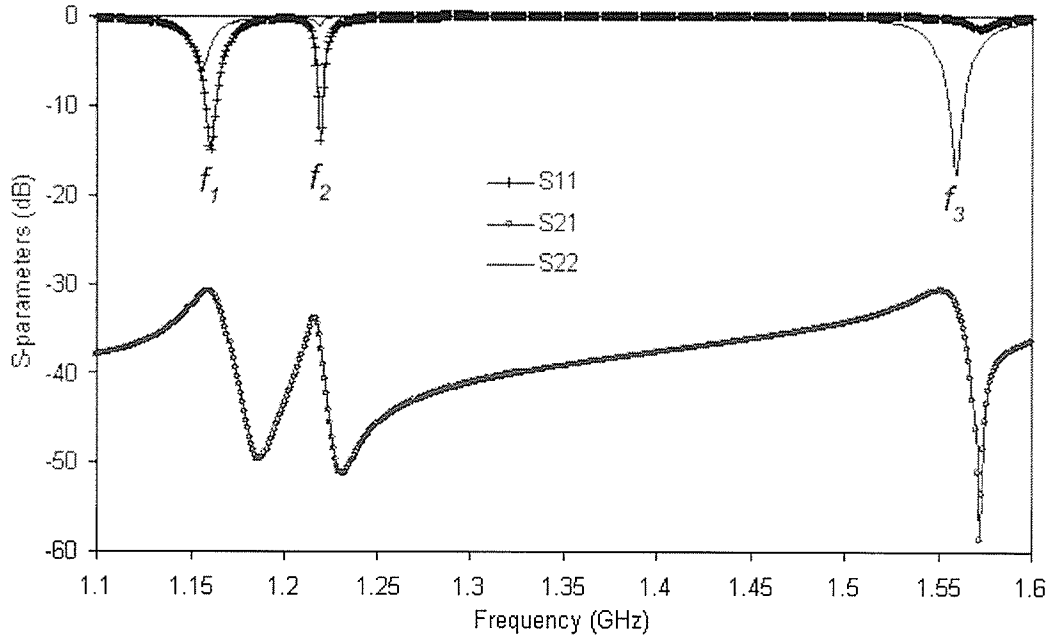


Fig. 4.2: Simulated scattering parameters of the antenna in Fig. 4.1, showing three resonances and good isolation between two ports.

Table 4.1: Design parameters for the antenna with multiple rings (Fig. 4.1) for tri-frequency operation

Ring # 1	L_1	72 mm
	L_2	56.5 mm
	L_2/L_1	0.78
Ring # 2	L_3	54 mm
	L_4	45 mm
	L_4/L_3	0.83
Ring # 3	L_5	60 mm
	L_6	31 mm
	L_6/L_5	0.52
Lower Layer Feed Line	d_2	2 mm
	S_2	41 mm
	w_2	4 mm
Upper Layer Feed Line	d_1	4.5 mm
	S_1	22 mm
	w_1	4 mm
Lower Substrate	ϵ_{r_1}	2.5
	h_1	1.6 mm
Upper Substrate	ϵ_{r_2}	1.03
	h_2	6 mm

The gain patterns for this antenna in two principal planes at three frequencies ($f_1 = 1.161$ GHz, $f_2 = 1.219$ GHz, and $f_3 = 1.56$ GHz) are shown in Fig. 4.3. The antenna shows a boresight gain of about 6 dBi at all three frequencies. However, the cross-polar level is high at all three frequencies. Particularly at 1.56 GHz, the cross-polar level is 4.26 dBi,

and it suggests that the antenna is a good candidate for circular polarization applications. Later, an example will be shown where a design is presented to cover three GPS frequencies with this antenna having multiple rings.

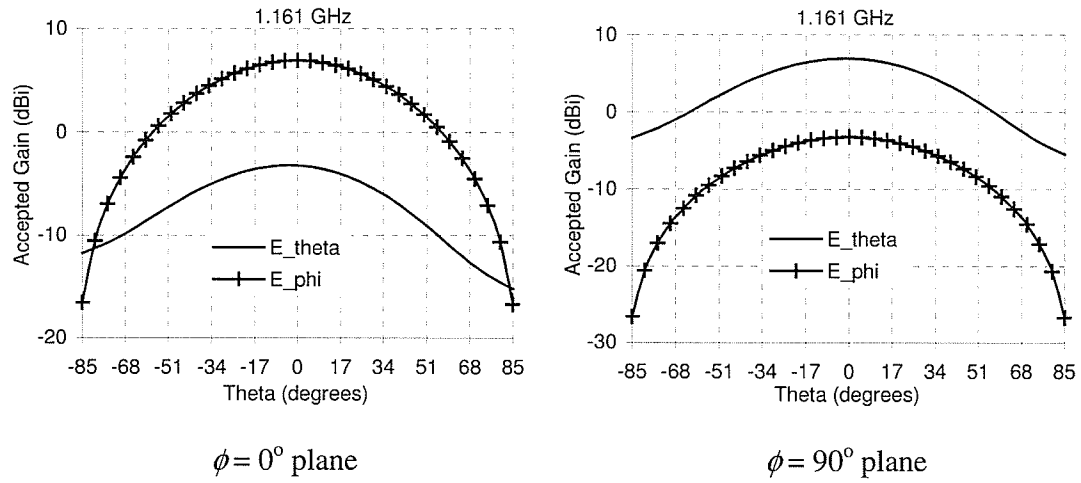


Fig. 4.3: Radiation patterns at $f_1 = 1.161$ GHz in two principal planes of the antenna in Fig. 4.1 with design parameters mentioned in Table 4.1.

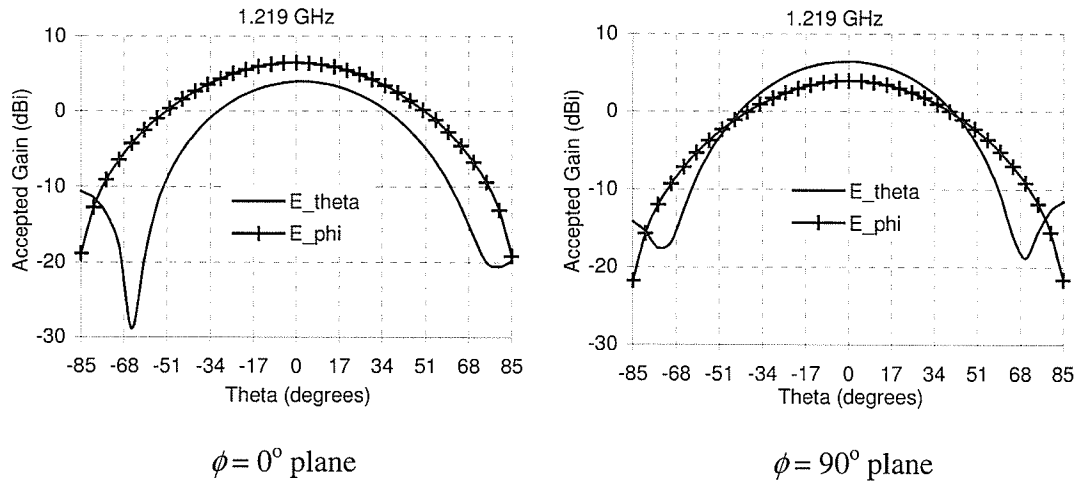


Fig. 4.4: Radiation patterns at $f_2 = 1.219$ GHz in two principal planes of the antenna in Fig. 4.1 with design parameters mentioned in Table 4.1.

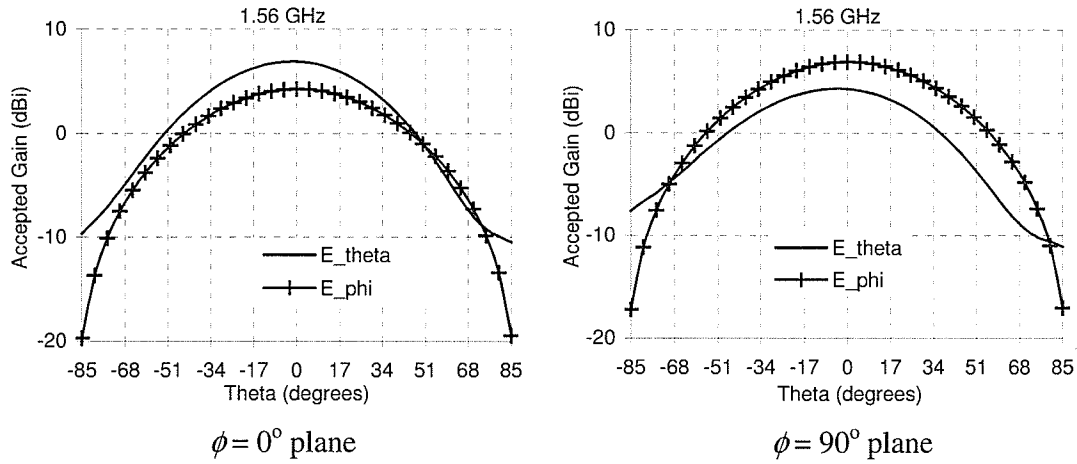


Fig. 4.5: Radiation patterns at 1.56 GHz in two principal planes of the antenna in Fig. 4.1 with design parameters mentioned in Table 4.1.

4.3 Confirmation by Ansoft HFSS

To validate the design method described in the previous section and to confirm the results obtained from Ansoft Designer, version 3.0, a stacked square ring antenna with capacitive feeding for multi-frequency operation is modeled in Ansoft HFSS, version 10, which is a finite-element-method based software. Design parameters used in the modeling are the same as in Table 4.1. Simulated S-parameters, obtained from HFSS, are plotted in Fig. 4.6. The results, obtained from Ansoft HFSS and Designer, are compared in Table 4.2. The resonances occurred approximately at the same frequencies in both cases, indicating good agreement between simulation results. In the case of HFSS, the simulated isolation S_{12} is below -25 dB, except at 1.21 GHz. Considering two different computational techniques, it can be concluded that the results are in good agreement, and it also confirms the analysis results from Designer.

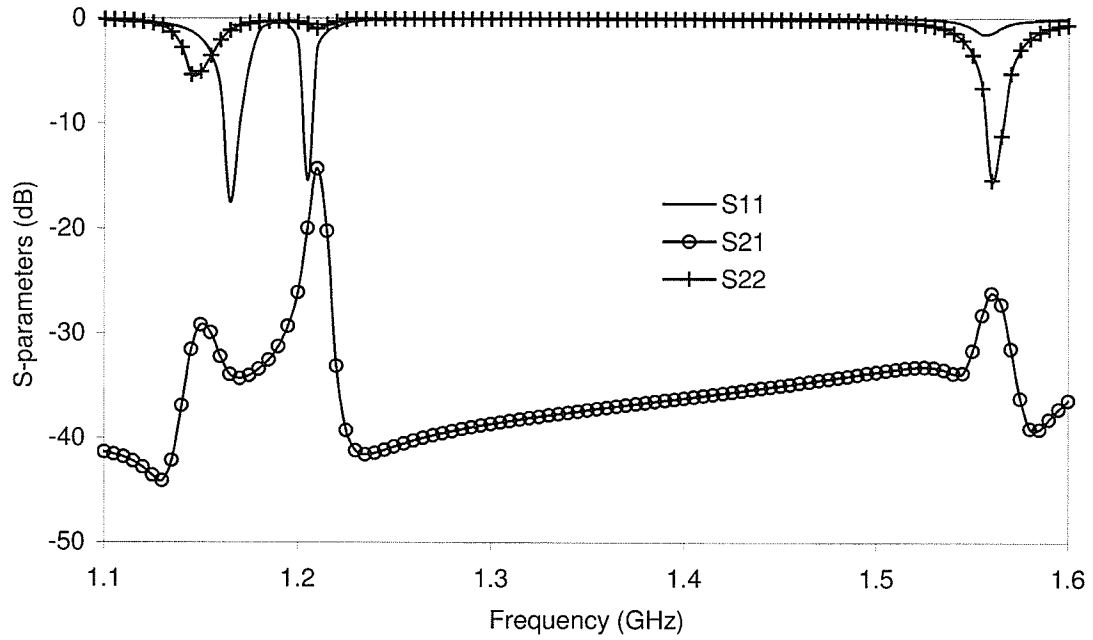


Fig. 4.6: Simulated scattering parameters, using Ansoft HFSS (Finite Element Method-based software package), of the antenna in Fig. 4.1.

Table 4.2: Simulation results of the stacked square ring antenna for multi-frequency operation, Fig. 4.1, from two software packages: Ansoft Designer and Ansoft HFSS.

Antenna parameters are mentioned in Table 4.1

Software	Ansoft Designer	Ansoft HFSS
f_1	1.161 GHz	1.165 GHz
S_{11} at f_1	-15 dB	-17.5 dB
f_2	1.219 GHz	1.205 GHz
S_{11} at f_2	-14 dB	-15.3 dB
f_3	1.56 GHz	1.56 GHz
S_{11} at f_3	-17.5 dB	-15.4 dB
S_{21}	Below -30 dB	Below -26 dB (except -14 dB at 1.21 GHz)

4.4 A Design for tri-frequency global positioning system (GPS)

A practical application of such an antenna, presented in the previous sections, is the Global Positioning System (GPS). GPS has now been considered as the future of aviation and transportation for most civil and military applications. A major modernization effort is now in progress, which includes an introduction of a third civil signal, located at 1176.45 MHz (L5) with the existing two civilian signals L1 (1575.42 MHz), and L2 (1227.60 MHz) [59, 60]. Existing L1 and L2 bands are for civil aviation safety-of-life services, and L5 band is for general use in non-safety critical applications [60, 61]. With access to all three signals, both civilians and military will benefit from a high-precision global positioning system with increased availability of reliable navigation operations, and improvement in the interference mitigation.

As part of the modernization effort of the GPS, bandwidths of L1 and L2 signals are extended to 24 MHz from 20 MHz, along with 24 MHz bandwidth for L5 signal. Several successful dual band designs are available in the literature to cover L1 and L2 frequencies [62-65]. However, it is a challenging task to integrate all three bands on a single antenna element. Another important issue is that the new band (L5) frequency is lower than those of L1 and L2 bands, and a typical design will lead to a large size antenna. Researchers have recently attempted to design tri-band antennas. For example, Rao et. al. [66] proposed an antenna array having four inverted L elements with trap loading that covers three GPS bands. The antenna has a large aperture size ($0.5 \lambda_0$ at L5 frequency) and thickness (22 mm or $0.086 \lambda_0$ at L5 frequency). To minimize the antenna

size, high permittivity substrates (ϵ_r of 12 and 25) are used in [67], where further miniaturization is achieved by using F-shaped configuration of four elements. Again, the overall height of this antenna is large (20 mm or $0.078 \lambda_0$ at L5 frequency). Instead of using arrays of element, stacked resonator concept is used in [68, 69] to cover three GPS frequencies. Zhou et. al. [68] presented a proximity-coupled stacked patch design, again with high permittivity substrates (ϵ_r of 16 and 30), where two L-shaped probe feeds were used to excite the patches and generate CP. The overall height of the antenna is smaller in this case (12.8 mm or $0.05 \lambda_0$ at L5 frequency). In [69], authors used the same stacked-resonator concept, however used circular patches instead of square patches. In all these designs mentioned above, mainly dual-band antennas are designed, where the lower band covers L2 and L5 bands, and the upper band covers L1 band.

The geometry of a multi-frequency antenna, developed in this study, has already been given in Fig. 4.1. Since L2 and L5 are two adjacent bands, rings # 1 and 2 are chosen to work as stacked rings, so that they can offer wide enough bandwidth to cover both L2 and L5 bands. The third ring size is chosen independently to cover L1 band. The dimensions are given in Table 4.3. A low permittivity material is used for the bottom layer, whereas foam is chosen for the top layer, as mentioned in Table 4.3. The overall height of the antenna is 15.6 mm ($0.06 \lambda_0$ at L5 frequency). The size of ring # 2, which basically determines the antenna size, is 77 mm or only $0.3 \lambda_0$ at L5 band frequency. Fig. 4.7 shows the return loss plot of this antenna. Since a stacked configuration is realized by rings # 1 and 2, a wider impedance bandwidth of about 75 MHz or 6.2% (1164 MHz to 1239 MHz) is achieved to cover both L2 and L5 bands. Because of Ring # 3, the higher

mode frequency becomes excited at L1 band with an impedance bandwidth of 29 MHz (1561 MHz to 1590 MHz). The isolation between two input ports of the antenna is below -20 dB. These results are obtained from Ansoft Designer, version 3.

Table 4.3: Multiple square ring antenna [Figs. 4.1] parameters for GPS frequencies

Ring # 1	L_1	77 mm
	L_2	53.5 mm
Ring # 2	L_3	52 mm
	L_4	43.5 mm
Ring # 3	L_5	66.5 mm
	L_6	23 mm
Lower layer feed line	d_2	0.2 mm
	S_2	40 mm
	w_1	0.5 mm
Upper layer feed line	d_1	5 mm
	S_1	22 mm
	w_2	4 mm
Lower substrate	ϵ_{r_1}	2.5
	h_1	1.6 mm
Lower substrate	ϵ_{r_2}	1.03
	h_2	14 mm

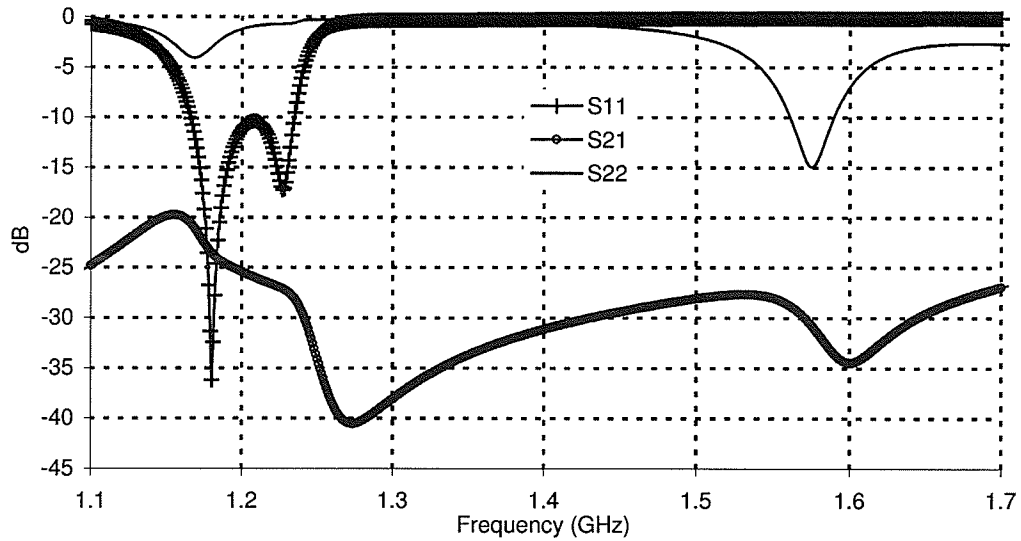


Fig. 4.7: Return loss of the antenna in Fig. 4.1 with the antenna parameters mentioned in Table 4.3.

Now, right hand circular polarization (RHCP) is required for GPS, which can be easily achieved for this antenna using two feed lines for each of ring # 1 and ring # 3, as shown in Fig. 4.8. Two feed lines on each layer will be excited with a phase difference of 90° to generate two equal but orthogonal modes in the rings. Phase shifters can be employed to excite the two feed lines with a 90° phase shift, which can be accommodated on the bottom side of the ground plane. The CP performance of this antenna is shown in Figs. 4.9 and 4.10. The axial ratio is below 3 dB up to 1.272 GHz, covering nicely L5 and L2 bands. For the higher band, the axial ratio bandwidth is 81 MHz, well above the required 24 MHz bandwidth around 1575 MHz. The CP gains are better than those in previously mentioned publications, as shown in Fig. 4.10. 7-dBic right hand CP (RHCP) gain bandwidth is 133 MHz for the lower two bands, and 112 MHz for the higher band. The LHCP gain is also mostly below -10 dBic indicating very good CP performance.

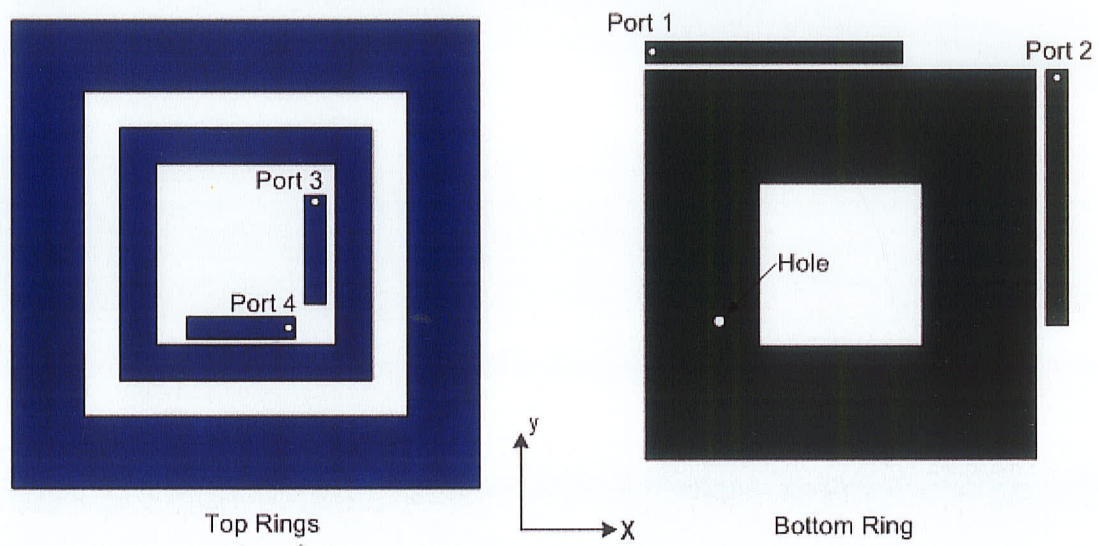


Fig. 4.8: Dual-feed arrangement of the multiple square ring antenna [Fig. 4.1] to obtain circular polarization for GPS system.

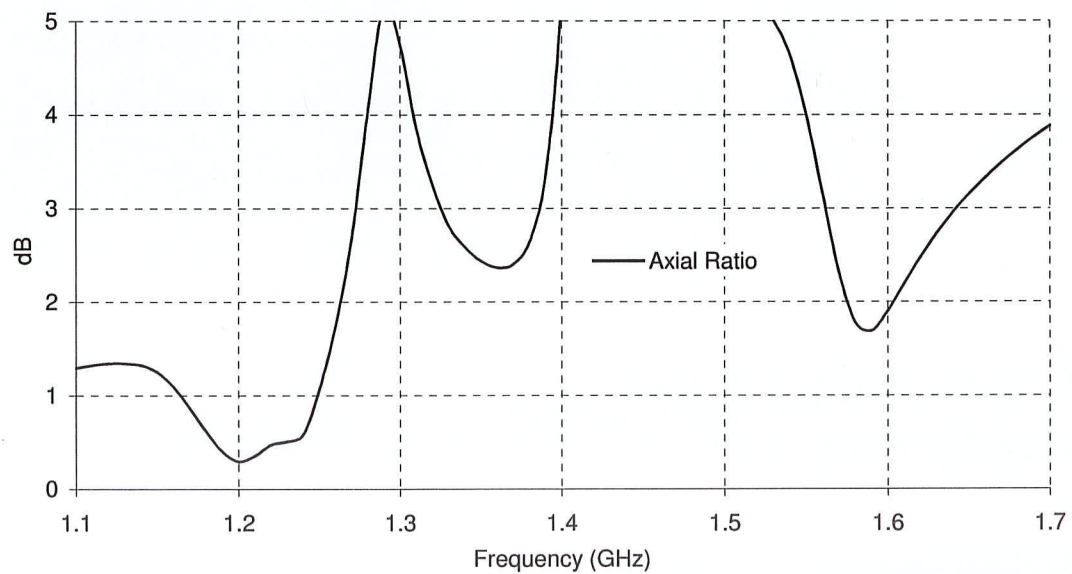


Fig. 4.9: Axial ratio of the multiple square ring antenna with orthogonal capacitive feeding. The antenna configuration is shown in Fig. 4.8 and antenna parameters are mentioned in Table 4.3.

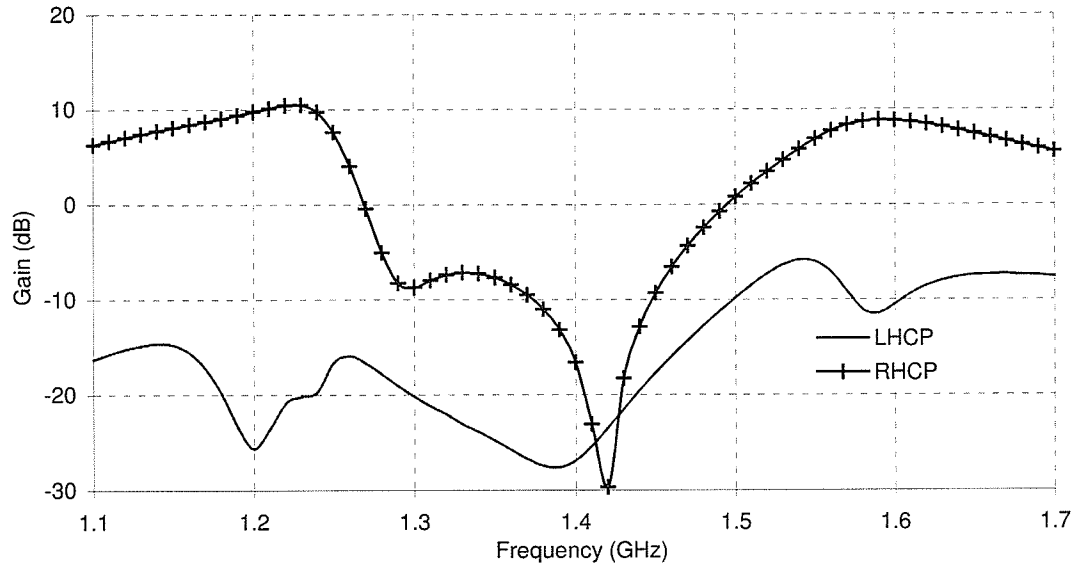


Fig. 4.10: CP gains of the multiple square ring antenna with orthogonal capacitive feeding. The antenna configuration is shown in Fig. 4.8 and antenna parameters are mentioned in Table 4.3.

CP gain patterns of this antenna, at three GPS frequencies, are shown in Figs. 4.11 to 4.13. It is stated that a minimum of -3.5 dBic gain is required for a large coverage of the solid angle for GPS antennas [66]. As demonstrated in Fig. 4.11, the peak RHCP gain of the antenna at 1176 MHz is 8.9 dBic, and RHCP gain stays above -3.5 dBic for elevation angle from -70° to 80° in both principal planes. For the L2 band, i.e. 1227 MHz, the peak boresight gain is 10.5 dBic, with upper hemisphere coverage from -70° to 80° , Fig. 4.12. For higher frequency band, L1, the solid angular coverage is from -62° to 72° . However, the cross-polar level is much higher at this frequency, approximately -5 dBic or less, compared to those in two other frequencies. Peak RHCP gain in this case is 8.57 dBic, as shown in Fig. 4.13.

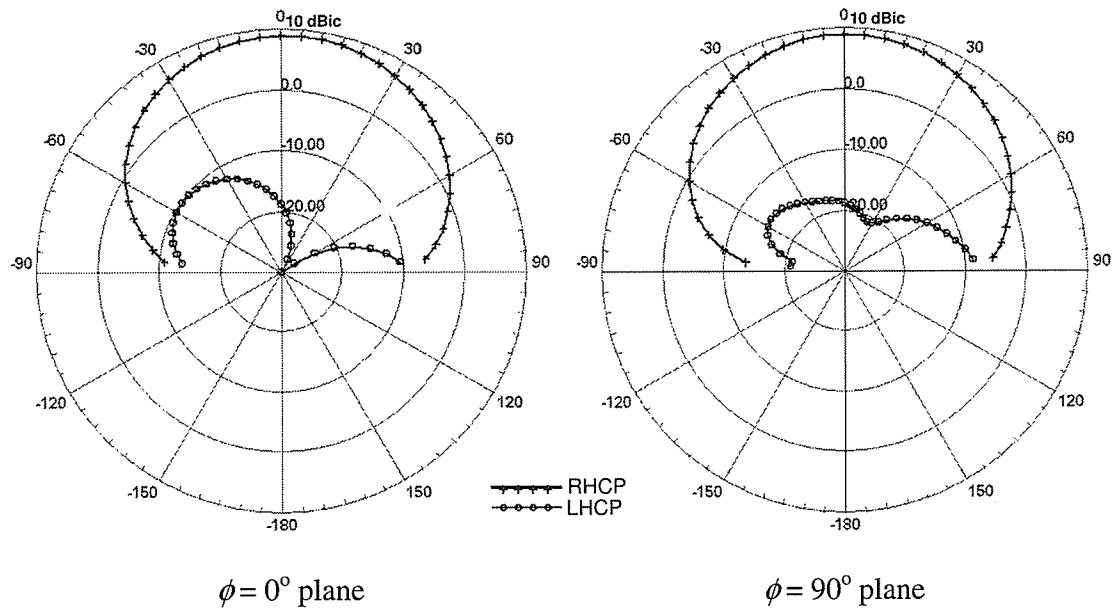


Fig. 4.11: CP gains of the multiple square ring antenna with orthogonal capacitive feeding at 1176 MHz in two principal planes. The antenna configuration is shown in Fig. 4.8 and antenna parameters are mentioned in Table 4.3.

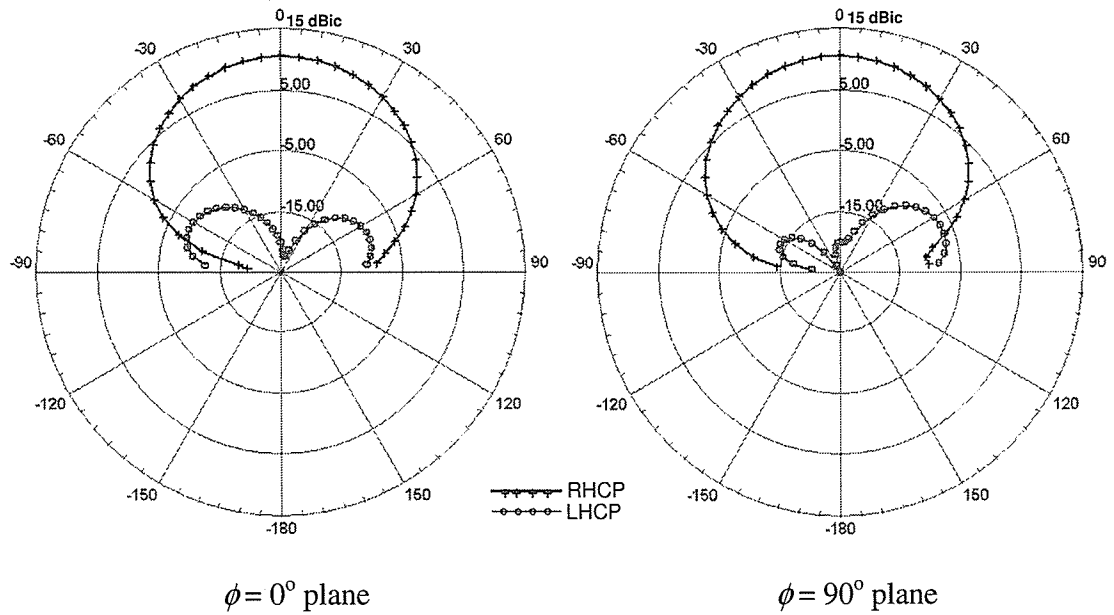


Fig. 4.12: CP gains of the multiple square ring antenna with orthogonal capacitive feeding at 1227 MHz in two principal planes. The antenna configuration is shown in Fig. 4.8 and antenna parameters are mentioned in Table 4.3.

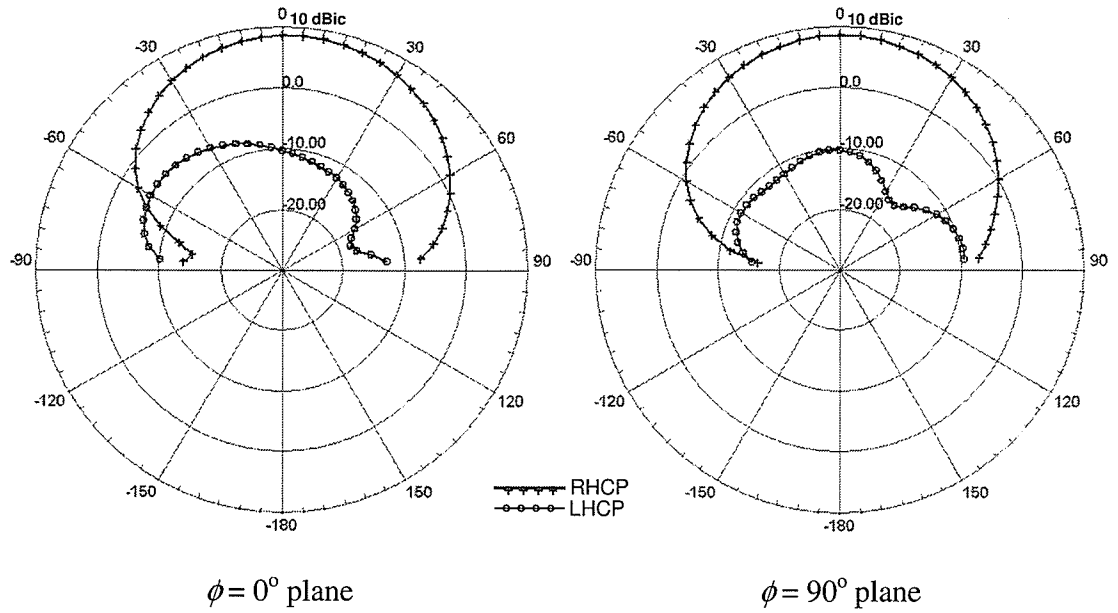


Fig. 4.13: CP gains of the multiple square ring antenna with orthogonal capacitive feeding at 1575 MHz in two principal planes. The antenna configuration is shown in Fig. 4.8 and antenna parameters are mentioned in Table 4.3.

4.5 Conclusion

Stacked square ring microstrip antenna opens up an opportunity to accommodate more resonators inside the rings, however with a challenge of exciting all three rings. A general method was proposed to design an antenna using three rings to operate at three frequencies. Two stacked rings were chosen such that if one was excited, it could electromagnetically excite the other. A third ring was accommodated inside the parasitic ring, which was larger in size compared to the bottom one, since it was on a foam substrate. To overcome the problem of feeding, a capacitive feeding was proposed, which allowed using narrow-width rings. It did not occupy extra space as well, since the inside

capacitive feeding was used for the inner third ring. The outside capacitive feeding was chosen for the bottom ring, which did not extend beyond the parasitic ring on top. The design was confirmed using two commercially available software: Ansoft Desinger (MoM-based) and Ansoft HFSS (FEM-based). A practical application of such an antenna was shown for the case of tri-band GPS. Dimensions of the three rings were selected such that the antenna covered three GPS frequency bands of L1, L2 and L5. The antenna had an overall height of 15.6 mm, and a size of 0.3λ at L5 frequency, on low-permittivity substrate materials.

CHAPTER FIVE

Loaded Square Ring Antenna

5.1 Introduction

In chapters three and four, we presented wideband and multi-frequency square ring antennas. To obtain multi-frequency operation using square rings, three rings were arranged in two stacked substrate layers and fed capacitively. For each ring, the TM_{11} mode was excited, and the corresponding frequencies were controlled to obtain multi-frequency or wideband operation. The geometry was a complex one, and it had limitations in achieving a certain frequency of operation due to the problem of accommodating two rings on the top layer.

Investigations in this chapter are aimed at loaded microstrip square ring antenna to show that multi-frequency operation can be achieved with a single layer square ring antenna by loading it. The TM_{11} mode of the square ring antenna is designated as the ‘unloaded mode’. It has been mentioned earlier that it is difficult to match the input impedance at the resonance frequency due to the unloaded mode. Attempts have been made to improve the impedance matching and bandwidth by loading it with a stub, notch, gap, shorting post etc. However, the loading increases the cross-polarization level. An interesting phenomenon has been observed when the square ring antenna is loaded with a narrow gap. Several resonances become excited along with the unloaded mode, one being

at much lower frequency than the unloaded mode. The multi-frequency capability and polarization of this loaded square ring antenna is discussed in this chapter. Some other miniaturized gap-loaded square ring antennas are also discussed here with the emphasis on the antenna performance.

5.2 Gap loaded square ring antenna

The discussion will start again from a regular square ring antenna, shown in Fig. 5.1(a), and step-by-step the effects of gap loading on this antenna will be shown. In this case, the square ring is on a dielectric material with permittivity (ϵ_r) of 2.5, thickness (h) of 1.57 mm, and loss tangent ($\tan\delta$) of 0.0019. The antenna parameters are: $L_1 = 35$ mm, $L_2 = 17.5$ mm, $W = 8.75$ mm. The probe is centered on one arm along the y-axis. For this antenna, the simulated return loss plot is shown in Fig. 5.1(b), obtained from Ansoft Designer. Low S_{11} value at unloaded mode frequency $f_u = 2.082$ GHz indicates a poor impedance matching. The antenna is x -polarized at this frequency, as can be noticed by the current distribution of the antenna in Fig. 5.1(c). At this frequency, its peak accepted gain is 5.5 dBi in both principal planes, as shown in Fig. 5.2. Moreover, the cross-polar level is very low, nearly -80 dBi along boresight. These results are summarized in Table 5.1. As mentioned previously, originally square ring antennas were loaded to improve the impedance match at f_u . Next, it will be shown that by loading, two more resonances are excited close to the unloaded mode frequency of the square ring.

Table 5.1: Polarization and accepted gain of unloaded square ring antenna. The antenna parameters are provided in the caption of Fig. 5.1

Frequency	Polarization	Peak accepted gain (dBi)			
		$\Phi = 0^\circ$		$\Phi = 90^\circ$	
		E_θ	E_ϕ	E_θ	E_ϕ
$f_u = 2.082$	x	5.5 (at $\theta = 0^\circ$)	-80 (at $\theta = 0^\circ$)	-24 (at $\theta = \pm 75^\circ$)	5.5 (at $\theta = 0^\circ$)

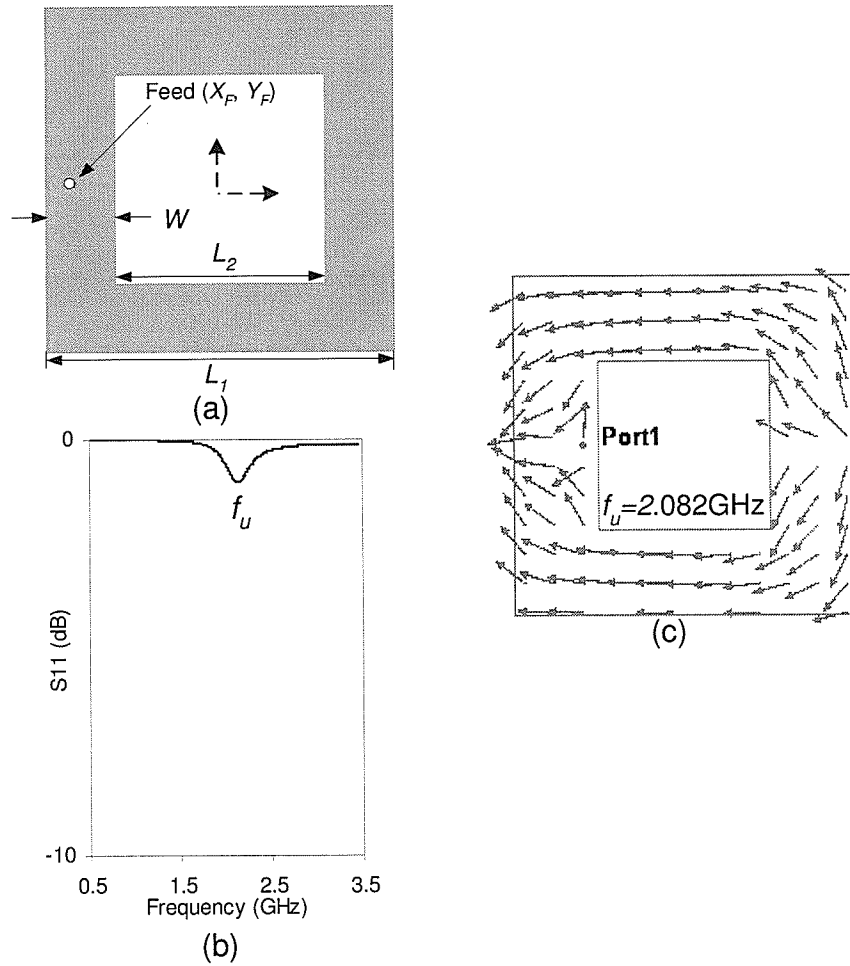


Fig. 5.1: (a) Geometry of the square ring antenna on an infinite ground plane, and its (b) return loss plot and (c) current distribution. The antenna parameters are: $L_1 = 35$ mm, $L_2 = 17.5$ mm, $W = 8.75$ mm. Substrate parameters: $\epsilon_r = 2.5$, $h = 1.57$ mm, and $\tan \delta = 0.0019$. Probe position: $X_F = -10.5$ mm, $Y_F = 0$ mm.

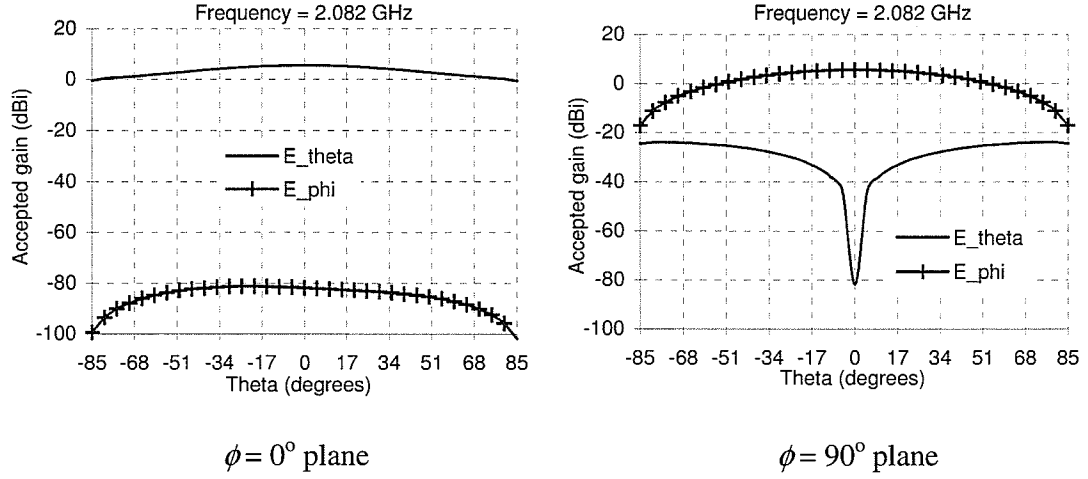


Fig. 5.2: Radiation patterns of the square ring antenna at $f_u = 2.082$ GHz. The antenna parameters are given in the caption of Fig. 5.1.

5.2.1 Vertical gap loading

When a vertical gap is introduced symmetrically on the upper arm of the square ring antenna with an off-center feed point on the arm along the y -axis, Fig. 5.3(a), the impedance matching at f_u , is improved, as can be noticed in Fig. 5.2(b). However, two more resonances based on minimum S_{11} value, f_{L1} and f_{L2} appear, namely loaded mode frequencies, with

$$f_{L1} < f_u < f_{L2} \quad (5.1)$$

and these three frequencies are almost equally spaced in the spectrum.

If we closely observe the current distribution plot for f_{L1} in Fig. 5.3(c), we can see that the square ring is working as a folded dipole, and has a current flowing along the

strip, which excites the dipole mode, and therefore, causes f_{L1} . f_u is due to the square ring, and f_{L2} is excited due to the loading. More design equations, and the relationship among these frequencies are discussed in a later section. Note that with a symmetric location of the feed along the y -axis and with a symmetric vertical gap loading on the arm along the x -axis, these loaded modes cannot be obtained. Interestingly, if we observe the current distribution at f_u in Fig. 5.3(d), one can notice that the polarization of the antenna at f_u has changed to y -polarization with respect to x -polarization at f_u , for the unloaded case. At f_{L2} , the antenna is x -polarized, same as f_{L1} , as E_θ is the co-polar component in the $\phi = 0^\circ$ plane, Fig. 5.3(e). However, the S_{11} value is poor at f_{L1} .

The gain patterns are plotted in Figs. 5.4 to 5.6 for all three frequencies. Note that the peak accepted gain at f_{L1} is -6.3 dBi, as shown in Fig. 5.4. We will discuss more about this gain drop later. The cross-polar level at f_u is slightly higher compared to the unloaded case, as can be noticed in Fig. 5.5. For both f_{L1} and f_{L2} , in the $\phi = 0^\circ$ plane, the cross-polar level is much higher, particularly around $\pm 45^\circ$, Figs. 5.4 and 5.6. However, the boresight cross-polar level is still low in both planes, at all three frequencies. This discussion is summarized in Table 5.2. These simulation results are also obtained from Ansoft Designer, using an infinite ground plane.

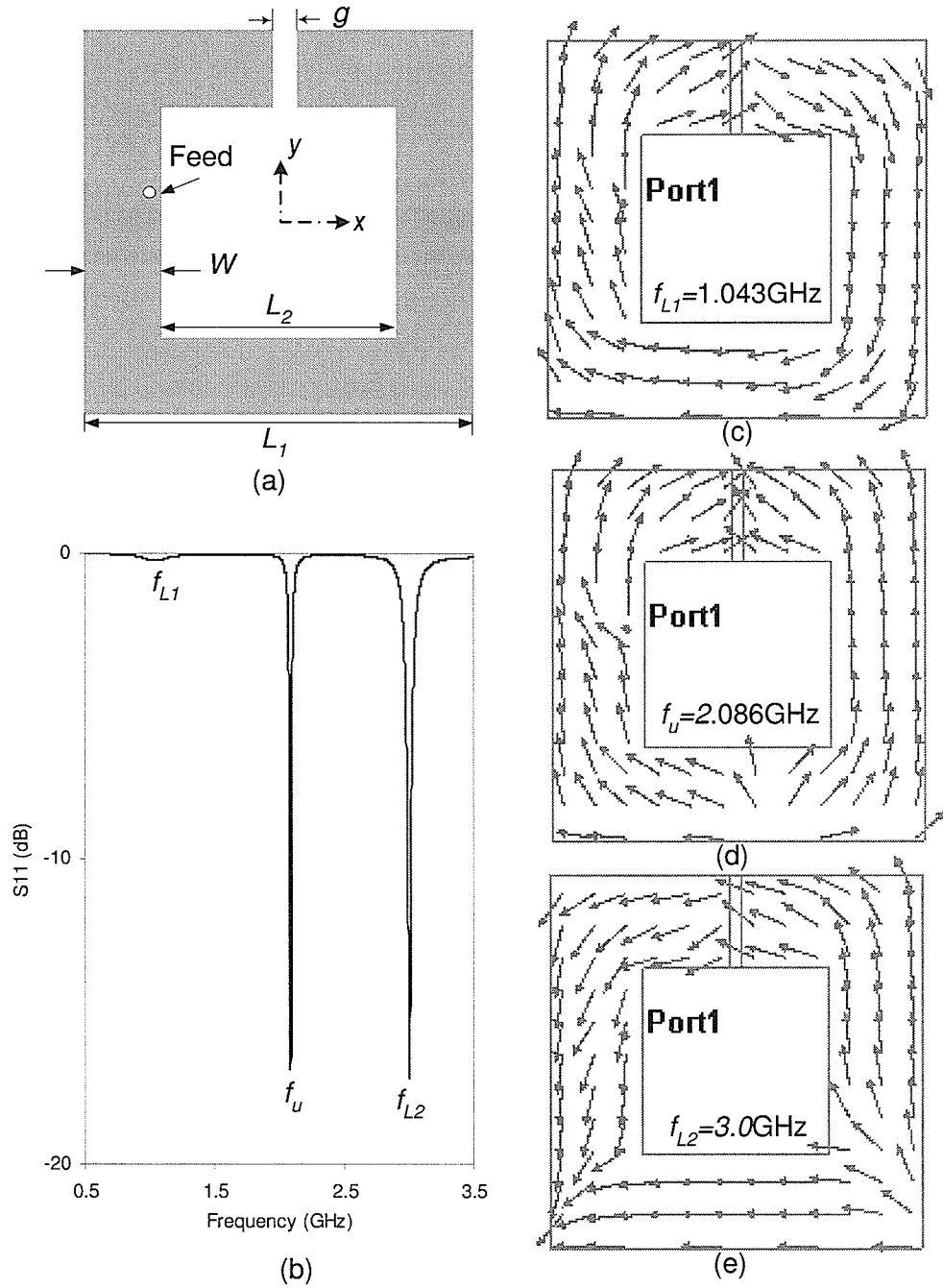


Fig. 5.3: (a) Geometry of the loaded square ring antenna on an infinite ground plane with a vertical gap, (b) its return loss plot, and current distributions of the antenna at (c), f_{L1} , (d) f_u , (e) f_{L2} . The antenna parameters are: $L_1 = 35$ mm, $L_2 = 17.5$ mm, $W = 8.75$ mm. Gap size, $g = 1$ mm. Substrate parameters: $\epsilon_r = 2.5$, $h = 1.57$ mm, and $\tan\delta = 0.0019$. Probe position: $X_F = -10.5$ mm, $Y_F = 2.5$ mm.

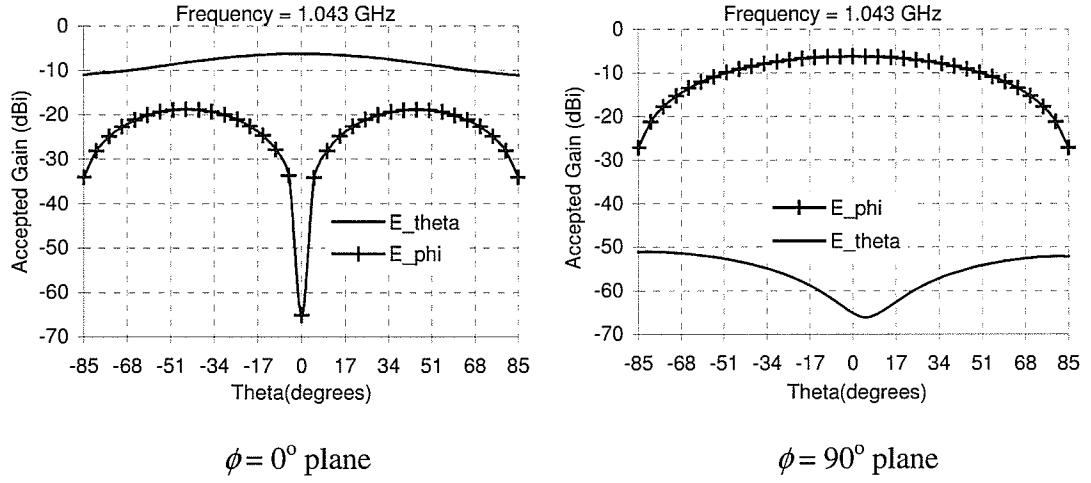


Fig. 5.4: Radiation patterns of the loaded square ring antenna with a vertical gap at $f_{LI} = 1.043$ GHz. The antenna parameters are given in the caption of Fig. 5.3.

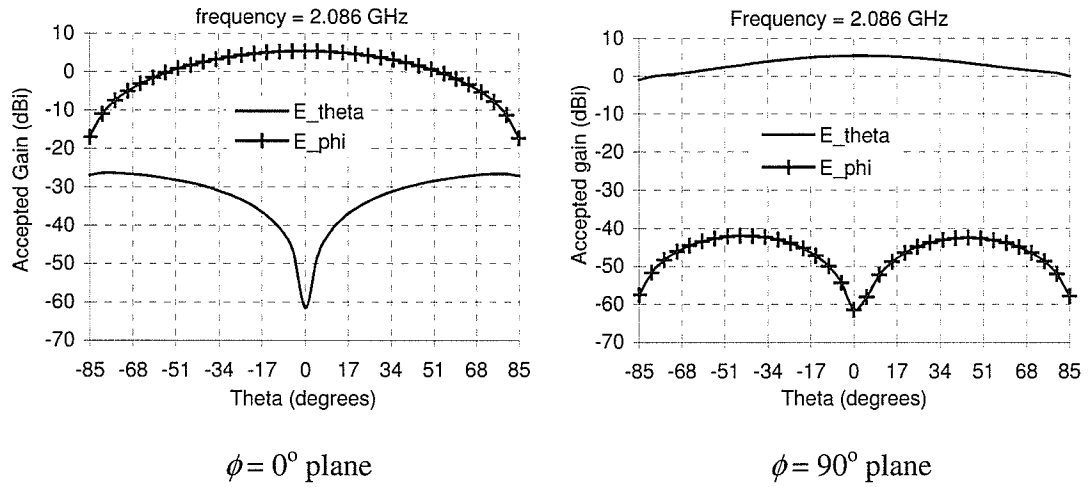


Fig. 5.5: Radiation patterns of the loaded square ring antenna with a vertical gap at $f_u = 2.086$ GHz. The antenna parameters are given in the caption of Fig. 5.3.

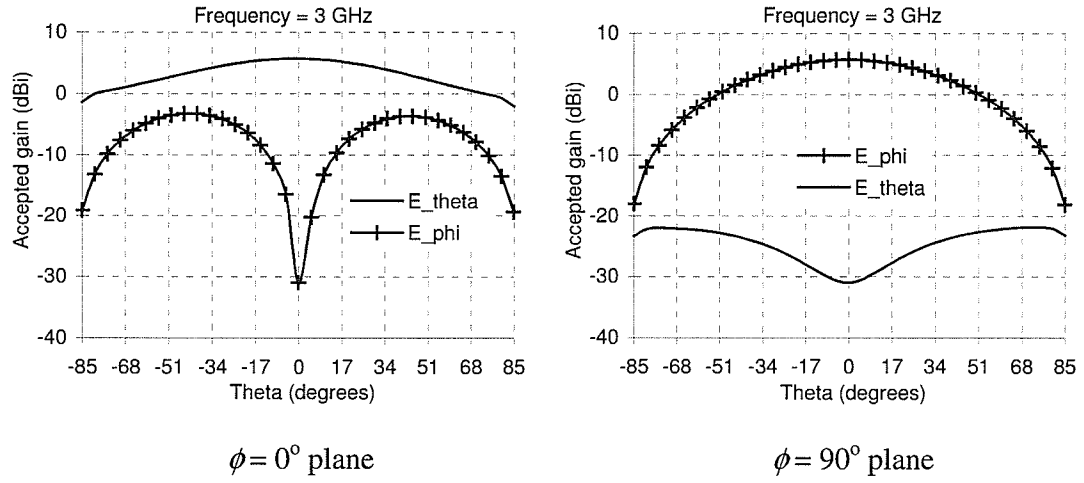


Fig. 5.6: Radiation patterns of the loaded square ring antenna with a vertical gap at $f_{L2} = 3.0$ GHz. The antenna parameters are given in the caption of Fig. 5.3.

Table 5.2: Polarization and accepted gain of the square ring antenna loaded with a vertical gap. The antenna parameters are provided in the caption of Fig. 5.3

Frequency (GHz)	Polarization	Peak Accepted Gain (dBi)			
		$\Phi = 0^\circ$		$\Phi = 90^\circ$	
		E_θ	E_ϕ	E_θ	E_ϕ
$f_{L1}=1.043$	x	-6.3 (at $\theta = 0^\circ$)	-18.6 (at $\theta = \pm 45^\circ$)	-51 (at $\theta = \pm 85^\circ$)	-6.3 (at $\theta = 0^\circ$)
$f_u=2.086$	y	-26 (at $\theta = \pm 80^\circ$)	5.4 (at $\theta = 0^\circ$)	5.4 (at $\theta = 0^\circ$)	-42 (at $\theta = \pm 45^\circ$)
$f_{L2}=3.0$	x	5.7 (at $\theta = 0^\circ$)	-3.3 (at $\theta = \pm 45^\circ$)	-22 (at $\theta = \pm 75^\circ$)	5.7 (at $\theta = 0^\circ$)

5.2.2 Horizontal gap loading

Instead of the vertical gap, we can load the square ring with a horizontal gap too, and still notice three resonances. In this case, the loading is located symmetrically on the arm along the y -axis in the form of a gap, keeping the feed point off-centered on the other arm again along the y -axis, as shown in Fig. 5.7(a). A better impedance matching can be achieved for f_{L1} and f_{L2} , with poor S_{11} value for f_u , Fig. 5.7(b). Note that the antenna polarization for all three frequencies rotates 90° with reference to the polarizations of the vertical gap-loaded case (x - to y -polarization or y - to x -polarization), as can be seen in Figs. 5.7(c) to 5.7(e).

The peak accepted gain for the lowest frequency, in this case, is about -6.3 dBi, as can be seen in Fig. 5.8. The gain patterns for f_u and f_{L2} are also shown in Figs. 5.9 and 5.10. They have similar performances like the case with vertical gap loading, except that the polarizations have been shifted by 90° . The results discussed so far are summarized in Table 5.3, which are obtained from Ansoft Designer, considering an infinite ground plane.

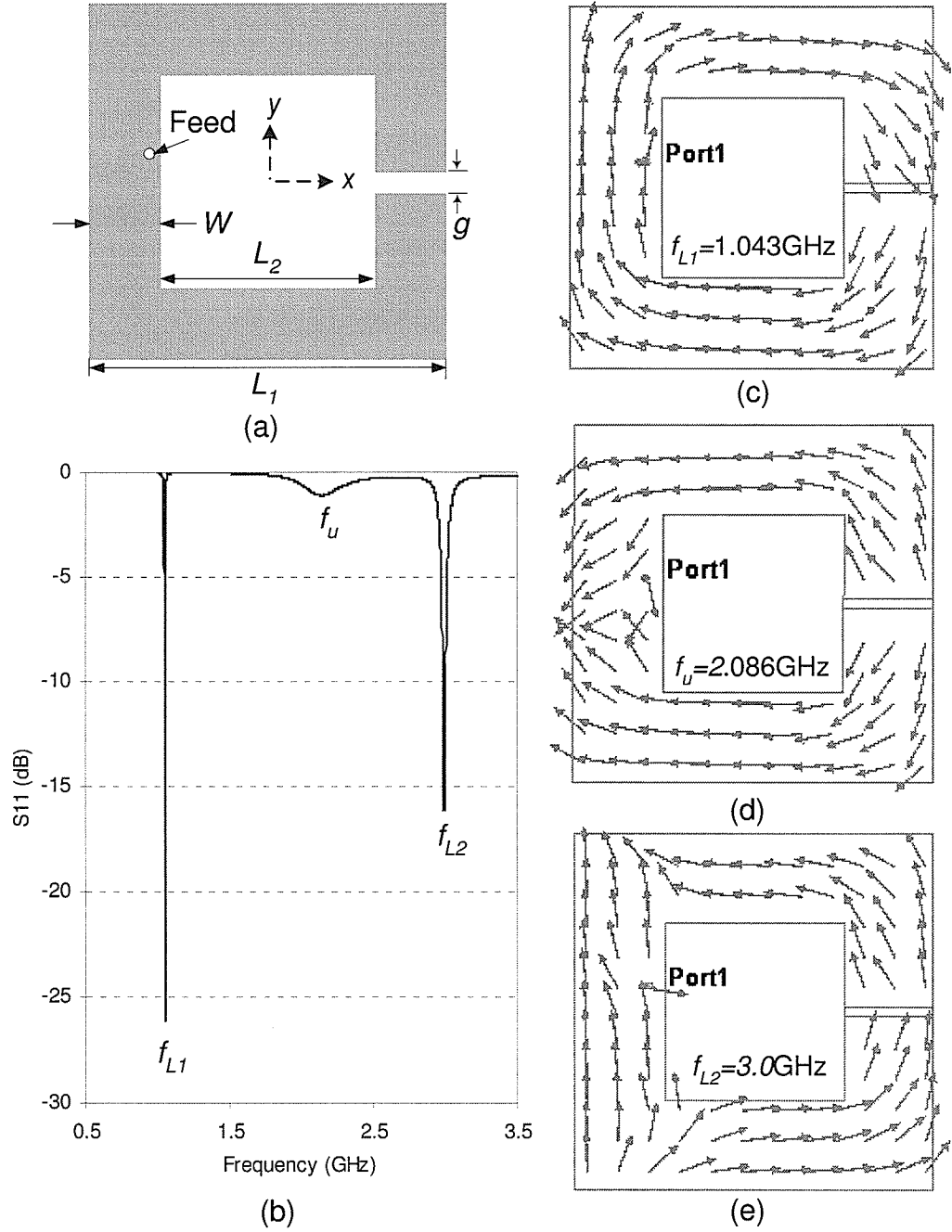


Fig. 5.7: (a) Geometry of the loaded square ring antenna on an infinite ground plane with a horizontal gap, current distributions of the antenna at (b), f_{L1} , (d) f_u , (e) f_{L2} , and (e) its return loss plot. The antenna parameters are: $L_1 = 35$ mm, $L_2 = 17.5$ mm, $W = 8.75$ mm. Gap size, $g = 1$ mm. Substrate parameters: $\epsilon_r = 2.5$, $h = 1.57$ mm, and $\tan\delta = 0.0019$. Probe position: $X_F = -10.5$ mm, $Y_F = 2.5$ mm.

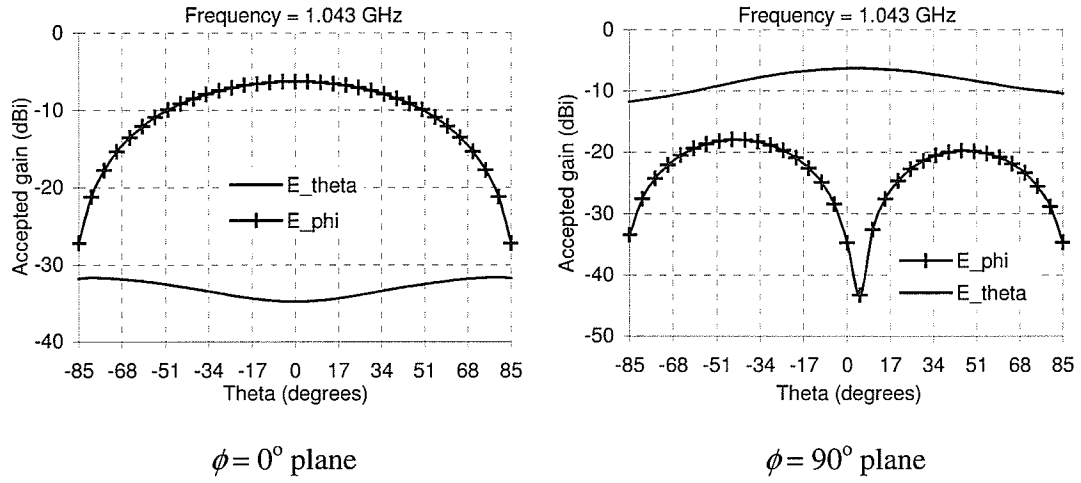


Fig. 5.8: Radiation patterns of the loaded square ring antenna with a horizontal gap at f_{LI} = 1.043 GHz. The antenna parameters are given in the caption of Fig. 5.7.

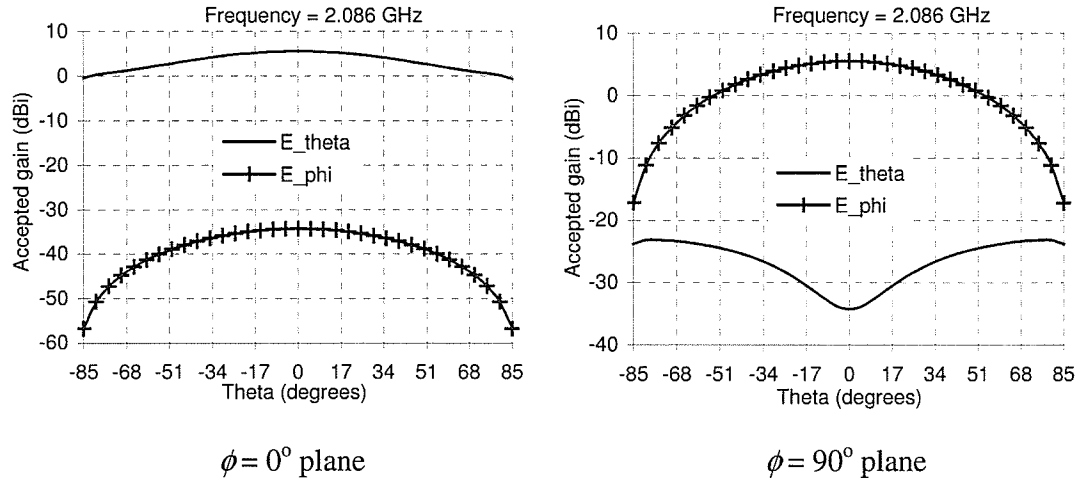


Fig. 5.9: Radiation patterns of the loaded square ring antenna with a horizontal gap at f_u = 2.086 GHz. The antenna parameters are given in the caption of Fig. 5.7.

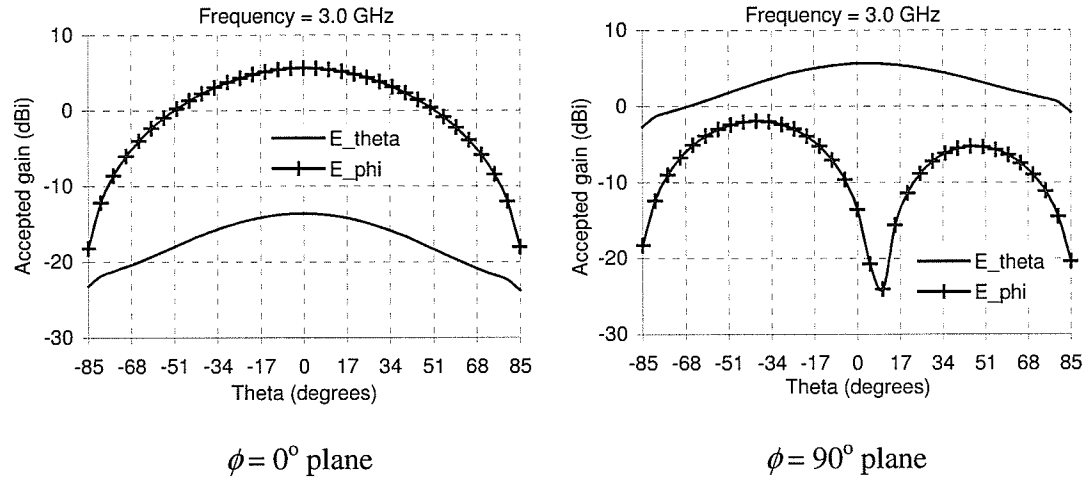


Fig. 5.10: Radiation patterns of the loaded square ring antenna with a horizontal gap at $f_{L2} = 3.0$ GHz. The antenna parameters are given in the caption of Fig. 5.7.

Table 5.3: Polarization and accepted gain of the square ring antenna loaded with a horizontal gap. The antenna parameters are provided in the caption of Fig. 5.7

Frequency (GHz)	Polarization	Peak accepted gain (dBi)			
		$\Phi = 0^\circ$		$\Phi = 90^\circ$	
		E_θ	E_ϕ	E_θ	E_ϕ
$f_{L1}=1.043$	y	-32 (at $\theta = 80^\circ$)	-6.3 (at $\theta = 0^\circ$)	-6.3 (at $\theta = 0^\circ$)	-18 (at $\theta = -45^\circ$)
$f_u=2.086$	x	5.5 (at $\theta = 0^\circ$)	-34 (at $\theta = 0^\circ$)	-23 (at $\theta = \pm 80^\circ$)	5.5 (at $\theta = 0^\circ$)
$f_{L2}=3.0$	y	-13.6 (at $\theta = 0^\circ$)	5.6 (at $\theta = 0^\circ$)	5.6 (at $\theta = 0^\circ$)	-2 (at $\theta = -40^\circ$)

5.3 Parametric study of the loaded square ring antenna

In order to better understand the relationship among the first three resonances of the loaded square ring antenna: f_{L1} , f_u , and f_{L2} , a detail parametric study is conducted using Ansoft Designer. There are several important parameters of the open square ring antenna, which affects its resonance frequencies. Detailed study about the first unloaded mode frequency, f_{L1} , has been discussed in [70, 71]. Here, the effects of varying the probe position, substrate parameters, gap length (g), and width of the ring (W) are discussed. Only one parameter is varied at a time, while keeping the rest of the parameters fixed, as shown in the caption of Fig. 5.11. An infinite ground plane is selected for the simulation.

5.3.1 Effect of probe position (X_F , Y_F)

It is mentioned earlier that, for the open square ring antenna, if the probe is placed symmetrically in one arm, while the gap is also symmetric on another arm, the loaded mode resonance frequencies cannot be excited. However, a slight asymmetric position of the probe excites two modes. For the case of horizontal gap loaded square ring antenna, by slightly changing the position of the probe along the y -axis, the reactance of the antenna can be changed. For the case of f_{L1} , this variation is demonstrated on the Smith chart of Fig. 5.11(a). However, as the feed point approaches to the corner of the ring, severe impedance mismatch is observed.

The variation in the input impedance due to moving of the feed probe point, along the x -axis is presented in Fig. 5.11(b). Note that the variation in the reactance is smaller for a large change in the X_F value, compared to the previous case. Similar effects are observed for f_u , and f_{L2} as well, and not shown here. Thus, by adjusting the probe location, good impedance matching can be found for the frequencies of the loaded and unloaded mode.

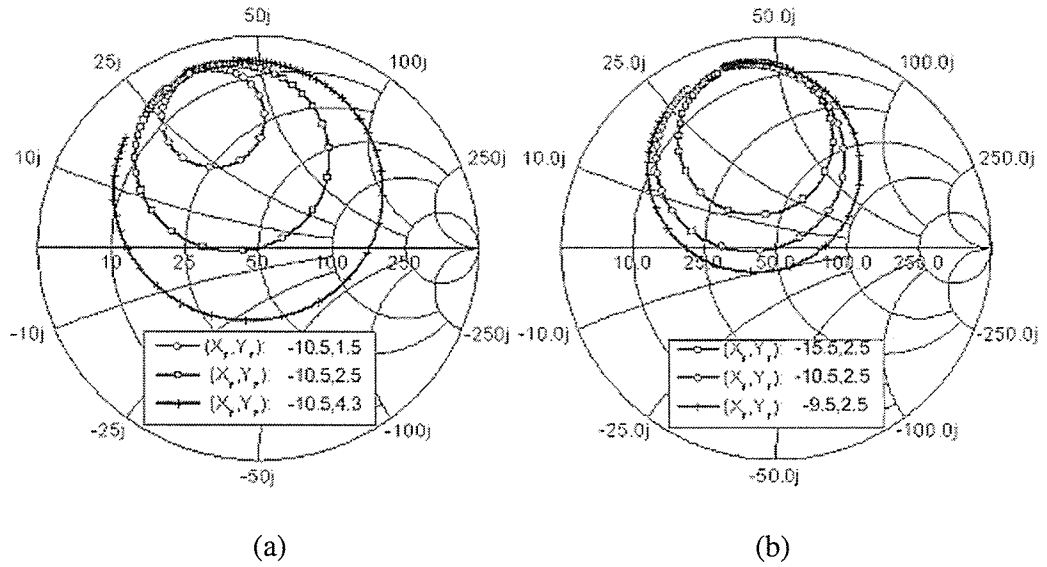


Fig. 5.11: The effects of different probe locations on the impedance of the loaded mode frequency f_{L1} of the square ring antenna in Fig. 5.7(a): (a) varying Y_F with $X_F = -10.5$ mm. (b) varying X_F with $Y_F = 2.5$ mm. The antenna parameters are: $L_1 = 35$ mm, $L_2 = 17.5$ mm, $W = 8.75$ mm. Gap size, $g = 1$ mm. Substrate parameters: $\epsilon_r = 2.5$, $h = 1.57$ mm, and $\tan \delta = 0.0019$.

5.3.2 Effect of substrate parameters

Substrate permittivity (ϵ_r)

Keeping all the parameters, mentioned in Fig. 5.11, fixed, the substrate permittivity, ϵ_r , is varied, and the effects on the return loss plot are shown in Fig. 5.12. When the substrate permittivity is increased from 2.5 to 4.4, loaded and unloaded mode frequencies shifted from the higher to lower frequencies. The amount of shifting is larger for higher frequencies, probably due to higher fringing effect.

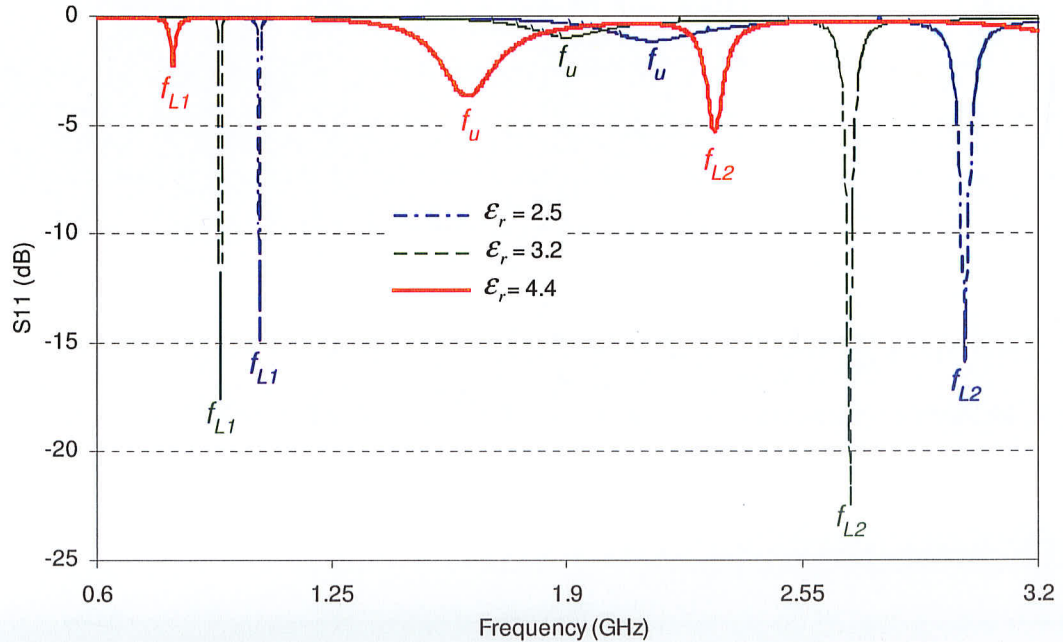


Fig. 5.12: The effects of varying ϵ_r on the frequency of the loaded square ring antenna in Fig. 5.7(a). The antenna parameters are the same as in the caption of Fig. 5.11.

Substrate thickness (h)

Next, the substrate thickness is varied for the case with $\epsilon_r=2.5$, and its effect on the return loss is shown in Fig. 5.13. Both f_{L1} and f_u move to the higher frequency. The reason behind this shifting, especially for the case of f_u , can be explained with the help of current distribution plot in Fig. 5.14. For larger thickness, the higher concentration of current can be noticed at the inner edge, which essentially reduces the average circumferential length of the square ring. However, f_{L2} moves to the lower frequency for an increase in the substrate thickness. In fact, as the thickness is increased, both f_u and f_{L2} come closer, and for the case of $h=10$ mm, they merge together.

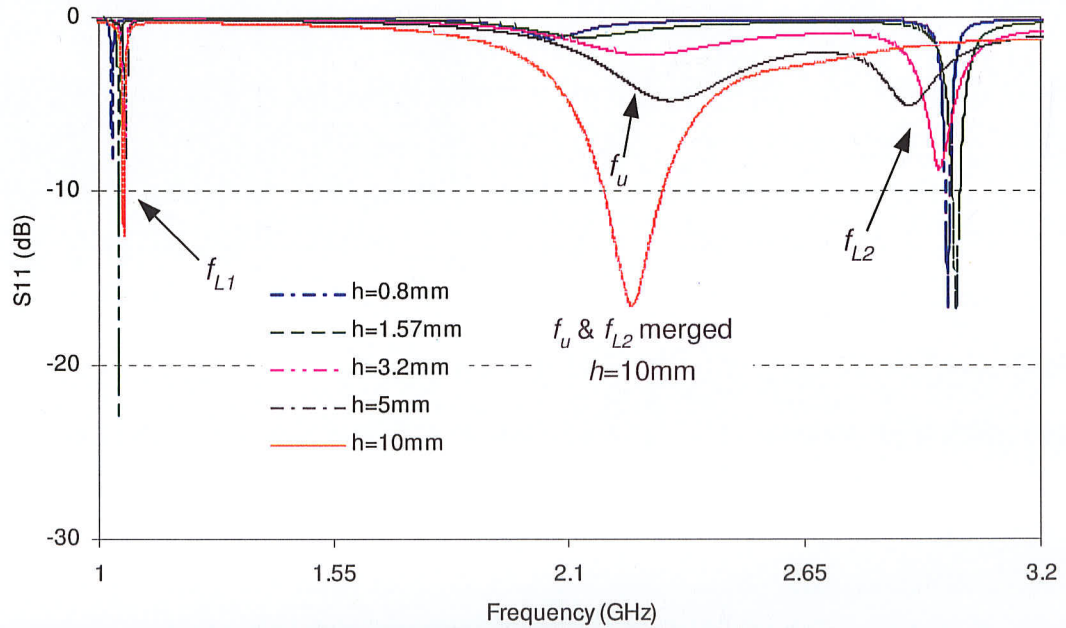


Fig. 5.13: The effects of varying h on the loaded and unloaded mode frequencies of the loaded square ring antenna in Fig. 5.7(a). The antenna parameters are the same as in the caption of Fig. 5.11.

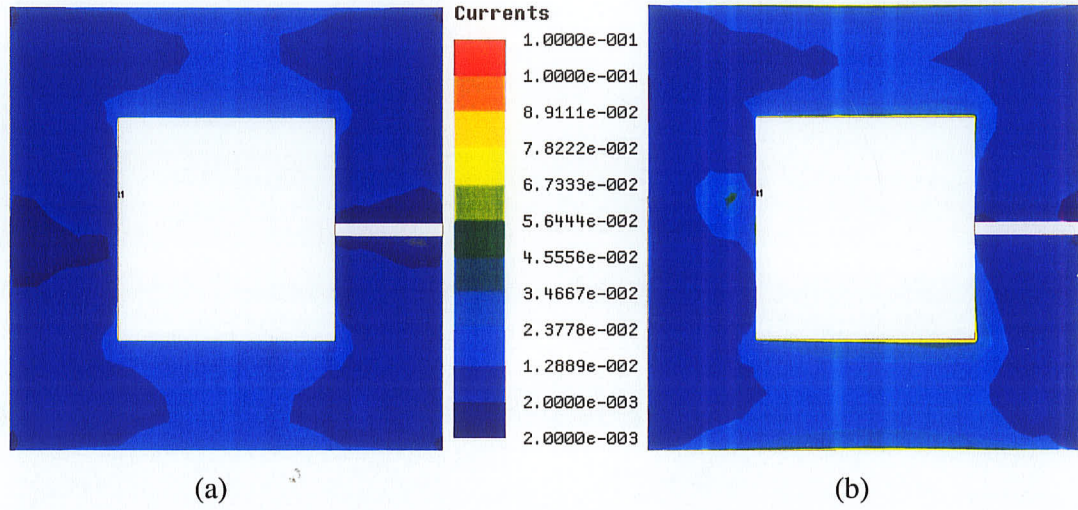


Fig. 5.14: Current distributions, at f_{L2} , of the loaded square ring antenna in Fig. 5.7(a) for (a) $h = 0.8$ mm and (b) $h = 10$ mm. The antenna parameters are the same as in the caption of Fig. 5.11.

5.3.3 Effect of ring width (W)

The effect of varying the ring width (W) on the return loss of the antenna in Fig. 5.7(a), keeping the rest of the parameters fixed, is shown in Fig. 5.15. From Table 5.4, it is evident that, when the slot size decreases, the width increases, and the average circumferential length of the ring length decreases. As a result, the effective current flow path decreases, which in turn increases the resonance frequencies due to the loaded and unloaded mode. The shifting in frequency is larger for the second unloaded mode frequency, f_{L2} , compared to f_{L1} and f_u . The detail about f_{L1} is provided in Table 5.4, showing it's shifting toward higher frequency, and narrow impedance bandwidth.

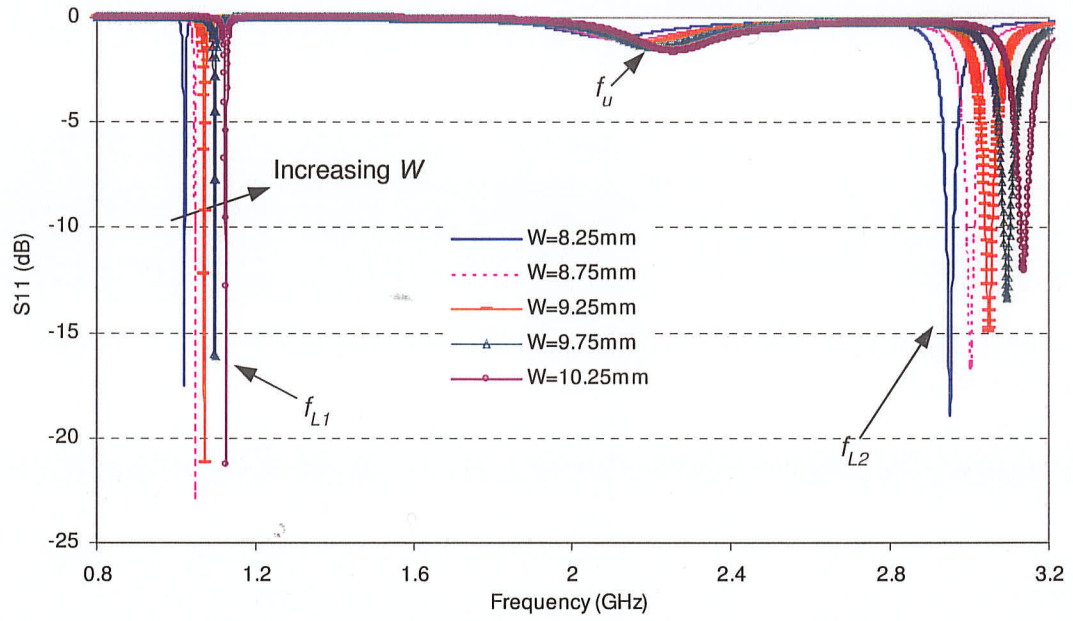


Fig. 5.15: The effects of varying width (W) on the return loss of the loaded square ring antenna in Fig. 5.7(a). The antenna parameters are: $L_1 = 35$ mm, Gap size, $g = 1$ mm, substrate parameters: $\epsilon_r = 2.5$, $h = 1.57$ mm, and $\tan\delta = 0.0019$. Probe location: $X_F = 10.5$ mm, $Y_F = 2.5$ mm.

Table 5.4: The effect of varying ring width (W) on f_{L1} of the square ring antenna in Fig. 5.7(a). The antenna parameters are mentioned in the caption of Fig. 5.15

Slot Size L_2 (mm ²)	Ring Width W (mm)	1 st Unloaded Mode Frequency f_{L1} (GHz)	-10dB RL BW (MHz)
16.5	8.25	1.021	2.1
17.5	8.75	1.043	2.1
16.5	9.25	1.0708	2.2
15.5	9.75	1.0964	2.2
14.5	10.25	1.1248	2.4

5.3.4 Effect of gap length (g)

Since, loading of the square ring antenna, in the form of a gap, gives several resonances, the gap length (g) is an important parameter of this antenna. In fact, an increase in g lowers the average circumferential length of the square ring. Therefore, the loaded mode resonances move to the higher frequencies, as shown in Fig. 5.16. However the shifting of unloaded mode frequency, f_u , is insignificant. Like the previous case, shifting in frequency is larger for the second unloaded mode frequency, f_{L2} , compared to f_{L1} .

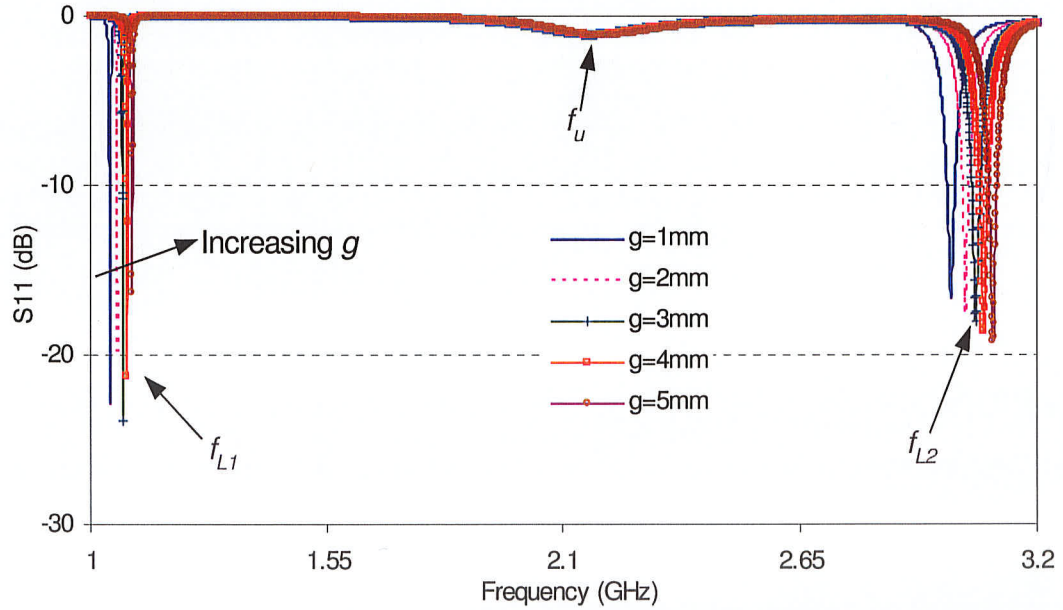


Fig. 5.16: The effects of varying g on the return loss of the loaded square ring antenna in Fig. 5.7(a), with $L_2 = 17.5$ mm. Other antenna parameters are the same as in the caption of Fig. 5.15.

5.4 Design guideline

By carefully studying the parametric data, and the discussion about the loading in Section 5.2, we can establish a relationship among the loaded and unloaded mode frequencies, and present the design equations based on the ring parameters. The unloaded mode frequency, f_u , is due to the TM_{11} mode of the square ring, and its corresponding wavelength λ_u in the dielectric can be found from:

$$L_{avg,unloaded} = \lambda_u \quad (5.2)$$

where L_{avg} is the average circumferential length of the square ring, and can be calculated from the physical parameters of the ring as follows:

$$L_{avg,unloaded} = (L_2 + W) \times 4 \quad (5.3)$$

From λ_u , the unloaded mode frequency f_u can be easily calculated using the following equation:

$$f_u = \frac{c}{\lambda_u \sqrt{\epsilon_{eff}}} \quad (5.4)$$

As mentioned earlier, the current distribution plot at f_{LI} of the loaded square ring antenna in Fig. 5.3(c) indicates that the dipole mode is excited causing the resonance at f_{LI} . Based on the parametric study, it is clear that we can relate f_{LI} and f_u by the following equation:

$$f_{LI} = 0.5 f_u \quad (5.5)$$

Again, from different return loss plots and the parametric study in Section 5.3

$$f_{L2} \approx f_u + f_{L1} \quad (5.6)$$

The reason for the equation (5.6) being approximate is that for the case of square ring, because of the strong fringing effect on the corners, summation of f_{L1} and f_u is not exactly equal to f_{L2} . If we can have a geometry with smooth bending, such as, annular ring, and thus, have less fringing effect, we will have the following relationship among three frequencies:

$$f_{L2} = f_u + f_{L1} \quad (5.7)$$

To facilitate this claim, the return loss plot for a loaded annular ring antenna having an inner diameter of 12 mm, and outer diameter of 21 mm, on a foam substrate with thickness 0.8 mm, is presented in Fig. 5.17. Considering its average diameter be the average of its inner and outer diameters, its average circumferential length is 104 mm. Due to the loading, its three resonances occur at 1.510 GHz, 3.074 GHz and 4.509 GHz. In this case, loaded and mode frequencies follow equation (5.7).

It is to be noted that the above discussion is valid as long as a thin substrate is used for the square ring antenna. When the substrate thickness is much higher, the second unloaded mode disappears, as discussed in Section 5.3.2.

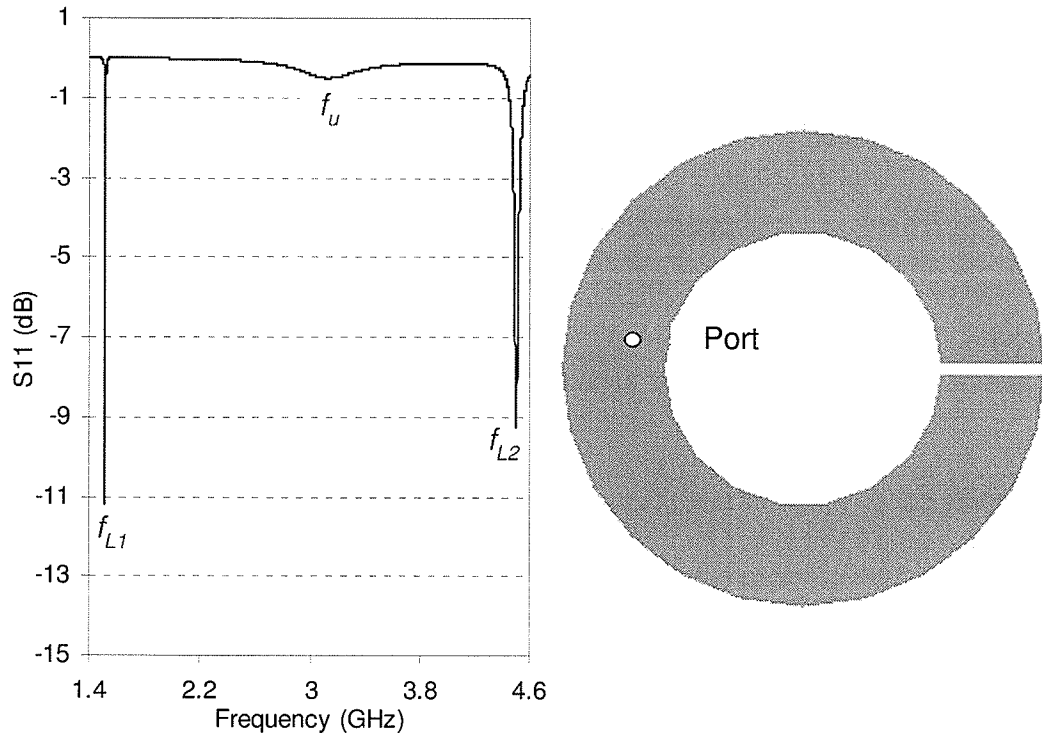


Fig. 5.17: Return loss plot of the gap-loaded annular ring antenna on an infinite ground plane, with its geometry. The antenna parameters are: inner diameter = 12 mm, outer diameter = 21 mm, probe position: $X_F = -15.5$ mm, $Y_F = 2$ mm, Foam substrate thickness = 0.8 mm.

5.5 Antenna miniaturization by loading

Since loading generates a resonance much lower than the unloaded mode frequency, the miniaturization aspect of this antenna is discussed in this section. We can compare the lowest resonance frequency (f_{L1}) of this structure with the typical square patch antenna. A 35 mm-square patch [as shown in Fig. 2.8(c)] on a substrate material, with $\epsilon_r = 2.5$, $h = 1.57$ mm, and $\tan \delta = 0.0019$, on an infinite ground plane, resonates at 2.61 GHz, as found in the simulation obtained using Ansoft Designer version 3.0. A

symmetric probe location, $X_F = -5$ mm, and $Y_F = 0$ mm, can be used for this case. When a $17.5 \text{ mm} \times 17.5 \text{ mm}$ square metal portion is removed from the center of the square patch, the 35 mm-square ring resonates at 2.086 GHz, as shown earlier in Fig. 5.1(b). The antenna is symmetrically fed by a 50- Ω SMA probe at $X_F = -10.5$ mm, $Y_F = 0$ mm in this case. The unloaded mode frequency is 80% of the resonance frequency of the conventional square patch antenna. It is necessary to mention here that the resonance frequency of the square ring antenna can be lowered if the width of the ring is made narrower. Note that in order to obtain the resonance at 2.086 GHz by a square patch antenna, the size has to be 44 mm, which indicates a reduction in antenna size of 20% for square ring. It is worth repeating here that with a symmetric probe-feed, it is not practical to match the square ring antenna with a narrow width to a 50-ohm input circuit.

When the antenna is loaded with a small gap, as presented in Fig. 5.7(a), several other resonances are excited, and the lowest resonance of the antenna is $f_{LI} = 1.043$ GHz, as shown in Fig. 5.7(b). This frequency is 50% of the resonance frequency of the unloaded case, and the reduction in antenna size is 60% compared to the conventional square patch antenna. Therefore, a much smaller antenna can be obtained by loading the square ring antenna.

Again, if we look at the gain patterns of this antenna, its peak gain is only -6.3 dBi, which conforms to the well-known limitation of the miniaturized antenna: the smaller the antenna is, the poorer the gain is [4]. Later, in this chapter, we will discuss more about such poor gain of miniaturized antennas obtained from the square ring antenna, and in the next chapter, a solution to this problem will be developed.

5.6 Experimental Study

First, the antenna miniaturization due to the loading of the square ring antenna is confirmed by experimental verification. A gap-loaded square ring antenna was fabricated and tested in the Antenna Lab at the University of Manitoba. For simulation, the infinite ground plane is considered. However, for fabrication, a ground plane of $16\text{ cm} \times 16\text{ cm}$ was used. Other antenna parameters are mentioned in Fig. 5.18. In this figure, the simulated and measured return losses are compared, which indicates a good agreement. The simulated loaded mode resonance is 1.4712 GHz , and the measured one is 1.4695 GHz . Unloaded mode frequency can be noticed in the plot as well. The slight difference in the measured resonance frequencies can be attributed to the presence of the finite ground plane in the fabricated prototype, and fabrication error in the hand-made antenna.

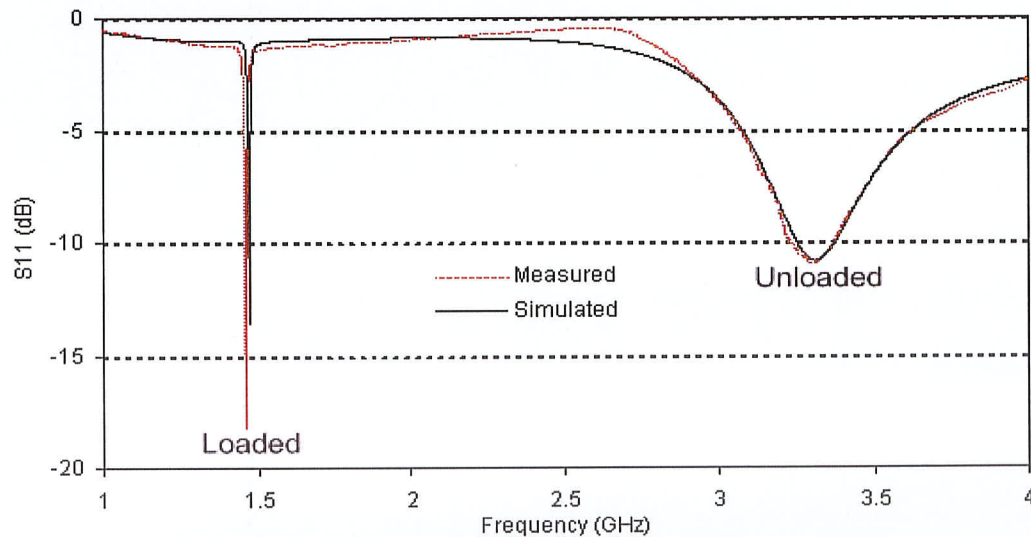


Fig. 5.18: The simulated and measured return losses of the gap-loaded square ring antenna in Fig. 5.7(a). Antenna parameters are: $L_1 = 35\text{ mm}$, $L_2 = 17\text{ mm}$, $W = 9\text{ mm}$, foam thickness, $h = 10\text{ mm}$, gap, $g = 2\text{ mm}$, probe location: $X_F = 12.5\text{ mm}$, $Y_F = 1.5\text{ mm}$.

In order to verify the gain patterns obtained from Ansoft Designer, another prototype was fabricated such that it can operate at a higher frequency, 1.64 GHz, and this is just to avoid the measurement of gain at much lower frequencies, not available in the Antenna Lab. The dimensions, for this case, are mentioned in the caption of Fig. 5.19, which has the simulated and measured return loss plot for the first loaded mode frequency. Both simulated and measured -10 dB return loss bandwidths, at this frequency, are 3.75 MHz, however, a small shifting of the resonance frequency can be noticed. Again, for simulation, an infinite ground is considered, whereas for measurement, a ground plane size of 32 cm \times 32 cm was used. Figs. 5.20 and 5.21 show the simulated and measured co- and cross-polarization levels of the antenna at the first loaded mode frequency, respectively. A good agreement is observed between simulated and measured results. It is clear that the cross-polar level is high at the loaded mode frequency, due to high orthogonal currents for unloaded mode.

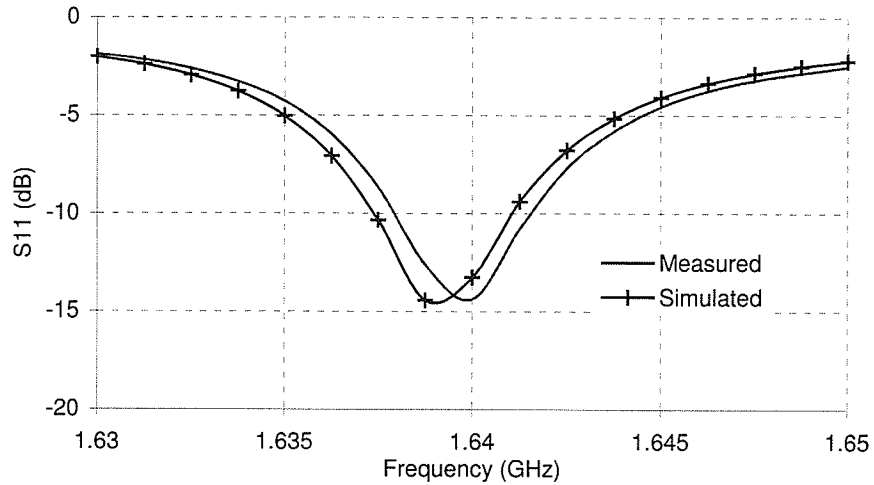
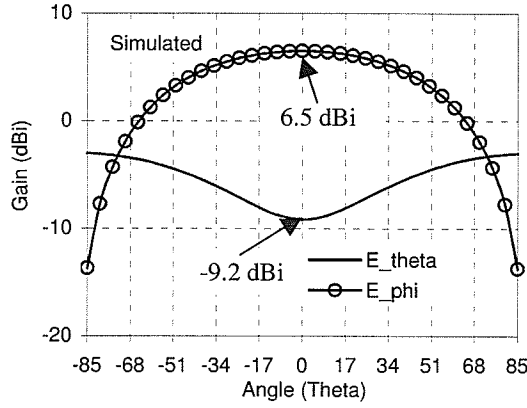
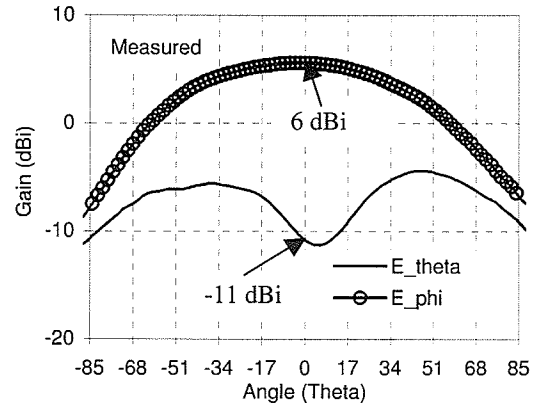


Fig. 5.19: Simulated and measured return loss plots of the square ring antenna loaded with a horizontal gap at loaded mode frequency, $f_{L1} = 1.64$ GHz. The antenna parameters are (in mm): $L_1 = 34$, $L_2 = 17.1$, $W = 8.45$, $g = 2$. Foam substrate thickness, $h = 10$.

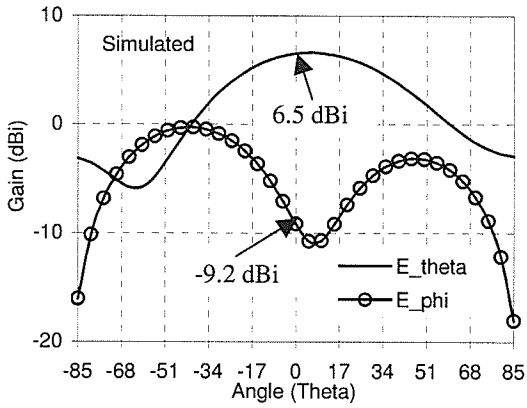


$\phi = 0^\circ$ plane
(a)

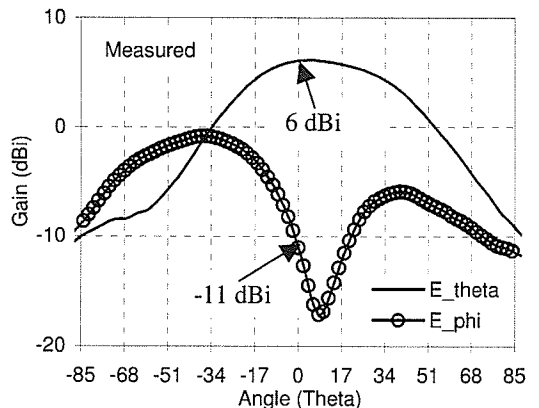


$\phi = 90^\circ$ plane
(b)

Fig. 5.20: (a) simulated and (b) measured gain patterns in the $\phi = 0^\circ$ plane of the square ring antenna loaded with a horizontal gap at loaded mode frequency, $f_{LI} = 1.64$ GHz. The antenna parameters are the same as in caption of Fig. 5.19.



$\phi = 0^\circ$ plane
(a)



$\phi = 90^\circ$ plane
(b)

Fig. 5.21: (a) simulated and (b) measured gain patterns in the $\phi = 90^\circ$ plane of the square ring antenna, loaded with a horizontal gap, at loaded mode frequency, $f_{LI} = 1.64$ GHz. The antenna parameters are the same as in caption of Fig. 5.19.

5.7 Modified gap-loaded square ring antenna

The lowest loaded mode frequency of the gap-loaded square ring antenna can be lowered further by modifying slot shape inside the square ring. The designs in Fig. 5.22(a) and 5.22(b) have been proposed in [23, 24]. Here a capacitive feeding is used, because the ring width is very narrow, and as such, probe-feed becomes impossible. The feed line and the ring are etched on a substrate with dielectric permittivity $\epsilon_r = 2.5$, and thickness of 0.79 mm, which is placed over the infinite ground plane with a foam in between, having a thickness of 6.35 mm. The feed line impedance is 50- Ω , which is excited by an SMA probe.

Other variations of the slot can also be possible, and an example is shown in Fig. 5.22(c). In all three cases, $g = 1$ mm. The main idea here is to lengthen the current flow path, which lowers the loaded mode frequency. The ring size is 12 mm \times 12 mm for all three cases. Note that a 12 mm-square patch on a substrate, with dielectric permittivity $\epsilon_r = 2.5$, and thickness of 0.79 mm, will operate at 7.5 GHz. Antenna # (a) operates at 2.184 GHz, as shown in Fig. 5.23, which indicates a size reduction of about 70.8%. Similarly, loaded mode frequency of antenna # (b) is 1.71 GHz, and that of antenna # (c) is 1.43 GHz, indicating size reductions of 77.2% and 80.9%, respectively, compared to the square patch antenna. However, from Table 5.5, we can see that as the antenna size gets smaller, the bandwidth gets narrower.

Again, as the current is much higher at the edges of narrow strips, the resistive losses are much higher. Therefore, the gain level is very low, especially for antenna # (b)

and antenna # (c), as can be found in Figs. 5.24-5.26. In the next chapter, we are going to present a method to reduce the resistive loss, and enhance the gain of miniaturized microstrip antennas.

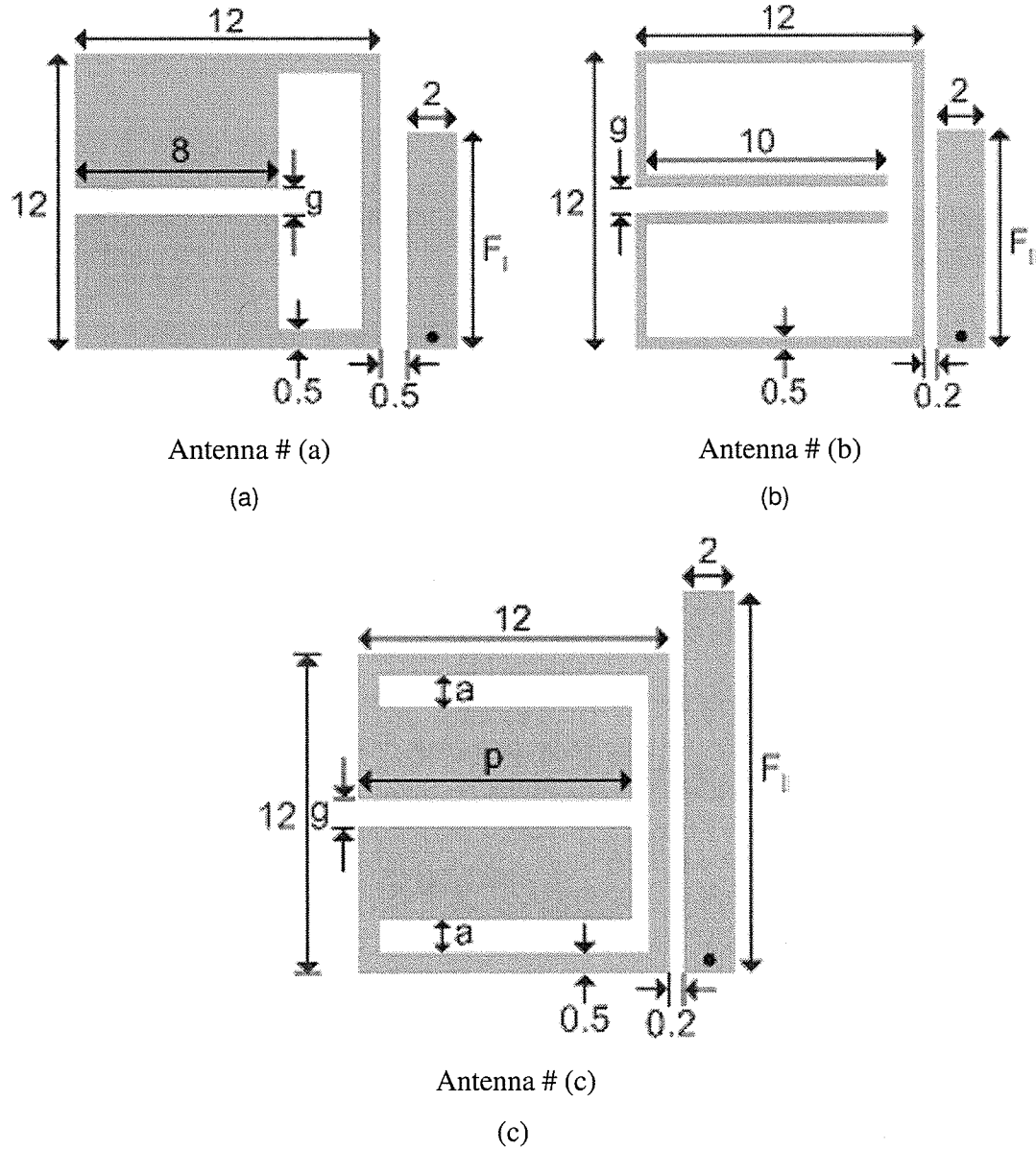


Fig. 5.22: Modified open square ring antenna geometries: antennas # (a) and (b) are from [23, 24]. For antenna # (c), $a = 2$ mm.

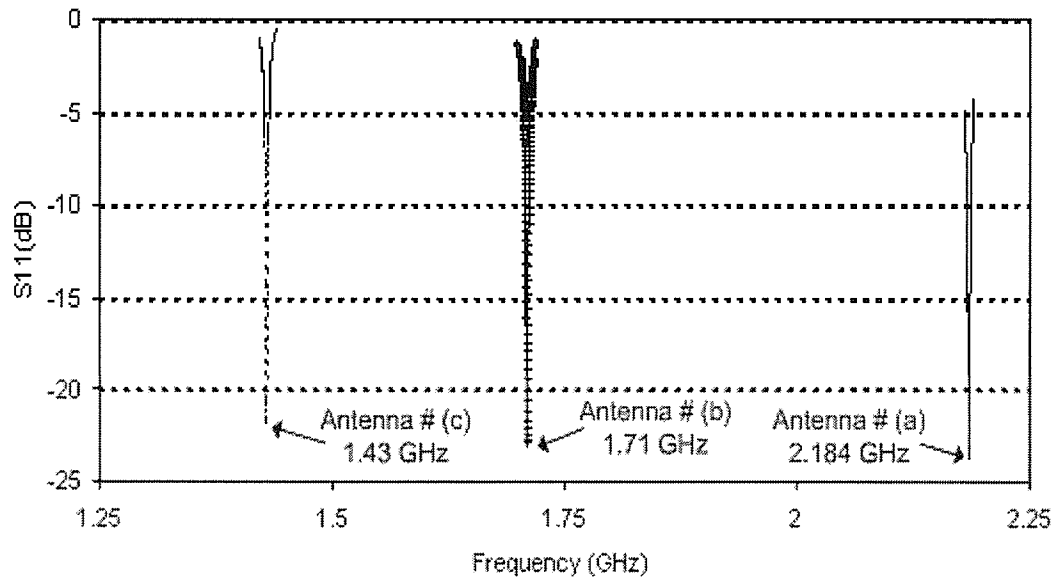


Fig. 5.23: Return losses of the modified open square ring antennas in Fig. 5.22.

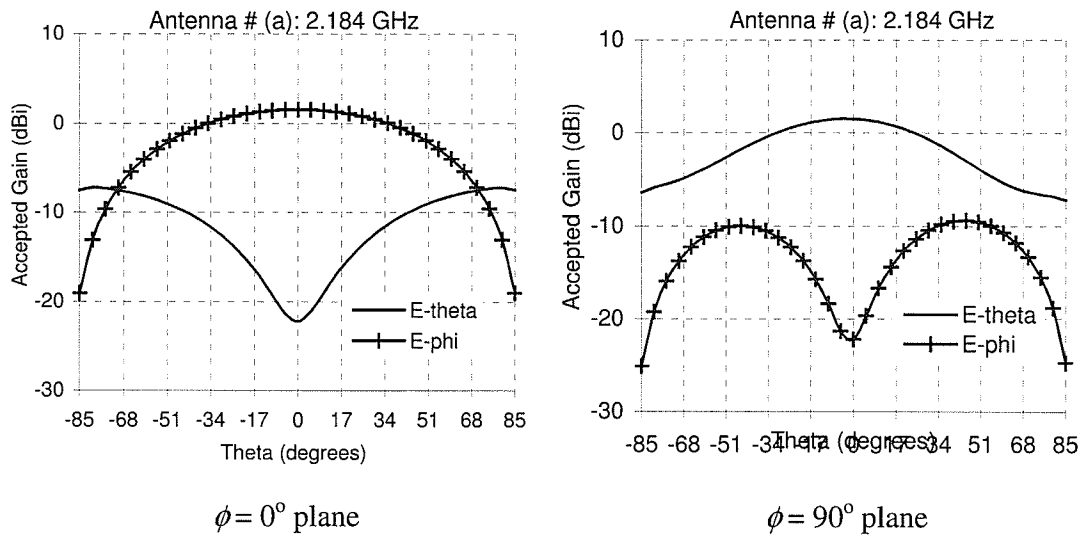


Fig. 5.24: Gain patterns in two principal planes of the modified open square ring antenna [Antenna # (a), Fig. 5.22(a)].

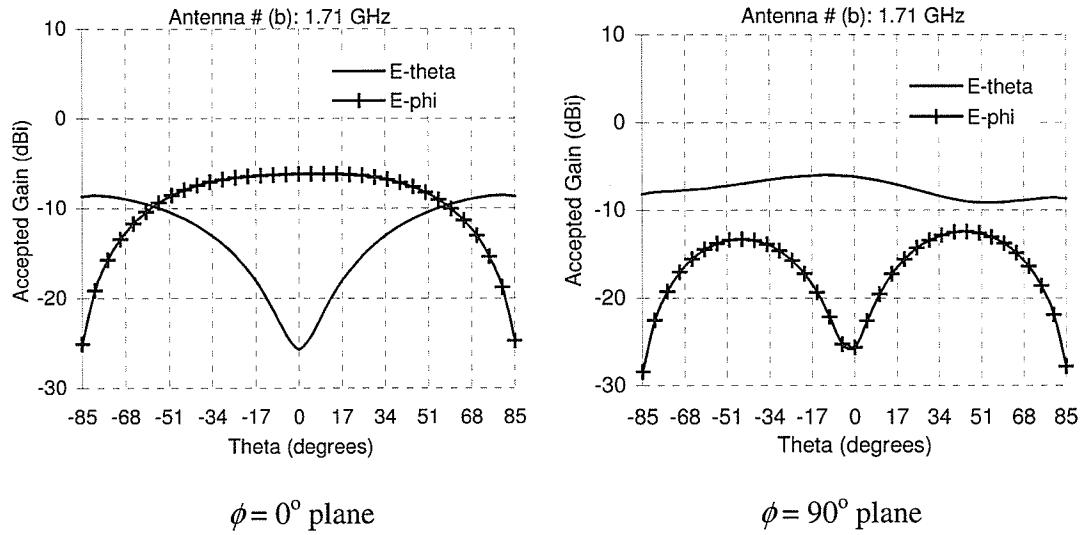


Fig. 5.25: Gain patterns in two principal planes of the modified open square ring antenna [Antenna # (a), Fig. 5.22(b)].

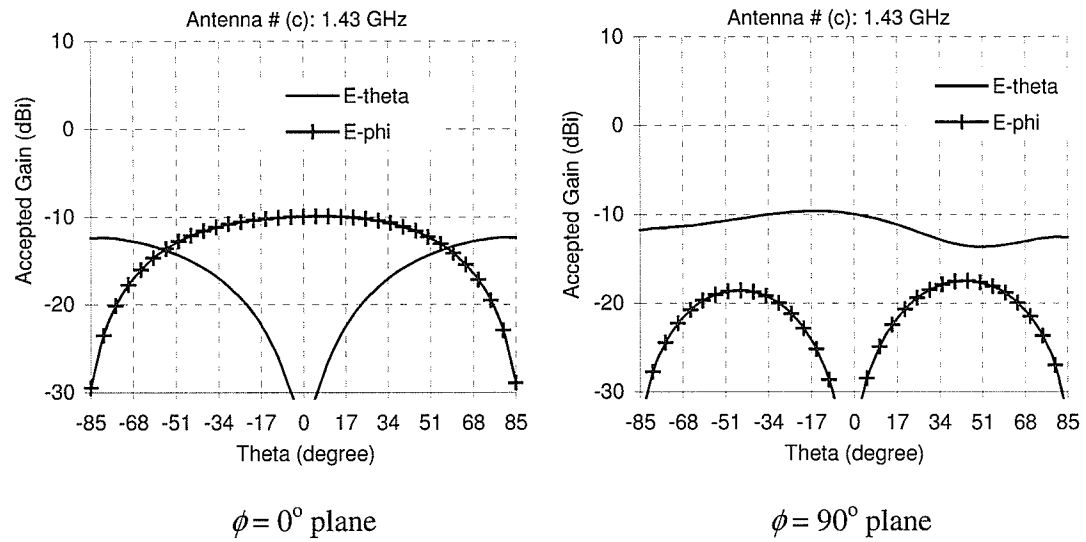


Fig. 5.26: Gain patterns in two principal planes of the modified open square ring antenna [Antenna # (a), Fig. 5.22(c)].

Table 5.5: Performance properties of the modified open square ring antennas in Fig. 4.10 on infinite ground plane

Antenna	Feed line length	Loaded mode frequency (GHz)	10-dB RL BW (MHz)	Gain (accepted) at loaded mode frequency (dBi)	
				$\phi = 0^\circ$	$\phi = 90^\circ$
# (a)	$F_1 = 6 \text{ mm}$	2.184	2183 – 2187 (= 4 MHz) 0.206%	Co: 1.52 Cross: -22	Co: 1.52 Cross: -22
# (b)	$F_1 = 10 \text{ mm}$	1.71	1709 – 1712 (= 3 MHz) 0.205%	Co: -6.22 Cross: -25.64	Co: -6.22 Cross: -25.64
# (c)	$F_1 = 18 \text{ mm}$	1.43	1427 – 1429.7 (= 2.7 MHz) 0.18%	Co: -9.98 Cross: -33	Co: -9.98 Cross: -33

5.8 Conclusion

In this chapter, the loaded and unloaded modes of the gap-loaded square ring antenna were discussed. Because of loading, two more resonances were noticed around the unloaded mode frequency. The important features of the loaded modes were presented with a parametric study. A relationship was established among loaded and unloaded mode frequencies. The simulated results were confirmed with experimental results. The first loaded mode frequency was much lower than the unloaded mode frequency of the square ring, which indicated a huge size reduction. However, the gain at

this frequency was too low. The slot inside the square ring could be modified to lower the loaded mode frequency, to obtain even smaller microstrip antenna. Again, the main problem with these modified open square ring antennas was their poor gain, due to high ohmic losses, which resulted from the high currents at the edges of the narrow rings. In the next chapter, a multi-layer laminated conductor concept will be presented which has the capability of reducing the resistive losses.

CHAPTER SIX

Gain Improvement of Miniaturized Square Ring Antennas

6.1 Introduction

Miniaturized antennas normally have poor gain and efficiency. In the case of miniaturized microstrip antennas, such as miniaturized square ring antennas presented in the previous chapter, high ohmic loss is the main cause of their reduced gain and efficiency. For a simple square ring antenna, this can be explained easily using the current distribution on the strip of the ring. As mentioned earlier, narrower width ($L_2/L_1 =$ large) of the square ring antenna indicates smaller antenna. As shown in Fig. 6.1, when the width of square ring is made very narrow ($L_2/L_1 = 0.93$) to make square ring antenna smaller, the currents become excessively large at inner and outer edges of the ring, compared to that of a square ring antenna with wider strip width. Therefore, I^2R loss, or conductor loss, is much higher, which contributes to reduced gain and efficiency.

To reduce the resistive loss in coaxial cables and transmission lines, laminated conductors have been used, each having thickness less than or around skin depth, instead of a single conductor, which essentially increases the penetration depth of the electromagnetic wave [25, 26]. Here, a multi-layered planar conductor is studied to explain the concept of laminated conductor. Since microstrip antennas are formed with

conductors, the patch conductor and the ground conductor, the same concept is used for miniaturized square ring microstrip antennas to enhance their gain.

In order to show its generality and applicability, several miniaturized microstrip antennas, such as square ring antenna, H-shaped patch antenna, and modified loaded square ring antenna, are considered. Multiple laminated conductor layers are used instead of a single conductor layer, to form the conducting patches of these antennas, and the effect in reduction in resistive losses is discussed in detail. Effects of laminating material permittivity and thickness are studied. Measurement results are presented to support the discussion.

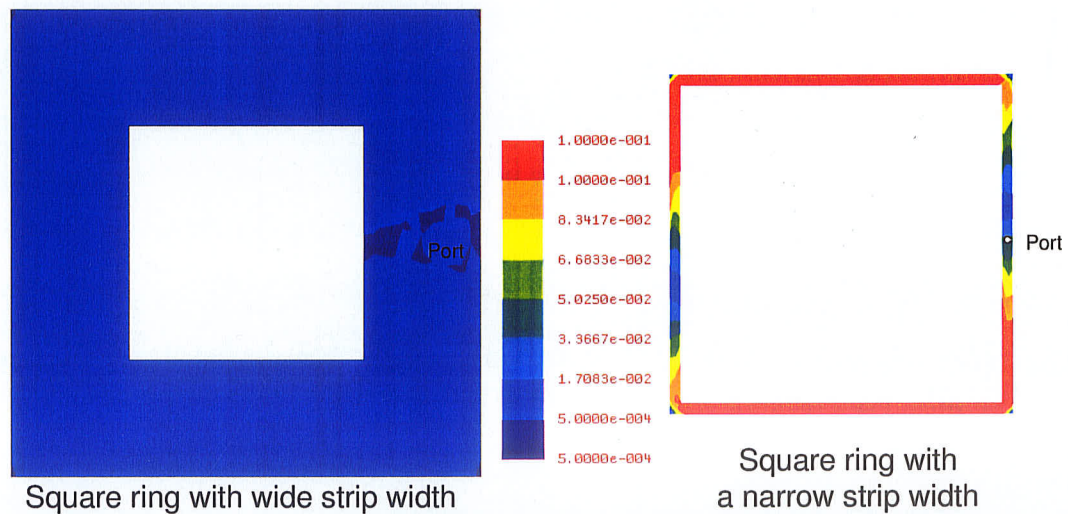


Fig. 6.1: Current distributions on the square ring antennas with wide and narrow strip widths, at their resonance frequencies.

6.2 Multi-layered planar conductor to reduce loss

Let us first consider a planar lossy material, having thickness a , dielectric permittivity ϵ_m , permeability μ_m , and conductivity σ_m (medium 2) in Fig. 6.2. This medium can be characterized by the propagation factor k_m , which can be expressed by the following equation in terms of the material properties:

$$k_m = \omega \sqrt{\mu_m \epsilon_m} \sqrt{1 - j \frac{\sigma_m}{\omega \epsilon_m}} \quad (6.1)$$

where ω is the angular frequency, and is defined by

$$\omega = 2\pi f \quad (6.2)$$

Here, f is the operating frequency.

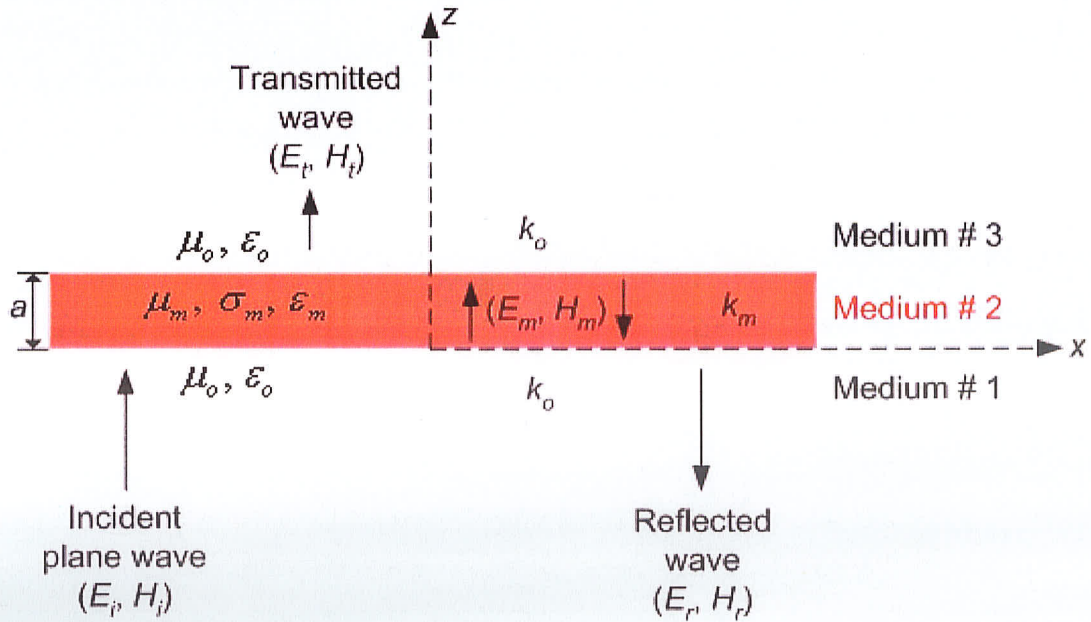


Fig. 6.2: Planar lossy material with plane wave incidence.

A uniform plane wave is propagating in the $+z$ direction in free-space (medium 1), and impinges normally at a plane boundary with medium 2 at $z = 0$. Medium 1 has a dielectric permittivity of ϵ_o and a permeability of μ_o , and its propagation factor is given by:

$$k_0 = \omega \sqrt{\mu_o \epsilon_o} \quad (6.3)$$

There will be reflection and transmission at this boundary [72, 73]. An x - or y -polarized incident field can be considered. The electric and magnetic fields for the incident and reflected waves in medium 1 are:

$$E_i = C_0 \exp(-jk_0 z) \quad (6.4)$$

$$E_r = C_1 \exp(jk_0 z) \quad (6.5)$$

$$H_i = \frac{k_0}{\omega \mu_o} C_0 \exp(-jk_0 z) \quad (6.6)$$

$$H_r = -\frac{k_0}{\omega \mu_o} C_1 \exp(jk_0 z) \quad (6.7)$$

Therefore, the total electric and magnetic fields in medium 1 is the sum of the incident component and reflected component:

$$E_1 = C_0 \exp(-jk_0 z) + C_1 \exp(jk_0 z) \quad (6.8)$$

$$H_1 = \frac{k_0}{\omega \mu_o} C_0 \exp(-jk_0 z) - \frac{k_0}{\omega \mu_o} C_1 \exp(jk_0 z) \quad (6.9)$$

The remaining part of the incident wave will be transmitted to medium 2, and the field within this medium can be represented by both forward and backward waves:

$$E_m = E_2 = C_2 \exp(-jk_m z) + C_3 \exp(jk_m z) \quad (6.10)$$

$$H_m = H_2 = \frac{k_m}{\omega\mu_m} C_2 \exp(-jk_m z) - \frac{k_m}{\omega\mu_m} C_3 \exp(jk_m z) \quad (6.11)$$

In medium 3, only forward wave in +z direction exists, which is the transmitted wave:

$$E_t = E_3 = C_4 \exp(-jk_0 z) \quad (6.12)$$

$$H_t = H_3 = \frac{k_0}{\omega\mu_0} C_4 \exp(-jk_0 z) \quad (6.13)$$

The continuity of the tangential components at the interfaces requires that at $z=0$,

$E_1 = E_2$, which gives

$$-C_1 + C_2 + C_3 = 1 \quad (6.14)$$

At $z=0$, $H_1 = H_2$, which gives

$$C_1 \left(\frac{k_0}{\omega\mu_0} \right) + C_2 \left(\frac{k_m}{\omega\mu_m} \right) + C_3 \left(-\frac{k_m}{\omega\mu_m} \right) = \left(\frac{k_0}{\omega\mu_0} \right) \quad (6.15)$$

At $z=a$, $E_2 = E_3$, which gives

$$C_2 [\exp(-jk_m a)] + C_3 [\exp(jk_m a)] - C_4 [\exp(-jk_0 a)] = 0 \quad (6.16)$$

At $z=a$, $H_2 = H_3$, which gives

$$C_2 \left(\frac{k_m}{\omega\mu_m} \right) [\exp(-jk_m a)] - C_3 \left(\frac{k_m}{\omega\mu_m} \right) [\exp(jk_m a)] - C_4 \left(-\frac{k_0}{\omega\mu_0} \right) [\exp(-jk_0 a)] = 0 \quad (6.17)$$

Therefore, we have four equations: equations (6.14)-(6.17), and four unknown amplitudes: C_1 , C_2 , C_3 and C_4 , considering C_0 , the amplitude of the incident wave, to be known, and equal to 1. These four equations can be expressed in a matrix form, as shown in equation (6.18):

$$\begin{bmatrix} -1 & 1 & 1 & 0 \\ \frac{k_0}{\omega\epsilon_0} & \frac{k_m}{\omega\epsilon_m} & -\frac{k_m}{\omega\epsilon_m} & 0 \\ 0 & \exp(-jk_m a) & \exp(jk_m a) & -\exp(-jk_0 a) \\ 0 & \frac{k_m}{\omega\epsilon_m} \exp(-jk_m a) & -\frac{k_m}{\omega\epsilon_m} \exp(jk_m a) & -\frac{k_0}{\omega\epsilon_0} \exp(-jk_0 a) \end{bmatrix} \begin{bmatrix} C_1 \\ C_2 \\ C_3 \\ C_4 \end{bmatrix} = \begin{bmatrix} 1 \\ \frac{k_0}{\omega\epsilon_0} \\ 0 \\ 0 \end{bmatrix} \quad (6.18)$$

The four unknowns can be found by solving the matrix, and thus, the reflected and transmitted powers can be calculated. Based on the transmitted and reflected powers, the power lost inside the lossy material can be found using the following equations:

$$P_L = \frac{1}{2\eta} - \frac{|C_1|^2}{2\eta} - \frac{|C_4|^2}{2\eta} \quad (6.19)$$

where, η is the wave impedance. The first term in the above equation is the incident power, the second term is the reflected power and the third term is the transmitted power.

Medium 2 in Fig. 6.2 can be conductor or dielectric, based on the material properties. If we consider a conducting material with a finite thickness having $\epsilon_m = 1$, the power lost in the material decreases as the conductivity, σ_m increases, as shown in Fig. 6.3. Moreover, the power loss increases with frequency. The power loss is calculated using equation (6.19). The MATLAB code, to solve the matrix in equation (6.18) and to calculate the power loss, is presented in Appendix B.

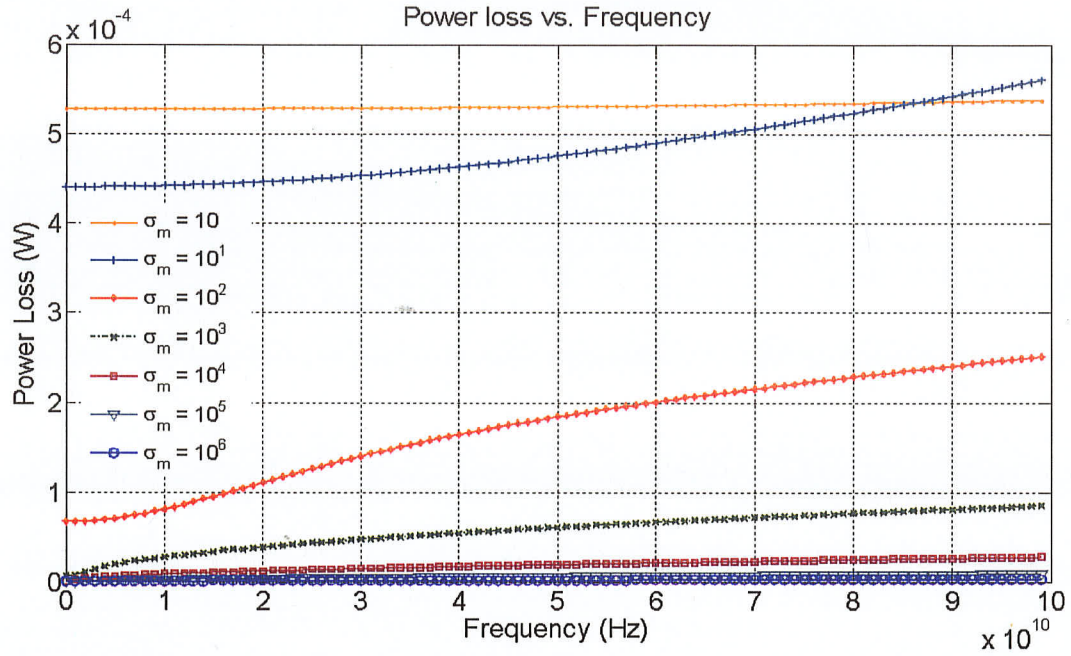


Fig. 6.3: Power loss vs. frequency for the lossy material in Fig. 6.2 for thickness of $a = 200 \mu\text{m}$.

We can extend the discussion to a three-layer system with alternate medium, as shown in Fig. 6.4. Media 2 and 4 are of the same material, with medium 3 in between having dielectric permittivity ϵ_l , permeability μ_l , and conductivity σ_l . Media 1 and 5 are free-space regions. The layered material system in Fig. 6.4 can be considered as a planar conductor with conducting material in media 2 and 4, each having a thickness of t_m , and a laminating dielectric layer with a thickness t_l and negligible σ_l in media 3. The overall thickness of the planar conductor is t . The propagation factor k_l of the dielectric layer can be expressed as follows:

$$k_l = \omega \sqrt{\mu_l \epsilon_l} \quad (6.20)$$

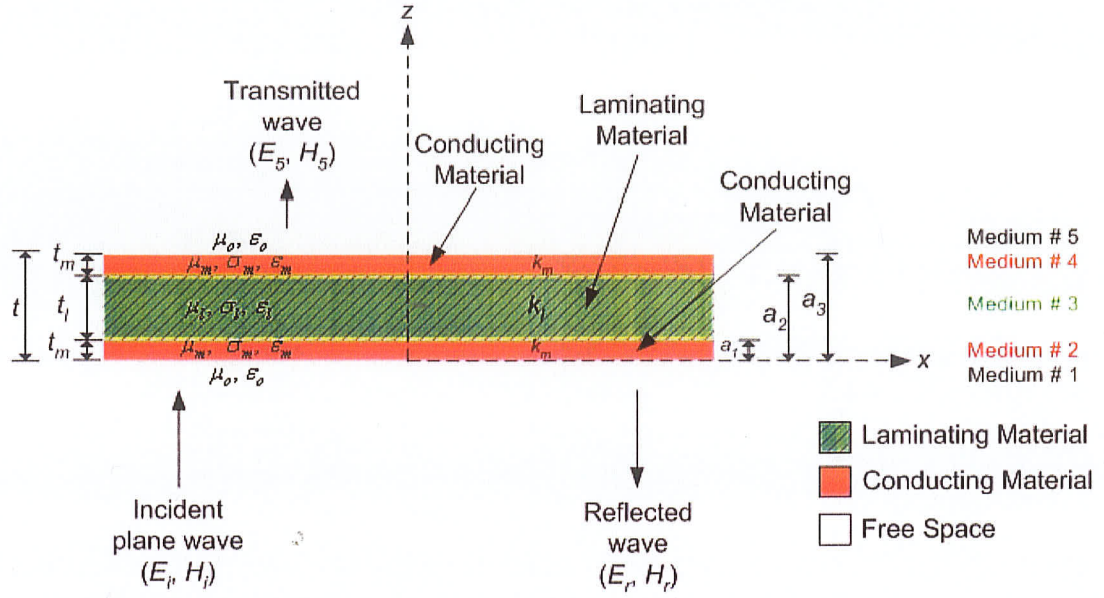


Fig. 6.4: Planar conductor with alternating laminating material with normal plane wave incidence: three layers.

If we consider a normal wave incidence at the boundary $z = 0$, then as previously, we can write the field equations in five regions, and apply the boundary condition:

Medium 1:

$$E_1 = C_0 \exp(-jk_0 z) + C_1 \exp(jk_0 z) \quad (6.21)$$

$$H_1 = \frac{k_0}{\omega \mu_0} C_0 \exp(-jk_0 z) - \frac{k_0}{\omega \mu_0} C_1 \exp(jk_0 z) \quad (6.22)$$

Medium 2:

$$E_2 = C_2 \exp(-jk_m z) + C_3 \exp(jk_m z) \quad (6.23)$$

$$H_2 = \frac{k_m}{\omega\mu_m} C_2 \exp(-jk_m z) - \frac{k_m}{\omega\mu_m} C_3 \exp(jk_m z) \quad (6.24)$$

Medium 3:

$$E_3 = C_4 \exp(-jk_l z) + C_5 \exp(jk_l z) \quad (6.25)$$

$$H_3 = \frac{k_l}{\omega\mu_l} C_4 \exp(-jk_l z) - \frac{k_l}{\omega\mu_l} C_5 \exp(jk_l z) \quad (6.26)$$

Medium 4:

$$E_4 = C_6 \exp(-jk_m z) + C_7 \exp(jk_m z) \quad (6.27)$$

$$H_4 = \frac{k_m}{\omega\mu_m} C_6 \exp(-jk_m z) - \frac{k_m}{\omega\mu_m} C_7 \exp(jk_m z) \quad (6.28)$$

Medium 5:

$$E_5 = C_8 \exp(-jk_0 z) \quad (6.29)$$

$$H_5 = \frac{k_0}{\omega\mu_0} C_8 \exp(-jk_0 z) \quad (6.30)$$

If we apply the boundary condition of matching tangential electric and magnetic fields along the boundaries $z = 0$, $z = a_1$, $z = a_2$, and $z = a_3$, we are going to have eight equations for eight unknown amplitudes: C_1 , C_2 , C_3 , C_4 , C_5 , C_6 , C_7 and C_8 , which can be expressed in matrix form, as shown below:

$$\begin{bmatrix}
-1 & 1 & 1 & 0 & 0 & 0 & 0 & 0 \\
\frac{k_0}{\omega\epsilon_0} & \frac{k_m}{\omega\epsilon_m} & -\frac{k_m}{\omega\epsilon_m} & 0 & 0 & 0 & 0 & 0 \\
0 & \exp(-jk_m a_1) & \exp(jk_m a_1) & -\exp(-jk_l a_1) & -\exp(jk_l a_1) & 0 & 0 & 0 \\
0 & \frac{k_m}{\omega\epsilon_m} \exp(-jk_m a_1) & -\frac{k_m}{\omega\epsilon_m} \exp(jk_m a_1) & -\frac{k_l}{\omega\epsilon_l} \exp(-jk_l a_1) & \frac{k_l}{\omega\epsilon_l} \exp(jk_l a_1) & 0 & 0 & 0 \\
0 & 0 & 0 & \exp(-jk_l a_2) & \exp(jk_l a_2) & -\exp(-jk_m a_2) & -\exp(jk_m a_2) & 0 \\
0 & 0 & 0 & \frac{k_l}{\omega\epsilon_l} \exp(-jk_l a_2) & -\frac{k_l}{\omega\epsilon_l} \exp(jk_l a_2) & -\frac{k_m}{\omega\epsilon_m} \exp(-jk_m a_2) & \frac{k_m}{\omega\epsilon_m} \exp(jk_m a_2) & 0 \\
0 & 0 & 0 & 0 & 0 & \exp(-jk_m a_3) & \exp(jk_m a_3) & -\exp(-jk_0 a_3) \\
0 & 0 & 0 & 0 & 0 & \frac{k_m}{\omega\epsilon_m} \exp(-jk_m a_3) & -\frac{k_m}{\omega\epsilon_m} \exp(jk_m a_3) & -\frac{k_0}{\omega\epsilon_0} \exp(-jk_0 a_3)
\end{bmatrix}
\begin{bmatrix}
C_1 \\
C_2 \\
C_3 \\
C_4 \\
C_5 \\
C_6 \\
C_7 \\
C_8
\end{bmatrix}
=
\begin{bmatrix}
1 \\
\frac{k_0}{\omega\epsilon_0} \\
0 \\
0 \\
0 \\
0 \\
0 \\
0
\end{bmatrix}
\quad (6.31)$$

In this case, the power lost in three layers will be:

$$P_L = \frac{1}{2\eta} - \frac{|C_1|^2}{2\eta} - \frac{|C_8|^2}{2\eta} \quad (6.32)$$

where C_1 and C_8 are the amplitude of the reflected and transmitted waves in media 1 and 5, respectively.

Now, if we want to consider ‘ n ’ number of layers, where the conducting layer and the laminating dielectric layer will repeat several times, we have a system of planar conductor, as shown in Fig.6.5. Considering two free-space regions, there are $n + 2$ numbers of media.

We can write field equations as we have done for the three-layer case for different media starting from medium 1, and continue until the free-space region after the last layer, as also suggested for layered dielectric media in [74]. The electric and magnetic fields for the last layer can be written as follows:

$$E_{2n} = C_{2n} \exp(-jk_m z) + C_{2n+1} \exp(jk_m z) \quad (6.33)$$

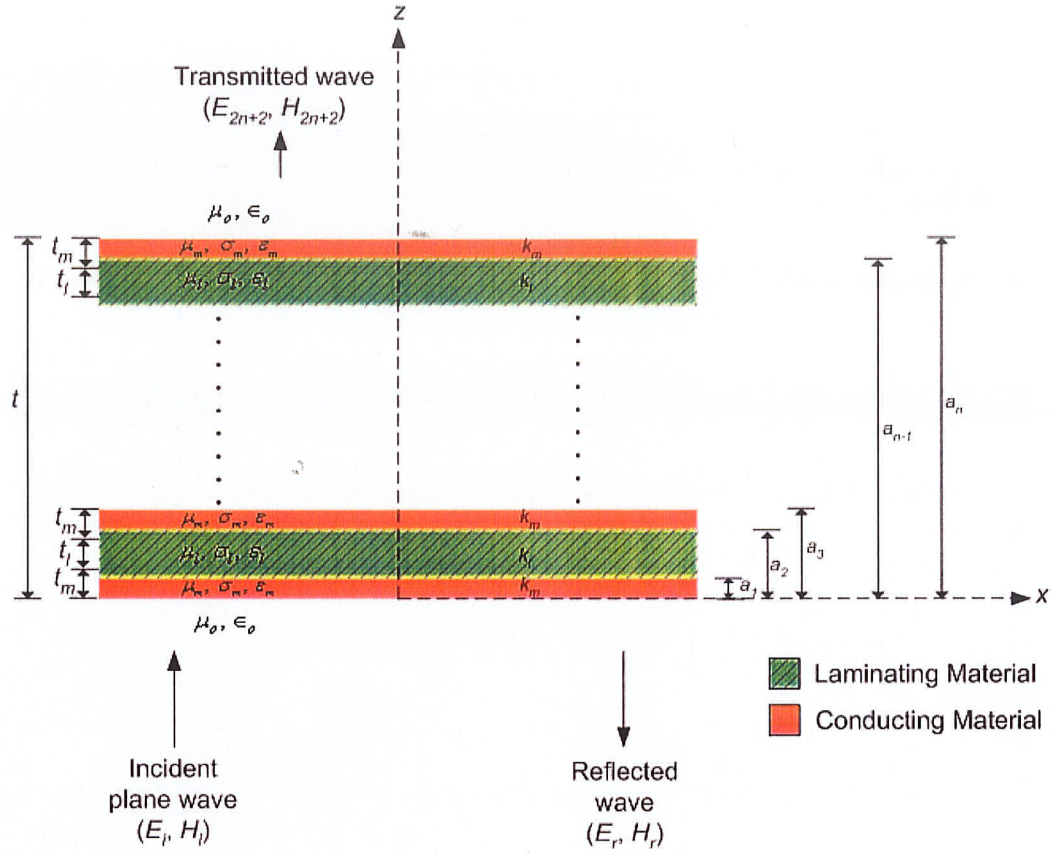


Fig. 6.5: Planar conductor with alternating laminating material with normal plane wave incidence: 'n' number of layers.

$$H_{2n} = \frac{k_m}{\omega\mu_m} C_{2n} \exp(-jk_m z) - \frac{k_m}{\omega\mu_m} C_{2n+1} \exp(jk_m z) \quad (6.34)$$

For the free-space region,

$$E_{2n+2} = C_{2n+2} \exp(-jk_0 z) \quad (6.35)$$

$$H_{2n+2} = \frac{k_0}{\omega\mu_0} C_{2n+2} \exp(-jk_0 z) \quad (6.36)$$

Applying the matching boundary condition at the boundaries $z = 0, a_1, a_2, a_3, \dots, a_n$, we will get $2n + 2$ number of equations for $2n + 2$ number of unknown amplitudes: $C_1, C_2, C_3, \dots, C_{2n+2}$. These equations can be represented in matrix form as shown below to solve for the unknowns:

$$\begin{bmatrix} M_{1,1} & M_{1,2} & M_{1,3} & 0 & 0 & 0 & 0 & \dots & 0 & 0 & 0 \\ M_{2,1} & M_{2,2} & M_{2,3} & 0 & 0 & 0 & 0 & \dots & 0 & 0 & 0 \\ 0 & M_{3,2}d_1 & M_{3,3}d_1 & M_{3,4}d_1 & M_{3,5}d_1 & 0 & 0 & \dots & 0 & 0 & 0 \\ 0 & M_{4,2}d_1 & M_{4,3}d_1 & M_{4,4}d_1 & M_{4,5}d_1 & 0 & 0 & \dots & 0 & 0 & 0 \\ 0 & 0 & 0 & M_{5,4}d_2 & M_{5,5}d_2 & M_{5,6}d_2 & M_{5,7}d_2 & \dots & 0 & 0 & 0 \\ 0 & 0 & 0 & M_{6,4}d_2 & M_{6,5}d_2 & M_{6,6}d_2 & M_{6,7}d_2 & \dots & 0 & 0 & 0 \\ \vdots & \vdots & \vdots & \vdots & \vdots & \vdots & \vdots & \ddots & \vdots & \vdots & \vdots \\ 0 & 0 & 0 & 0 & 0 & 0 & 0 & \dots & M_{2n+1,2n}d_n & M_{2n+1,2n+1}d_n & M_{2n+1,2n+2}d_n \\ 0 & 0 & 0 & 0 & 0 & 0 & 0 & \dots & M_{2n+2,2n}d_n & M_{2n+2,2n+1}d_n & M_{2n+2,2n+2}d_n \end{bmatrix} \begin{bmatrix} C_1 \\ C_2 \\ C_3 \\ C_4 \\ C_5 \\ C_6 \\ \vdots \\ C_{2n+1} \\ C_{2n+2} \end{bmatrix} = \begin{bmatrix} Y_1 \\ Y_2 \\ 0 \\ 0 \\ 0 \\ 0 \\ \vdots \\ 0 \\ 0 \end{bmatrix} \quad (6.37)$$

Here, $M_{1,1} = -1, M_{1,2} = 1, M_{1,3} = -1, Y_1 = 1$ and $Y_2 = \frac{k_0}{\omega \epsilon_0}$. Also,

$$M_{2,1} = \frac{k_0}{\omega \epsilon_0} \quad (6.38)$$

$$M_{2,2} = \frac{k_m}{\omega \epsilon_m} \quad (6.39)$$

$$M_{2,3} = -\frac{k_m}{\omega \epsilon_m} \quad (6.40)$$

$$M_{3,2}d_1 = \exp(-jk_m a_1) \quad (6.41)$$

$$M_{3,3}d_1 = \exp(jk_m a_1) \quad (6.42)$$

$$M_{3,4}d_1 = -\exp(-jk_l a_1) \quad (6.43)$$

$$M_{3,5}d_1 = -\exp(jk_l a_1) \quad (6.44)$$

$$M_{4,2}d_1 = \frac{k_m}{\omega \epsilon_m} \exp(-jk_m a_1) \quad (6.45)$$

$$M_{4,3}d_1 = -\frac{k_m}{\omega \epsilon_m} \exp(jk_m a_1) \quad (6.46)$$

$$M_{4,4}d_1 = -\frac{k_l}{\omega \epsilon_l} \exp(-jk_l a_1) \quad (6.47)$$

$$M_{4,5}d_1 = \frac{k_l}{\omega \epsilon_l} \exp(jk_l a_1) \quad (6.48)$$

$$M_{5,4}d_2 = \exp(-jk_l a_2) \quad (6.49)$$

$$M_{5,5}d_2 = \exp(jk_l a_2) \quad (6.50)$$

$$M_{5,6}d_2 = -\exp(-jk_m a_2) \quad (6.51)$$

$$M_{5,7}d_2 = -\exp(jk_m a_2) \quad (6.51)$$

$$M_{6,4}d_2 = \frac{k_l}{\omega \epsilon_l} \exp(-jk_l a_2) \quad (6.52)$$

$$M_{6,4}d_2 = -\frac{k_l}{\omega \epsilon_l} \exp(jk_l a_2) \quad (6.53)$$

$$M_{6,4}d_2 = -\frac{k_m}{\omega\epsilon_m}\exp(-jk_ma_2) \quad (6.54)$$

$$M_{6,4}d_2 = \frac{k_m}{\omega\epsilon_m}\exp(jk_ma_2) \quad (6.55)$$

•

•

•

•

•

•

•

$$M_{2n+1,2n}d_n = \exp(-jk_ma_n) \quad (6.56)$$

$$M_{2n+1,2n+1}d_n = \exp(jk_ma_n) \quad (6.57)$$

$$M_{2n+1,2n+2}d_n = -\exp(-jk_0a_n) \quad (6.58)$$

$$M_{2n+2,2n}d_n = \frac{k_m}{\omega\epsilon_m}\exp(-jk_ma_n) \quad (6.59)$$

$$M_{2n+2,2n+1}d_n = -\frac{k_m}{\omega\epsilon_m}\exp(jk_ma_n) \quad (6.60)$$

$$M_{2n+2,2n+2}d_n = -\frac{k_0}{\omega\epsilon_0}\exp(-jk_0a_n) \quad (6.61)$$

For this n -layer system of planar conductor, the power lost can be calculated using the following equation:

$$P_L = \frac{1}{2\eta} - \frac{|C_1|^2}{2\eta} - \frac{|C_{2n+2}|^2}{2\eta} \quad (6.62)$$

In this case, C_1 and C_{2n+2} are the amplitudes of the reflected and transmitted waves, respectively. By solving the matrix in equation (6.37), power lost in the laminated conductor system in Fig. 6.5 can be calculated. A MATLAB code, to solve this matrix, is attached in Appendix C.

The main aim of this formulation is to evaluate the performance of a planar conductor, where several layers of conducting material, each one laminated with a dielectric material having a thickness in the order of skin depth, are used. Before we start the discussion on the loss in the planar laminated conductor, the definition of skin depth is given first.

In good conductors, a high-frequency electromagnetic wave is attenuated very rapidly as it propagates in a good conductor [73, 75]. The depth of wave penetration in good conductor is called ‘skin depth’, and is defined by:

$$\delta = \frac{1}{\sqrt{\pi f \mu \sigma}} \quad (6.63)$$

For the convenience of the readers, several tables are attached in Appendix D with different skin depths for different conductivities, σ .

MATLAB plots are discussed next to see the effects of having multiple laminated conducting layers on the loss of the planar conductor. For conductivity $\sigma_m = 10^5$, Fig. 6.6 shows that when several laminated conducting layers are used, instead of a single conducting material layer, loss decreases. Each laminated conductor layer, the thickness of which is designated as t_c , comprises a conducting layer with an infinitesimal thickness and the laminating dielectric layer having a thickness (t_l) around the skin depth for a given frequency range. Although the thickness of the conducting layer is infinitesimal, there will be finite surface current distribution on the surface of the conducting material, which will cause finite ohmic losses. The significant loss reduction occurs when a few number of laminated conductor layers (2 or 5) are used. Although with 15 layers or more, the loss reduction can be observed, however, after 25 layers, the loss reduction is not significant, but still the power loss is less than that of the single layer case. The overall thickness (t) increases as more number of layers is used, and t is much higher compared to the skin depth of the conducting material.

If we restrict the overall thickness t , as the number of laminated conducting layers increases, the loss reduces, as shown in Figs. 6.7 and 6.8 for two conductivities: $\sigma_m = 10^3$ and $\sigma_m = 10^5$. When the conductivity is higher, the loss is less, as can be noticed in these figures. For each case, the laminated conductor thickness is smaller than the skin depth. Note that for large number of layers, the laminated conductor layer thickness becomes much smaller than the skin depth, which translates into lower loss compared to that of few number of layers. However, the amount of reduction in loss is small for the case with

large number of layers, compared to that with less number of layers. In both cases, the overall thickness (t) is fairly larger than the skin depth. However, when higher overall thickness is used, no significant loss reduction is observed, Fig. 6.9. Slightly higher loss can be observed at the higher frequencies, in this case.

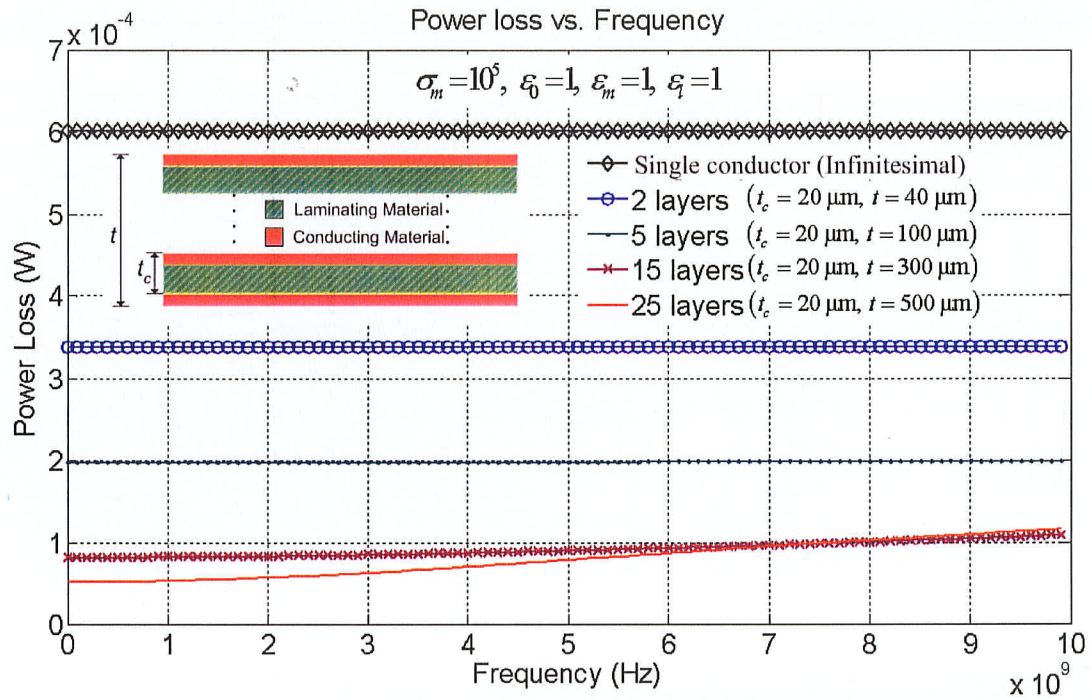


Fig. 6.6: Loss reduction due to the use of multiple laminated conductors instead of a single conducting layer, with $t_c = 20 \mu\text{m}$. Skin depth at 1 GHz is $50.3 \mu\text{m}$ for $\sigma_m = 10^5$.

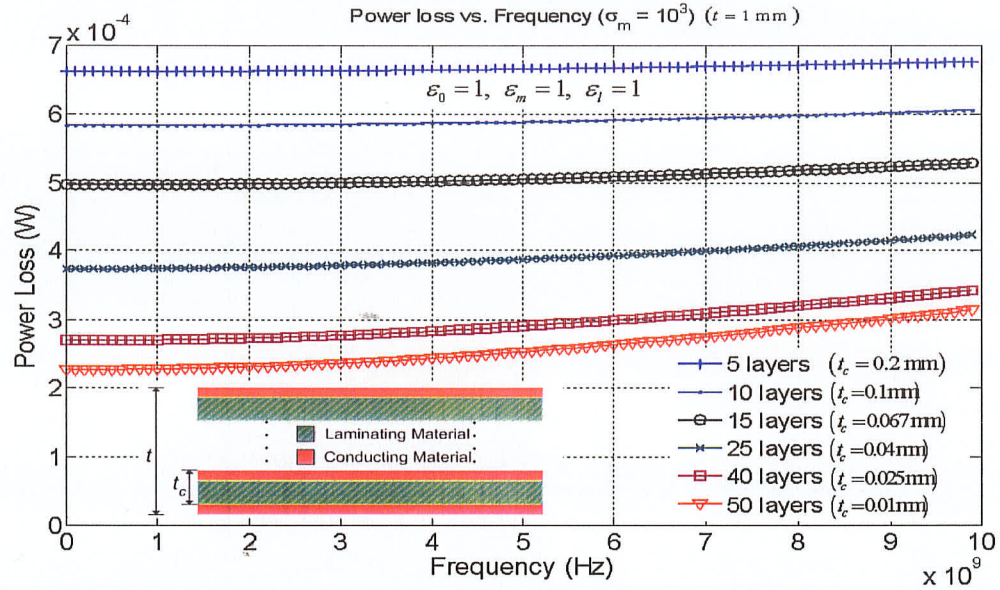


Fig. 6.7: Loss reduction due to the use of many laminated conductor layers with smaller thickness of each layer: $\sigma_m = 10^3$, $t = 1$ mm. Skin depth at 1 GHz is 503 μm for $\sigma_m = 10^3$.

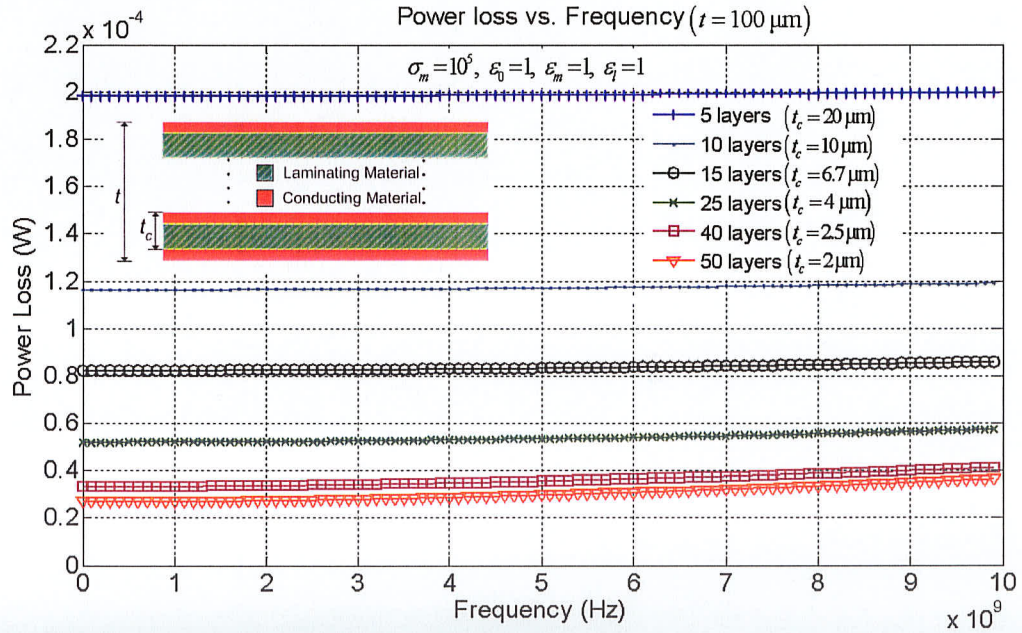


Fig. 6.8: Loss reduction due to the use of many laminated conductor layers with smaller thickness of each layer: $\sigma_m = 10^5$, $t = 100$ μm . Skin depth at 1 GHz is 50.3 μm for $\sigma_m = 10^5$.

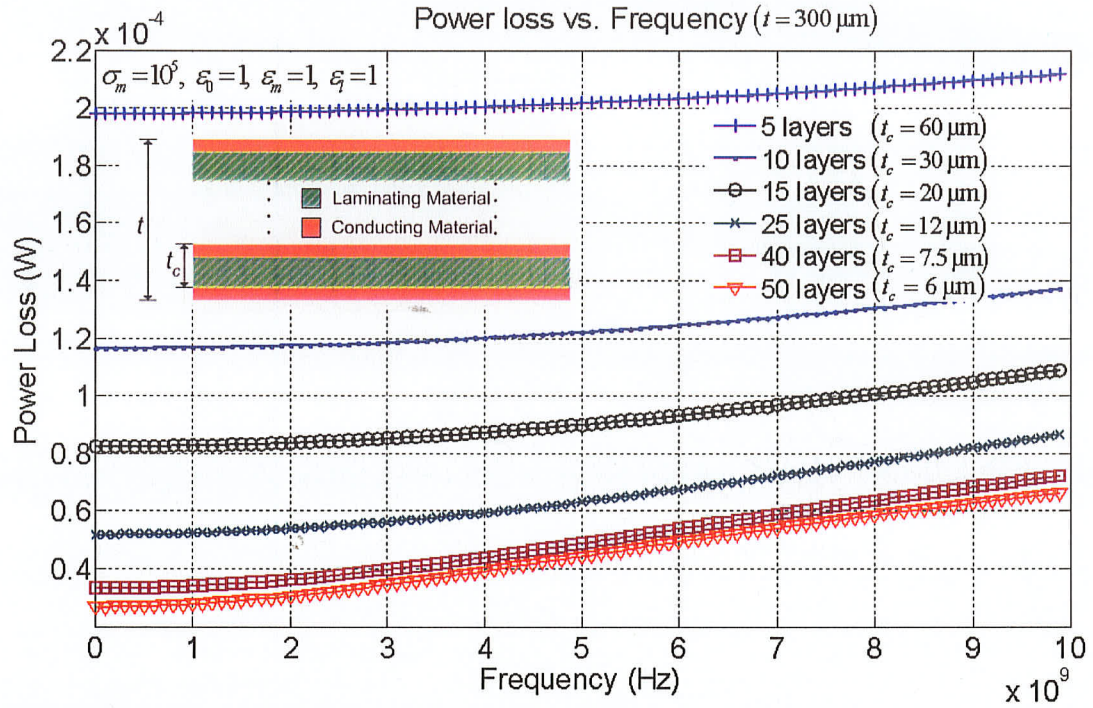


Fig. 6.9: Loss reduction due to the use of many laminated conductor layers with smaller thickness of each layer: $\sigma_m = 10^5$, $t = 300 \mu\text{m}$. Skin depth at 1 GHz is $50.3 \mu\text{m}$ for $\sigma_m = 10^5$.

6.3 Multi-layered patches to enhance miniaturized antenna gain

As mentioned earlier, when width of the square ring is narrow, the variation of current on the ring becomes very large, and causes excessive ohmic losses, which reduces the antenna gain. To overcome this problem, we applied the concept of multiple laminated conductors to some miniaturized antennas in this section. Although microstrip antennas consist of patch conductor and ground conductor, laminated conductors are used

only for the patch conductor, and the ground conductor is assumed infinite to simplify the computer simulation in Ansoft Designer, Version 3.

6.3.1 Square ring antenna

Consider the simple geometry of the microstrip square ring antenna with a narrow width, as shown in Fig. 6.10. The size of the ring is $L_1 = 60$ mm, with width $W = 5$ mm, i.e. $L_2/L_1 = 0.84$, which operates at 1.41 GHz on a foam substrate having thickness $h = 1$ mm. We have used multiple thin laminated conductor layers (as depicted in Fig. 6.11) rather than a single conductor. Table 6.1 shows that for a single copper conductor having an infinitesimal thickness, the gain of the antenna is 4.56 dBi [76, 77].

When multiple laminated conductor layers are used to form the square ring, a significant improvement in the gain is observed, as indicated in the simulation results in Table 6.1 and Fig. 6.12. An infinitesimal thickness of copper is used in the simulation obtained from Ansoft Designer, version 3. To better understand the effects of having multiple laminated conductor layers, air gaps are used between conductor layers instead of dielectrics. Each laminated conductor has a conductor layer with infinitesimal thickness, and an air gap with $1\text{ }\mu\text{m}$ thickness. The thickness of each laminated conductor layer (t_c) is around the skin depth. For 6 layers, with overall thickness (t) of $6\text{ }\mu\text{m}$, the antenna gain is 6.92 dBi, 2.36 dB higher than that of the single conductor case. When air gap (t_l) is $3\text{ }\mu\text{m}$, a peak gain of 8.84 dBi is observed for 4 layers having an overall thickness of $12\text{ }\mu\text{m}$. This

indicates an increase in the gain of 4.28 dB, compared to a single layer case, as shown in Fig. 6.13.

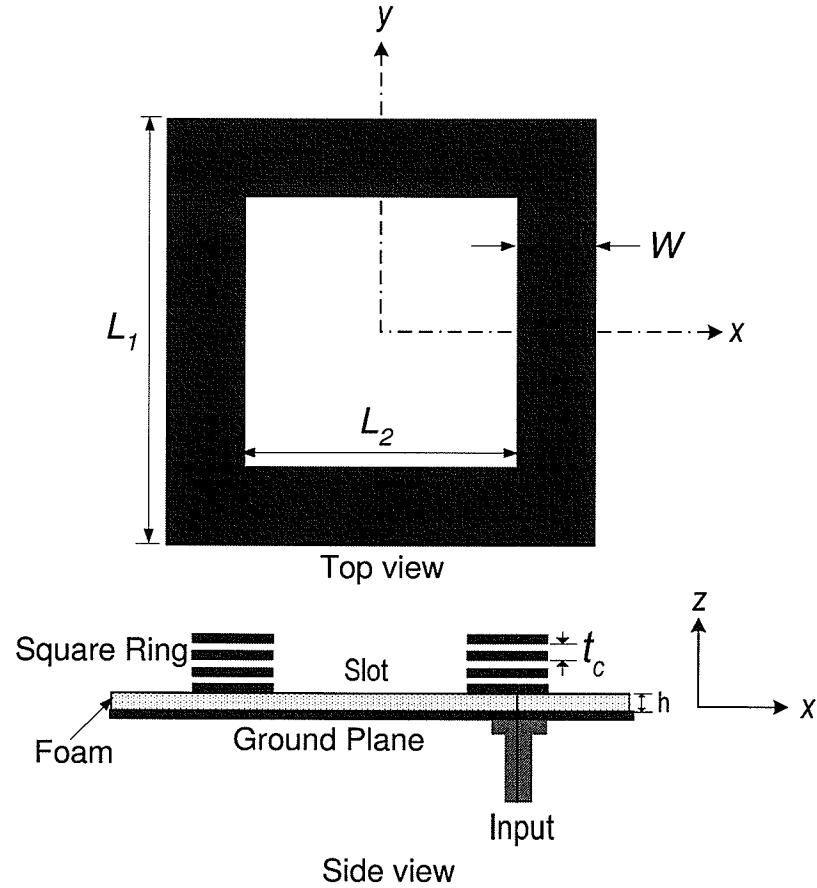


Fig. 6.10: Geometry of the square-ring antenna on foam substrate: (a) top view, (b) side view. Antenna parameters: $L_1 = 60$ mm, $W = 5$ mm, $L_2 = 50$, $h = 1$ mm.

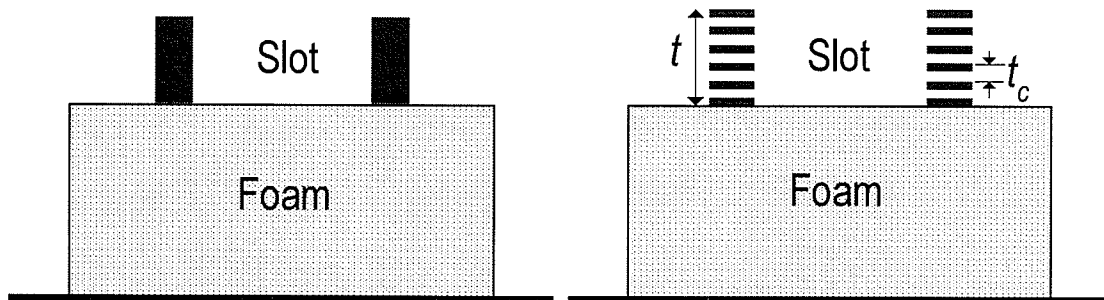


Fig. 6.11: Side view of a square ring antenna on a foam substrate, (a) with a single solid conductor, (b) with multiple thin laminated conductor layers.

Table 6.1: Multiple laminated conductor layers to enhance the gain of the square ring antenna in Fig. 6.10 with $t_c = 1 \mu\text{m}$

Number of laminated conductor layers	Overall conductor thickness t (μm)	Peak accepted gain (dBi)
Single conductor	Infinitesimal	4.56
1	1	4.81
2	2	5.81
3	3	6.09
4	4	6.52
5	5	6.92
6	6	6.69
7	7	6.66
8	8	6.43
9	9	6.25

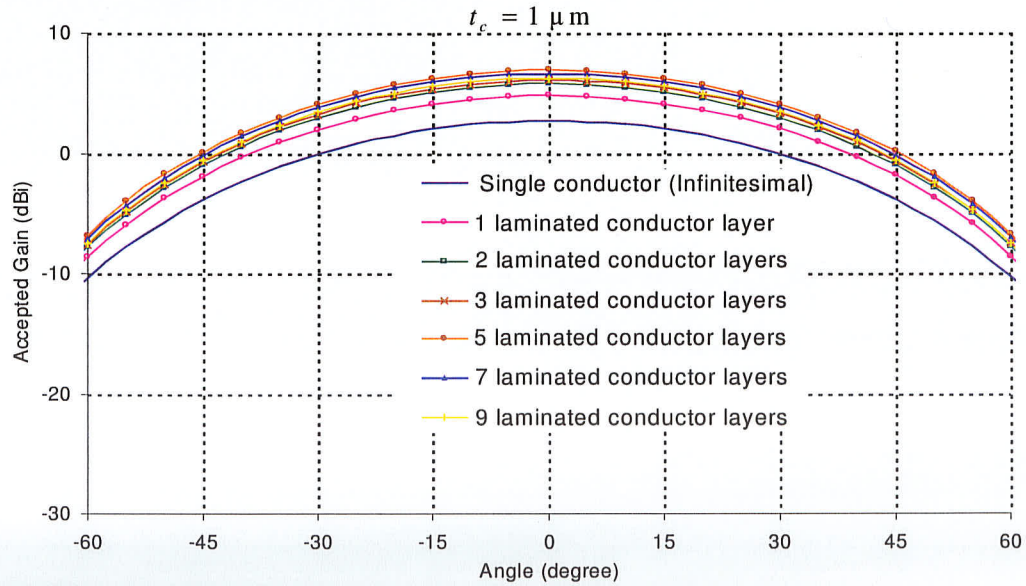


Fig. 6.12: Variations of the gain of the ring antenna in Fig. 6.10 for multiple laminated conductor layers at 1.41 GHz in the $\phi = 0^\circ$ plane: $t_c = 1 \mu\text{m}$.

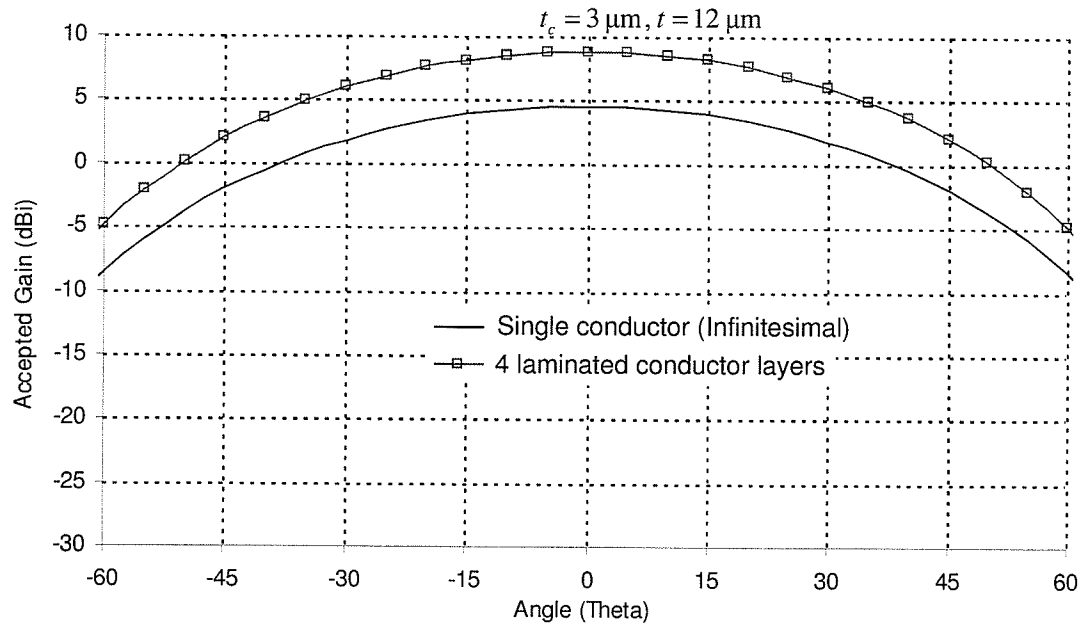


Fig. 6.13: Variations of the gain of the ring antenna in Fig. 6.10 for multiple laminated conductor layers at 1.41 GHz in the $\phi = 0^\circ$ plane: $t_c = 3 \mu\text{m}$.

The square ring antenna, discussed above, has no dielectric loss, since foam layer is considered as the substrate. Let us consider another miniaturized microstrip antenna, H-shaped microstrip antenna, which has dielectric loss, and use multiple laminated conductors to see whether gain can be improved.

6.3.2 H-shaped miniaturized antenna

Geometry of the H-shaped microstrip antenna is shown in Fig. 6.14. Like the ring antenna, its gain reduces due to increased losses caused by the miniaturization. This

geometry is selected here to find the generality of the technique. The antenna is on a microwave substrate having relative permittivity, $\epsilon_r = 2.5$, loss tangent, $\tan \delta = 0.0019$ and thickness = 1.6 mm. The antenna is operating at 2 GHz [78]. The antenna has both conductor and dielectric losses (5.04 dB), with the later one dominating the loss (1.47 dB), as shown in Fig. 6.15. When multiple laminated conductors are used for this antenna, the gain remains nearly 3.69 dBi, indicating no significant gain improvement, as shown in Fig. 6.16. This discussion suggests that the use of several laminated conductor layers cannot reduce the dielectric loss, and can only improve the gain when conductor loss is the dominant cause of losses.

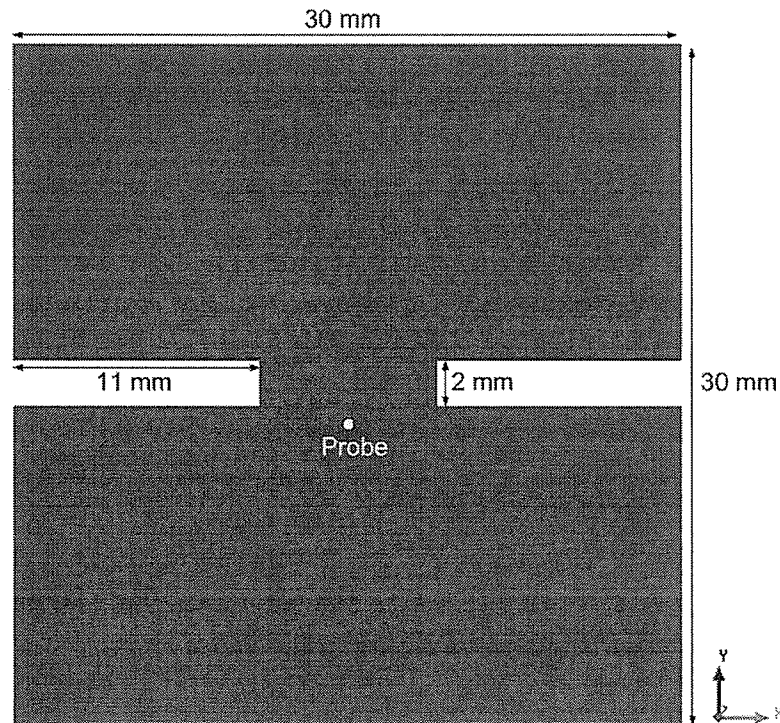


Fig. 6.14: Geometry of the H-shaped microstrip antenna, on a substrate having $\epsilon_r = 2.5$, $\tan \delta = 0.0019$ and $h_2 = 1.6$ mm, with antenna dimensions.

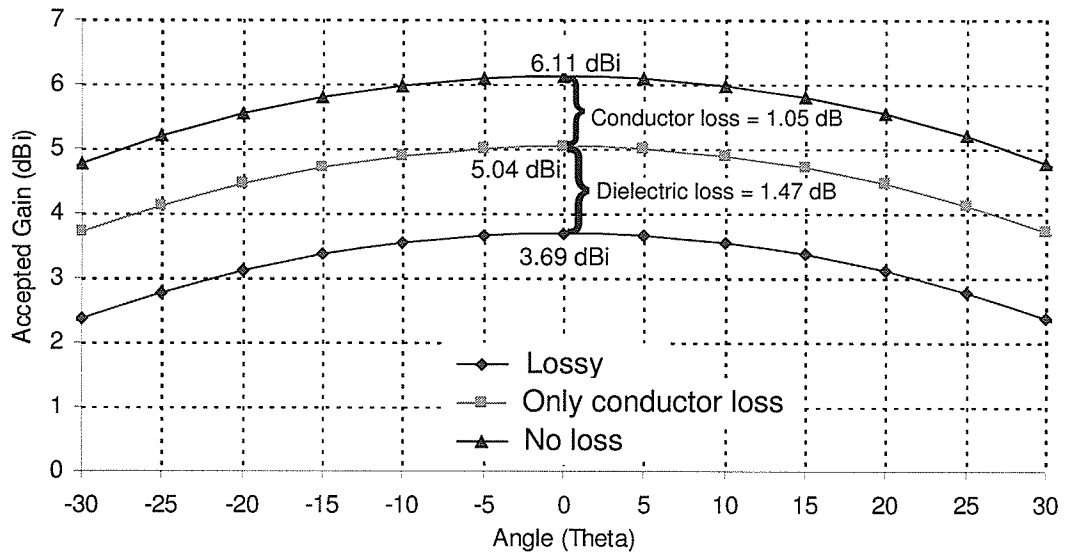


Fig. 6.15: Gain patterns, in $\phi = 0^\circ$ plane, of the H-shaped antenna in Fig. 6.14 at 2 GHz, in order to calculate the conductor and dielectric losses.

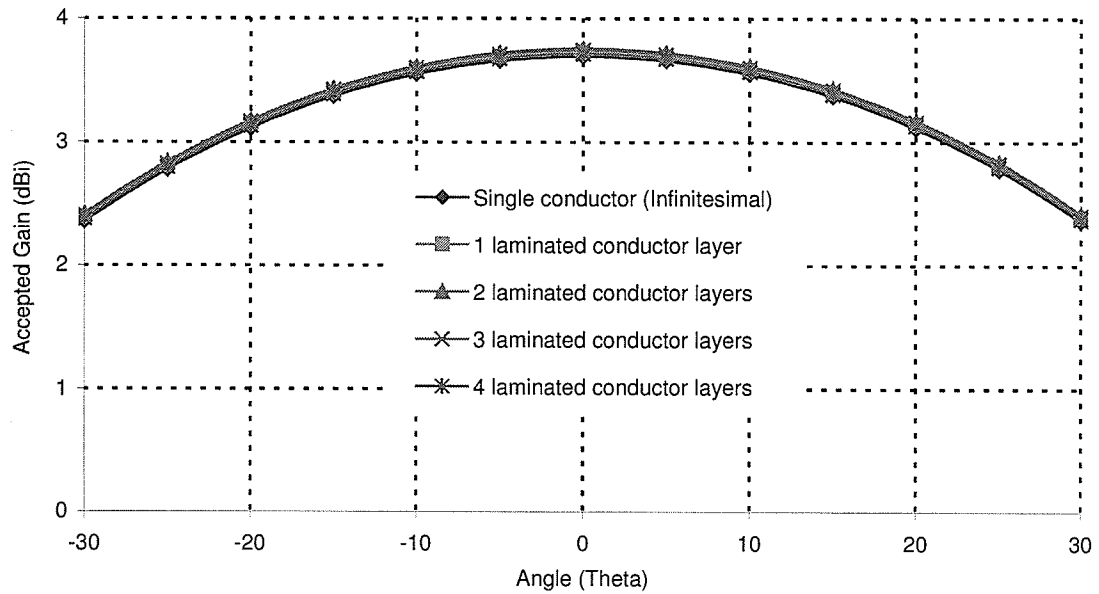


Fig. 6.16: Gain patterns, in $\phi = 0^\circ$ plane, of the H-shaped antenna in Fig. 6.14 at 2 GHz, with multiple laminated conductor with $t_c = 0.5 \mu\text{m}$.

6.3.3 Miniaturized loaded square ring antenna

Now we consider another miniaturized antenna, the capacitively-fed modified loaded square ring microstrip antenna, as discussed in section 5.7 in the previous chapter. It was mentioned earlier that this antenna is a miniaturized antenna to a greater extent. Moreover, it has a poor gain. More detail geometry of the antenna is presented in Fig. 6.17. The antenna is on a dielectric substrate with $\epsilon_r = 2.5$, thickness = 0.79 mm, and $\tan\delta = 0.0019$, which is separated from the ground plane by a foam of thickness 6.35 mm. From Fig. 6.18, we can see that its conductor loss is the dominant factor of the total loss of 4.48 dB. For the single conductor (infinitesimal thickness) case, its gain is 1.52 dBi. However, when several laminated conductors are used, its gain increases, as shown in Fig. 6.19. For 3 layers, its gain is 2.88 dBi, with an air gap of $0.5 \mu\text{m}$, and overall conductor thickness, $t = 1.5 \mu\text{m}$, as mentioned in Table 6.2. A very small shifting of the operating frequency is observed when more number of layers is used.

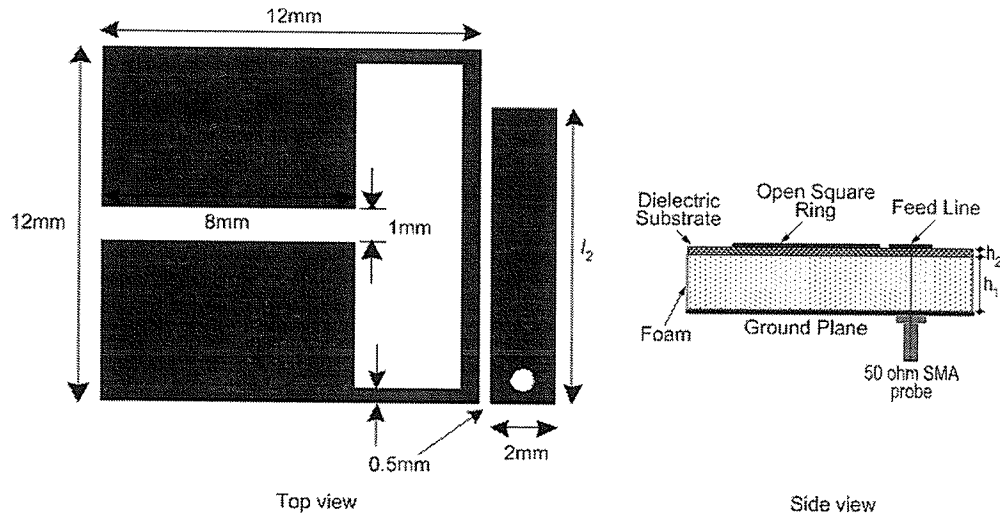


Fig. 6.17: Geometry of the modified loaded square ring antenna, on a substrate having $\epsilon_r = 2.5$, thickness = 0.79 mm, and $\tan\delta = 0.0019$.

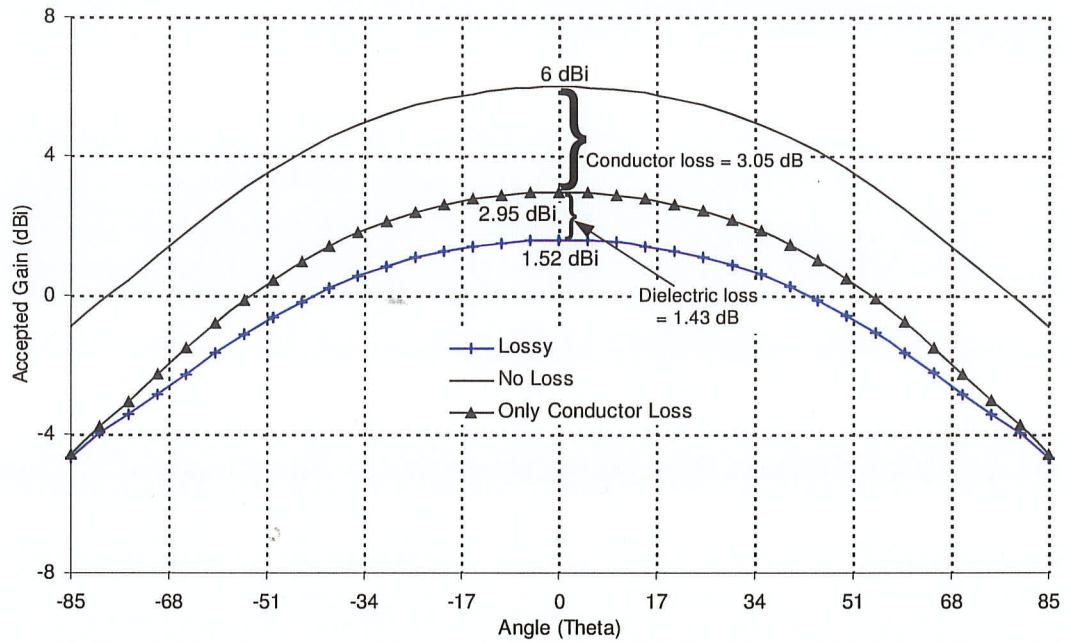


Fig. 6.18: Gain patterns at 2.185 GHz, in the $\phi = 0^\circ$ plane, of the modified square ring antenna in Fig. 6.17, in order to calculate the conductor and dielectric losses.

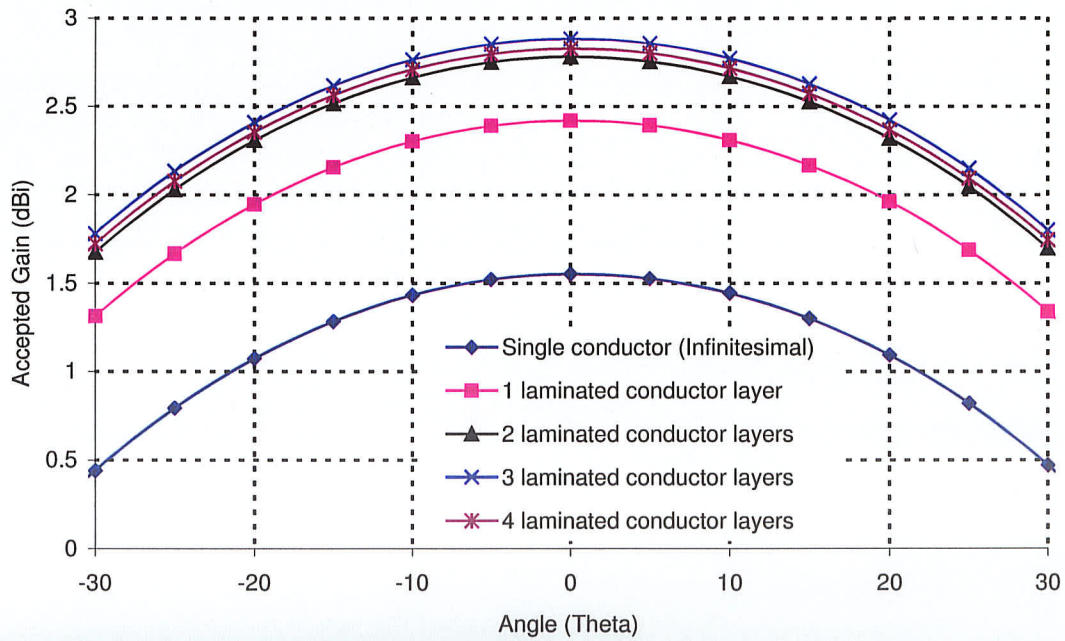


Fig. 6.19: Variations of the gain at 2.185 GHz of the multi-layered modified loaded square ring antenna in Fig. 6.17, in the $\phi = 0^\circ$ plane: $t_c = 0.5 \mu\text{m}$.

Table 6.2: Effects of multiple laminated conductor layers on the gain of the modified loaded square ring antenna in Fig. 6.17: $t_c = 0.5 \mu\text{m}$

Number of Laminated conductor layers	Overall conductor thickness t (μm)	Peak accepted gain (at 2.22 GHz) (dBi)
Single conductor	Infinitesimal	1.52
1	0.5	2.42
2	1	2.78
3	1.5	2.88
4	2	2.83

It is important to mention here that when perfect electric conductor (PEC) is considered as the infinitesimal conductor layers, the gain improvement cannot be achieved, as can be noticed in Fig. 6.20. With multiple laminated conductors with PEC, the accepted gain stays at 3.65 dBi as shown in Figs. 6.20 (a), (c) and (e). Apparently, the beamwidth, in each case, does not change with increasing number of layers. For these cases, when copper is considered as the conducting material, the conductor loss occurs, which is mentioned in those figures. It is evident that with increasing number of layers, the copper loss is reduced. For each case, when copper loss is added to its accepted gain, the curve overlaps with its accepted gain obtained considering PEC. This suggests that the gain improvement is due to the reduction in the ohmic loss because of the use of multiple laminated conductors.

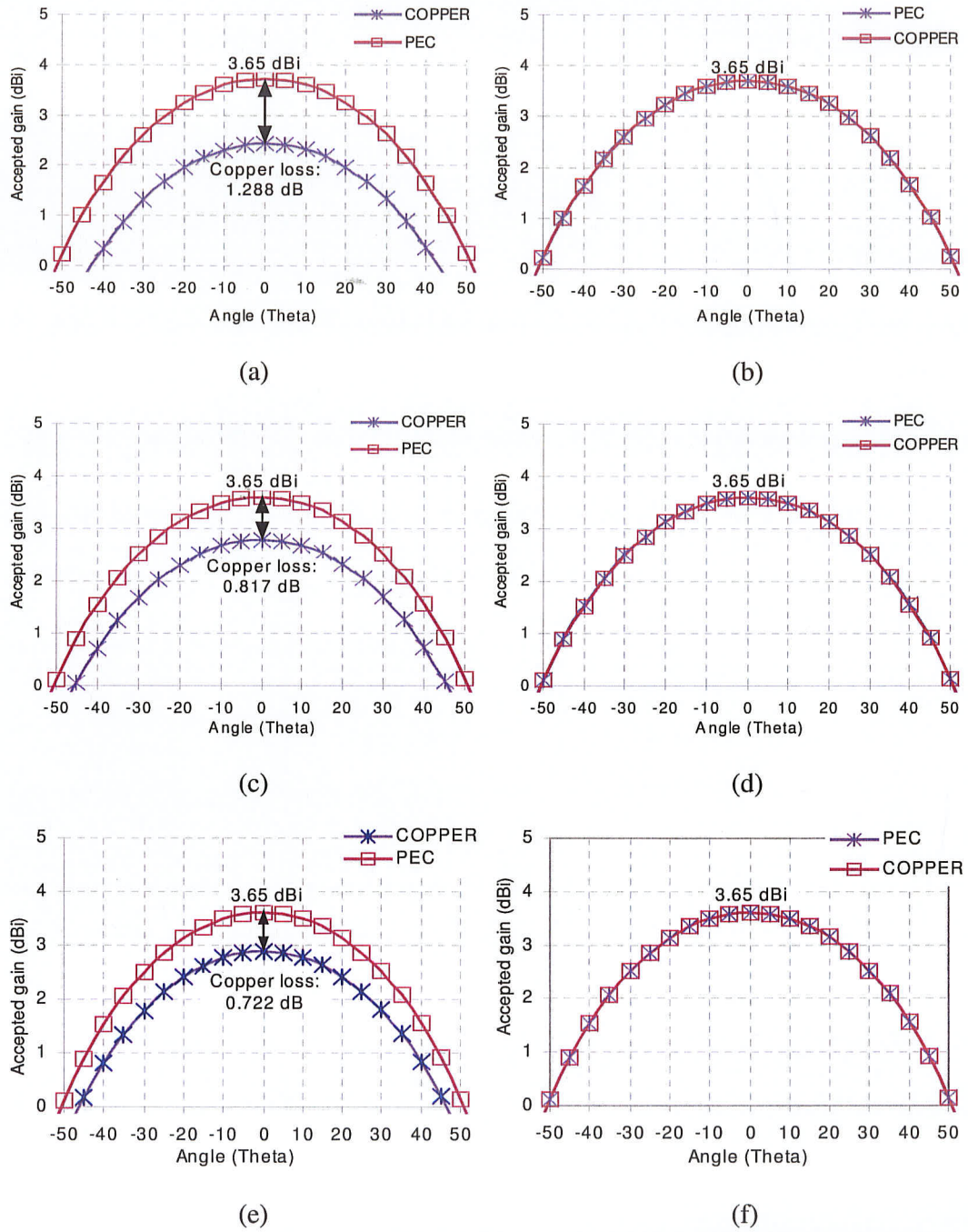


Fig. 6.20: Variations of the gain, at 2.185 GHz in the $\phi = 0^\circ$ plane, of the ring antenna for multiple laminated conductor layers, with perfect electric conductor (PEC) and copper conductor: $t_c = 0.5 \mu\text{m}$. (a) 2 layers, (c) 3 layers and (e) 4 layers showing ohmic losses, and (b) 2 layers, (d) 3 layers and (f) 4 layers, with copper losses added to the gain.

6.4 Choice of laminating dielectric material

In order to be able to fabricate the antenna, air as the laminating dielectric material is not suitable. Therefore, effects of using different dielectric permittivities and thicknesses are studied for the miniaturized antenna discussed in Section 6.3.2. First, for the case with two layers with air as the laminating dielectric material, the thickness of each laminating material (t_l) is varied. Fig. 6.21 shows the effect of varying t_l on the return loss plot of the antenna. For very small thicknesses, the frequency for minimum S_{11} does not change much. However, as the thickness is increased, the frequency for minimum S_{11} moves to the higher frequencies. Fig. 6.22 shows the variation in the gain of the antenna when t_l is varied. With larger t_l , the gain of the antenna increases as indicated in Table 6.3. The gain is recorded at the frequency of minimum S_{11} .

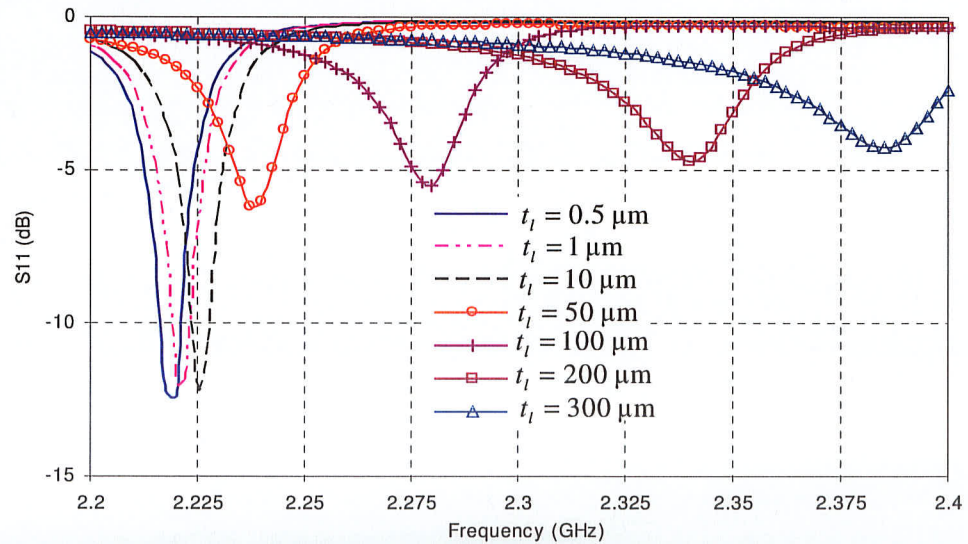


Fig. 6.21: Variation on the return loss of the modified loaded square ring antenna with multiple laminated conductor layers, in Fig. 6.17, with different laminating dielectric material thickness, t_l . $\epsilon_r = 1$.

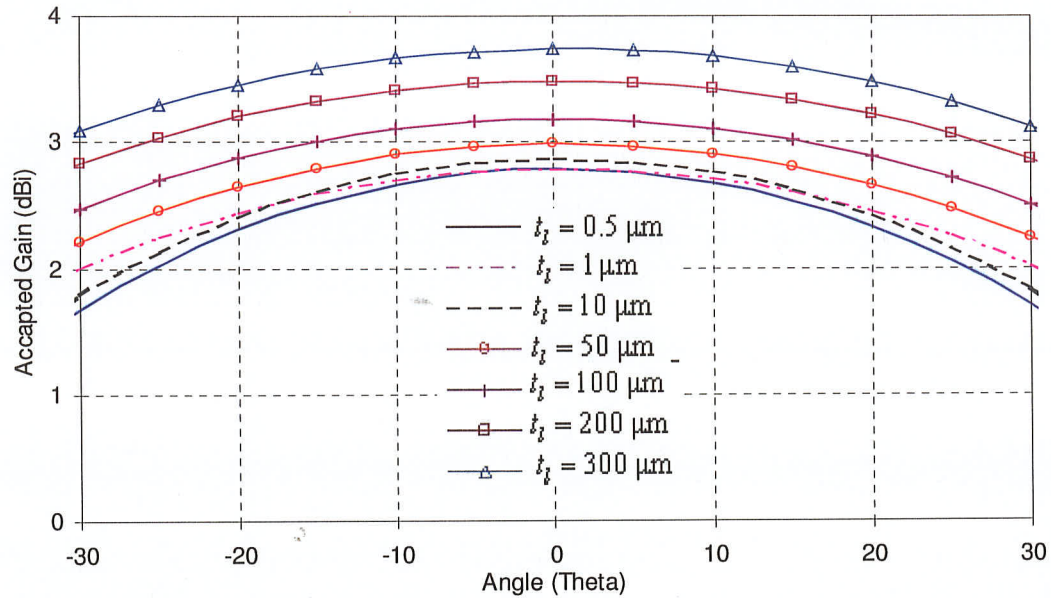


Fig. 6.22: Variation on the gain of the modified loaded square ring antenna with multiple laminated conductor layers, in Fig. 6.17, with different laminating dielectric material thickness, t_l . $\epsilon_r = 1$.

Table 6.3: Laminated conductor thickness and the gain of the modified loaded square ring antenna in Fig. 6.17 for two-layer case with different laminating dielectric thickness t_l

Laminating dielectric thickness t_l (μm)	Overall conductor thickness t (μm)	Frequency for minimum S_{11} (GHz)	Minimum S_{11} value (dB)	Peak accepted gain (dBi)
0.5	1	2.222	-13.5	2.78
1	2	2.224	-13.2	2.79
10	20	2.225	-13.4	2.87
50	100	2.24	-6.24	2.98
100	200	2.28	-5.53	3.18
200	400	2.3425	-4.8	3.48
300	600	2.39	-4.3	3.74

Next, for a fixed value of t_l (100 μm) and two laminated conductor layers, permittivity of the laminating dielectric (ϵ_l) is changed. As the value of ϵ_l increases, the frequency for minimum S_{11} shifts to the lower frequencies. The S_{11} value does not change much with this change in permittivity, as shown in Fig. 6.23. However, the gain drops as the permittivity of the laminating dielectric is increased, as shown in Fig. 6.24 and Table 6.4. Again, the gain is recorded at the frequency of minimum S_{11} . This discussion suggests that to achieve the optimum gain, $\epsilon_l = 1$ is the best material, and thickness of the laminating layer can be chosen based on the application. Even with a thin laminating layer thickness, significant gain enhancement can be achieved.

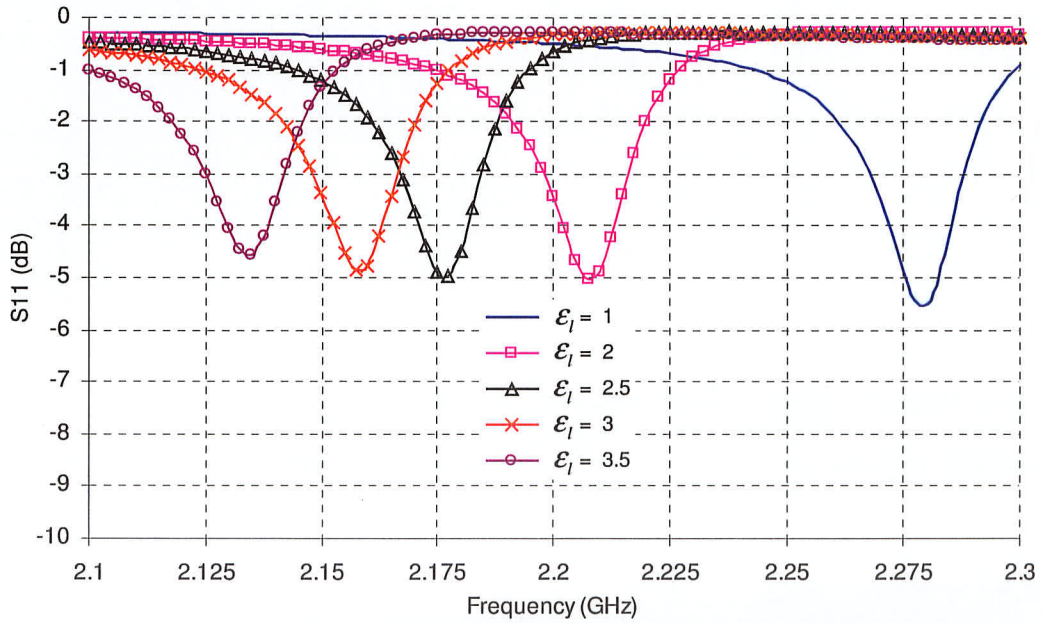


Fig. 6.23: Variation on the return loss of the modified loaded square ring antenna with multiple laminated conductor layers, in Fig. 6.17, with different laminating dielectric materials (varying ϵ_l). $t_l = 100 \mu\text{m}$.

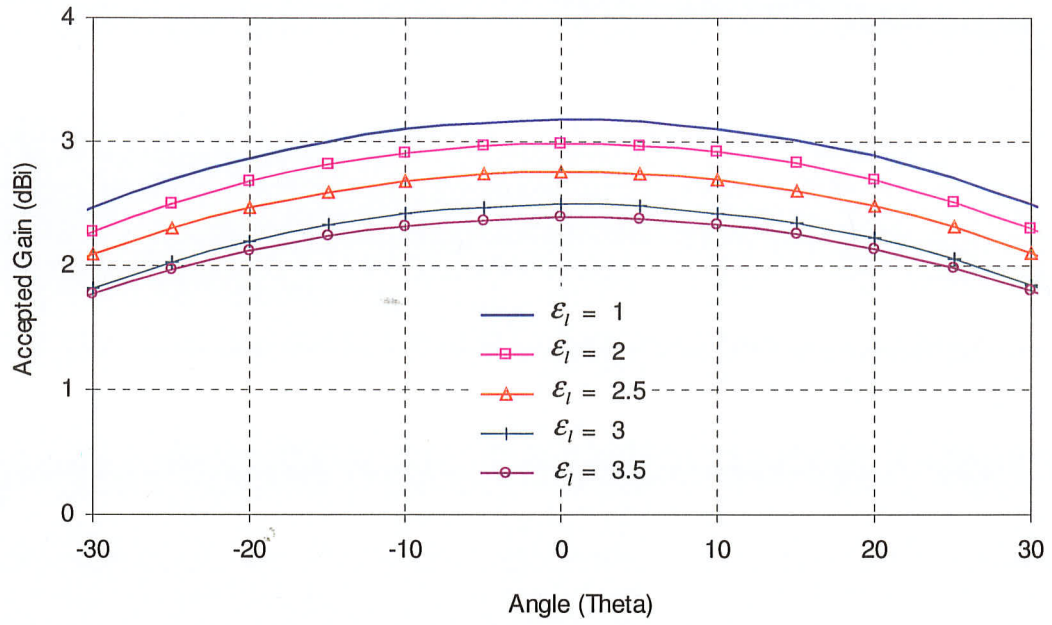


Fig. 6.24: Variation on the gains of the modified loaded square ring antenna with multiple laminated conductor layers, in Fig. 6.17, with different laminating dielectric materials (ϵ_l). $t_l = 100 \mu\text{m}$.

Table 6.4: Laminated conductor thickness and the gain of the modified loaded square ring antenna in Fig. 6.17 for two-layer case with different laminating dielectric material (varying ϵ_l). $t_l = 100 \mu\text{m}$ and $t = 200 \mu\text{m}$.

Laminating dielectric permittivity (ϵ_l)	Frequency for minimum S_{II} (GHz)	Minimum S_{II} value (dB)	Peak accepted gain (dBi)
1	2.28	-5.53	3.18
2	2.21	-5	2.99
2.5	2.175	-4.98	2.76
3	2.16	-4.88	2.50
3.5	2.135	-4.57	2.39

6.5 Experimental study

In order to verify the gain enhancement technique presented in previous sections, attempts have been made to fabricate a miniaturized antenna with several laminated conductors. To avoid sophisticated and expensive micro-fabrication to have thin laminating dielectric layer thickness, a commercially available low-loss substrate material, RT/Duroid 5880, is used as laminating dielectric. Its permittivity (ϵ_r) is 2.2, thickness is 254 μm , and loss tangent is only 0.0009.

Simulated return loss plot of the antenna in Fig. 6.17, with multiple laminated conductor, using RT/Duroid 5880 material as the laminating dielectric is shown in Fig. 6.25. As the number of layers increases from 1 to 3 the frequency for minimum S_{11} goes to lower frequencies. It is necessary to mention here that when the thickness of each laminated conductor layer is very small, this shifting is negligible. The S_{11} values become worse with the increased number of layers, which indicates poor impedance match. The matching can be easily improved by changing the length of the capacitive feed line.

In the case of gain, accepted gain, at the frequency of minimum S_{11} , increases as the number of layers increases, as expected, Fig. 6.26, with 2.69 dBi gain for the case of 3 layers. The antenna with 1, 2, and 3 layers, using the same substrate, was fabricated in the antenna laboratory and the machine shop at the University of Manitoba.

Measured return loss plots of four cases are shown in Fig. 6.27. As the simulated case, the frequency for minimum S_{11} goes also to the lower frequency for the measured

antenna. However, in the measured case, the amount of shifting in the frequency is larger compared to the simulated ones.

In the case of gain, we can see the enhancement in measured gain due to the increase in number of layers. Here also, the gain is measured at the frequency of minimum S_{11} . However, due to the mismatch loss, as can be seen in Fig. 6.26, the gain is not as high as the simulated ones. It is necessary to mention here that due to mismatch loss, the gain drops. A table is attached in Appendix E to quantify the reduction in antenna gain due to mismatch loss. If we take into account the gain drop due to mismatch loss, the measured gain agrees well with the simulated ones, as shown in Table 6.5.

The peak of the gain did not occur along boresight (at $\theta = 0^\circ$), may be due to the misalignment of the antenna with respect to the reference antenna. Moreover, multiple layers are glued to each other by hand, which can also cause misalignment of the layers. The laminating dielectric material was not rigid, which could cause a non-uniformity in the layers. These could be reasons for discrepancy between the simulated and measured return losses and gains. Considering these practical issues and complexity of the structure, it can be concluded that the measured results are in good agreement with the simulated ones.

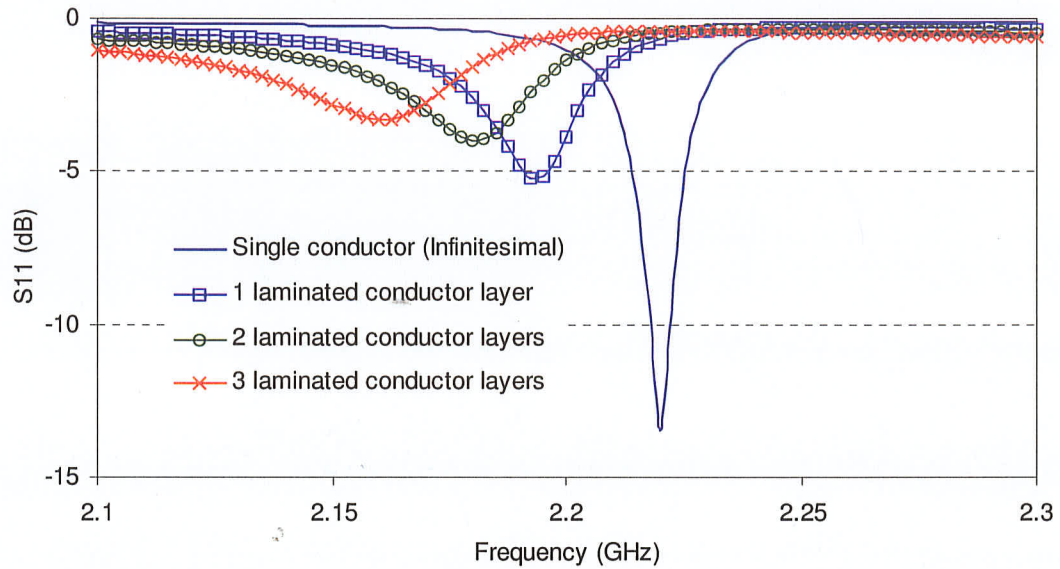


Fig. 6.25: Simulated return loss plots of the modified loaded square ring antenna with multiple laminated conductor layers, in Fig. 6.17, with RT/Duroid 5880 as the laminating dielectric: thickness = 254 μm , relative permittivity = 2.2, and $\tan\delta = 0.0009$.

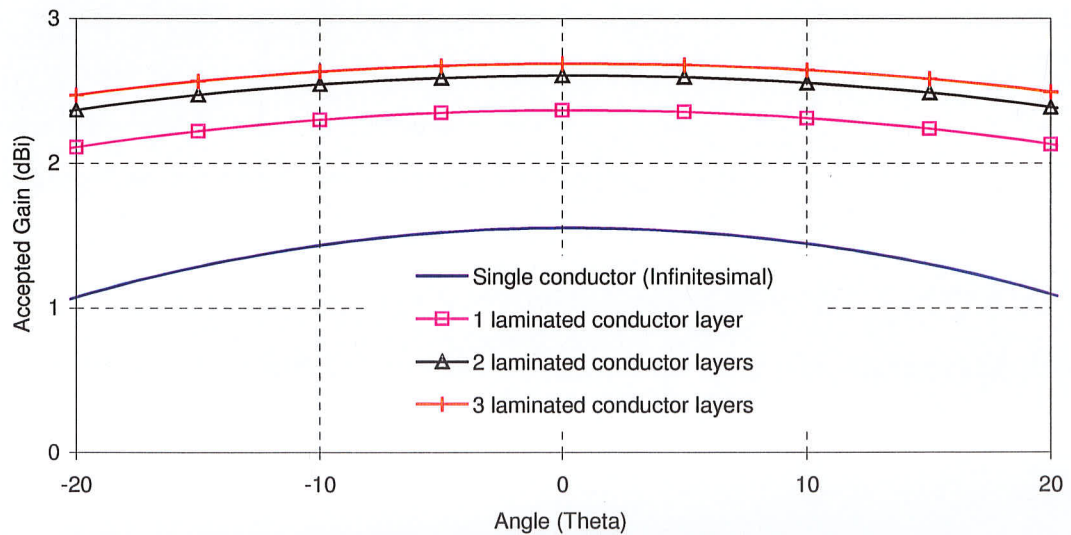


Fig. 6.26: Simulated gain patterns of the modified loaded square ring antenna with multiple laminated conductor layers, in Fig. 6.17, with RT/Duroid 5880 as the laminating dielectric: thickness = 254 μm , relative permittivity = 2.2, and $\tan\delta = 0.0009$.

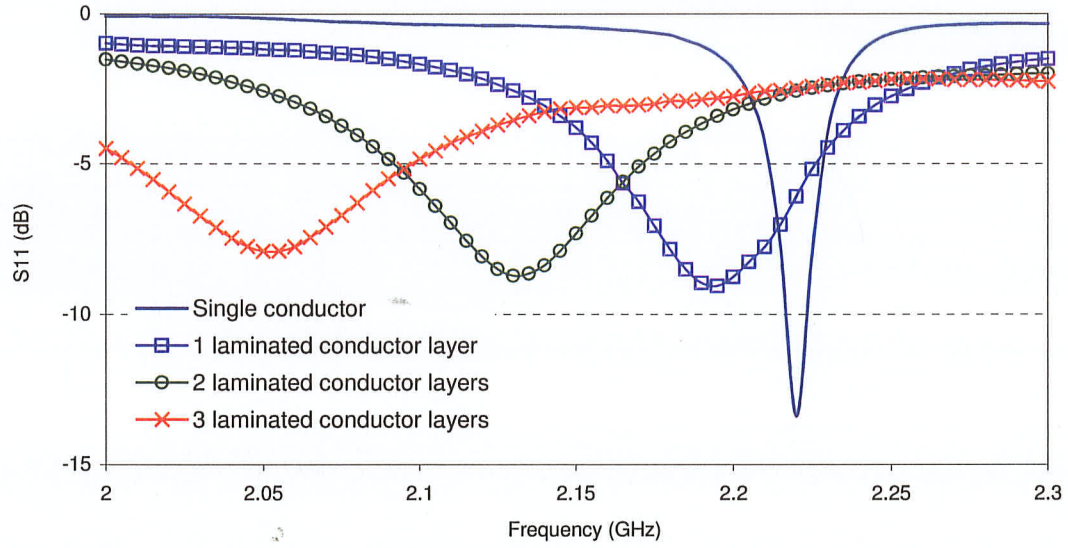


Fig. 6.27: Measured return losses of the modified loaded square ring antenna with multiple laminated conductor layers, in Fig. 6.17, with RT/Duroid 5880 as the laminating dielectric: thickness = 254 μm , relative permittivity = 2.2, and $\tan\delta = 0.0009$.

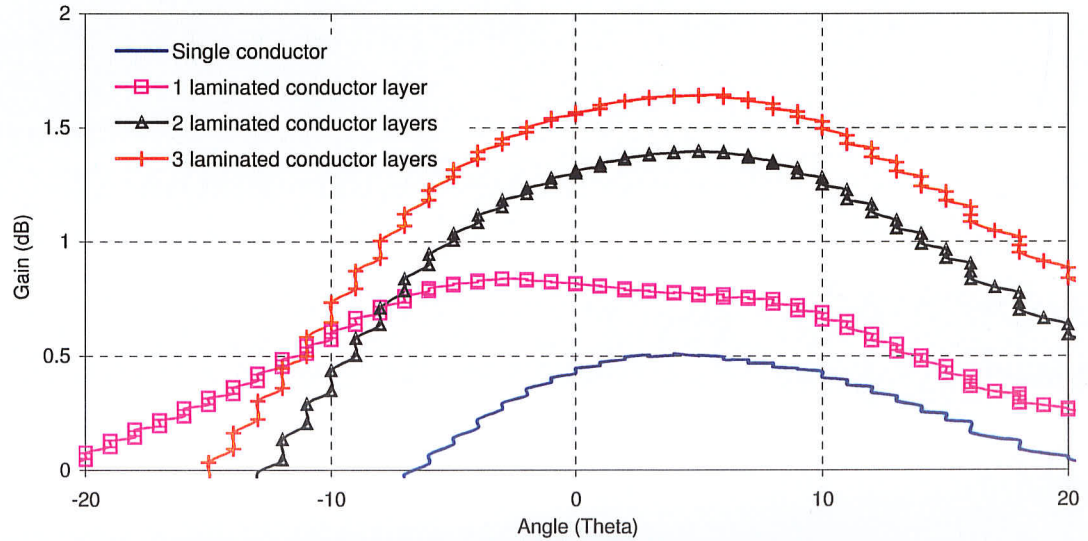


Fig. 6.28: Measured gain patterns of the modified loaded square ring antenna with multiple laminated conductor layers, in Fig. 6.17, with RT/Duroid 5880 as the laminating dielectric: thickness = 254 μm , relative permittivity = 2.2, and $\tan\delta = 0.0009$.

Table 6.5: Simulated and measured return losses and gains of the modified loaded square ring antenna in Fig. 6.17, using multiple laminated conductors. Laminating dielectric:

RT/Duroid 5880: $t_c = 254 \mu\text{m}$, $\epsilon_r = 2.2$, and $\tan\delta = 0.0009$.

Number of laminated conductor layers	Overall conductor thickness t (μm)	Simulated		Measured		
		Frequency for minimum S_{11} (GHz)/ Value (dB)	Peak accepted gain (dBi)	Frequency for minimum S_{11} (GHz)/ Value (dB)	Peak gain (dBi)	Peak accepted gain (dBi)
Single conductor	Infinitesimal	2.221 (-13.5)	1.52	2.22 (-13.38)	0.51	0.51
1	254	2.1925 (-5.2)	2.51	2.195 (-9.05)	0.84	1.34
2	508	2.1825 (-4)	2.61	2.1325 (-8.7)	1.39	2.51
3	762	2.165 (-3.3)	2.69	2.055 (-7.9)	1.64	2.67

6.6 Conclusion

A unique gain enhancement technique is presented in this chapter to increase the gain of miniaturized microstrip square ring antennas. The main idea here is to reduce the ohmic loss by introducing several laminating conducting layers, instead of a single conductor. In the case of a planar conductor, it has been shown that when several laminating conductor layers are used, the power lost in the conductor is less compared to

a single conducting material. When more number of layers are used, the reduction in the loss is more, however, with a few number of layers, a significant loss reduction occurs.

The method is applied to microstrip ring antennas, which consist of the patch conductor and ground conductor. It was found that when the conductor loss is the dominant source of the loss in microstrip ring antennas, the antenna gain could be increased by using several laminated conducting layers, which essentially reduces the ohmic loss of these antennas.

Although laminating materials with $\epsilon_r = 1$ and very thin thickness are sufficient to substantially increase the gain, for the ease of fabrication, we used low-loss thicker laminating material with $\epsilon_r = 2.2$ to fabricate a miniaturized antenna with several laminated conducting layers. The simulated and measured results are in good agreement, taking into consideration the practical issues and complexity of the structure.

CHAPTER SEVEN

Conclusion

7.1 Summary

In this thesis, microstrip square ring antenna was investigated on the basis of wideband and multi-band operation, polarization, and loss reduction. Microstrip ring antennas are miniaturized antennas, and come with typical problems of small antennas, such as narrow impedance bandwidth, polarization impurity and poor gain. Research was carried out to overcome these problems, and methods that were developed during the research to address these problems were presented in this thesis.

At first, different antenna miniaturization techniques were discussed, along with a brief review on microstrip ring antennas, or more specifically, microstrip square ring antennas. General disadvantages of square ring antennas were mentioned. Narrow bandwidth is one of those disadvantages, and when it comes to the case of circularly polarized square ring antennas with a single feed, the problem is even more severe. However, several corner-perturbed dual-layer square ring antennas were designed with wider axial ratio bandwidths. As the corner perturbation, both negative and positive perturbations were successfully used on both parasitic and driven rings to widen the axial ratio bandwidth.

One unique case was the hybrid perturbation scheme, where the driven ring was negatively perturbed, and the parasitic ring was positively perturbed. The locations of the perturbations were chosen using the concept of sequential rotation so that the stacked configuration generated circular polarization. One important advantage of this design was its capability of covering wider angular region in the upper hemisphere.

The effects of having finite ground plane were also studied, where it was shown that having symmetric ground plane is an important issue in the case of circularly polarized stacked square ring antennas. Moreover, it was mentioned that smaller ground planes degrade the CP performance of the antenna, which can be improved again by changing ring sizes and the ring separation. The simulated results were confirmed by comparing them with the measurement results, obtained after testing several corner-perturbed stacked square ring antennas, fabricated at the Antenna Laboratory at the University of Manitoba.

Study was carried out to obtain multi-band operation from stacked square ring antenna, as it allows accommodating more resonators inside the square rings. It is obvious that these resonators will resonate at much higher frequencies than those of the stacked rings. Feeding three rings, to operate them in three frequencies, was the main challenge in this case. Capacitive feedings were chosen for both bottom ring and the ring inside the top ring. The bottom ring, excited using an outside feed line, works as the excitation for the top outer ring. An inside capacitive feed line was chosen for the top inner ring. Moreover, the capacitive feeding allows us to have rings with narrower widths, thus making it easier to accommodate another ring inside the top ring. Circular

polarization was achieved from this antenna by using two feed lines for the bottom ring, and two feed lines for the top inner ring, exciting one with 90° phase shift with respect to the other on the same layer.

A specific application of such a design is in the modernized global positioning system, where three bands, L5, L2 and L1, are to be covered. The antenna with three rings was optimized to cover these three GPS frequencies with circular polarization. The antenna has advantages in terms of overall height and size over other designs, available in the open literature for the tri-band GPS application. In this case, the results were confirmed by simulating the antennas using two commercial software: Ansoft Designer, version 3 and Ansoft HFSS, version 10.

Multi-band operation can also be achieved from square ring antenna when it is loaded with a small gap or slit. It was shown that due to the loading, two other modes, called loaded modes, are excited around the TM_{11} or unloaded mode frequency of the square ring, when an asymmetric feed location was chosen. The polarization of each of these modes can be altered by introducing the gap either on the horizontal arm or on the vertical arm. A parametric study was conducted to understand the nature of the loaded modes, and to establish a relationship among these loaded and unloaded mode frequencies.

In fact, by loading, we obtain a miniaturized antenna, as the first loaded mode frequency is much lower than the frequency of the conventional square patch. Some other modified loaded square ring antennas were also discussed, where the slot inside

the square ring was modified for further miniaturization. The probe-feed was not capable of providing 50-ohm impedance match for these antennas. Therefore, a capacitive feeding was selected. However, these miniaturized antennas suffer from serious gain problem, as the miniaturization leads to the high ohmic loss. These results were also confirmed by comparing simulated and measured results.

A method was presented to reduce ohmic losses in miniaturized microstrip square ring antennas, where several laminated conductor layers were used, instead of just one conducting layer. It was shown analytically that when multiple laminated conducting layers are used for a planar conductor, the power lost in it is much less compared to that with a single conducting layer. When the thickness of each layer is much smaller than the skin depth of the conducting material, and the number of layers is greater, the amount of loss reduction increases.

In case of modified loaded square ring antenna, when several layers of laminated conductor layers were used, a significant improvement in the gain was observed, compared to the single conducting layer case. In order to avoid expensive micro-fabrication methods, a thicker dielectric material was chosen as the laminating dielectric. The fabricated results matched well with the simulated ones.

7.2 Future research

There are several scopes available for future research. First of all, the thesis deals with microstrip square ring antenna. The study can be extended to annular or elliptical ring antennas to make it more general. Other than that, more specific study can be conducted in particular area:

- In the case of hybrid perturbation method for stacked square rings, the feasibility of using positive perturbations, in the form of stub protruded to the inside slot on the driven ring, should be studied. In fact, different combinations can be studied thoroughly to generalize the concept of hybrid perturbation method.
- In stacked square ring antennas, a third ring was accommodated inside the slot of the top ring. However, another resonator can be inserted on the bottom layer, and the possibility of obtaining quad-band operation can be explored. The feeding will be the big challenge for this case. For circular polarization, designing and accommodating the phase shifters, and providing excitation to four feed lines need further and careful study.

Although it has been shown several times in this thesis that the simulated results obtained from the EM simulator match well with the measured ones, implementation of circularly polarized capacitively-fed antenna with three rings, for practical application, can be a topic of future research.

- For gap-loaded square ring antennas, analytical solution can be sought to have more concrete insight about the loaded mode frequencies.
- Research can be conducted on how one can fabricate patch conductor with thinner laminated conductor layers in order to reduce the ohmic losses, since even with thin layers, significant gain enhancement can be obtained.

Moreover, laminated conductor layers were not considered for the ground conductor, which can be studied in future.

Appendices

Appendix A: Glossary of Important Terms

Gain

IEEE standard definition of gain is: it is the ratio of the radiation intensity in a given direction, to the radiation intensity that would be obtained if the power accepted by the antenna were radiated isotropically. If the direction is not specified, the direction of maximum radiation intensity is implied. The radiation intensity corresponding to the isotropically radiated power is equal to the power accepted by the antenna divided by 4π [80].

$$\text{gain} = 4\pi \frac{\text{radiation intensity}}{\text{total accepted power}} \quad (\text{A1})$$

Gain reference in this thesis is an isotropic antenna with dBi units. An isotropic antenna is an antenna transmitting equal radiation in all directions. It is a hypothetical idealized antenna that does not exist in reality.

Accepted Gain

The IEEE definition of gain does not include mismatch loss. However, in practice, gain is often measured with mismatch loss. In this thesis, the term “Accepted Gain” is the gain without mismatch loss, i.e. the antenna is considered to be completely matched to the input circuit.

If an antenna is without any loss, then in any given direction, its gain is equal to its directivity. In the case of microstrip antennas, the sources of the loss are: conductor loss and dielectric loss.

Circular Polarization and Axial Ratio

According to [80], polarization of an antenna in a given direction is defined as the polarization of the wave transmitted (radiated) by the antenna. When the direction is not stated, the polarization is taken to be the polarization in the direction of maximum gain. Polarization of a radiated wave is the direction of the electric field. Therefore, polarization can be determined by tracing the end point of the arrow representing the instantaneous electric field.

Polarization can be classified as linear, circular and elliptical. If the electric field traces a line, it is called linearly polarized. In general, the electric field traces an ellipse, and the field is called elliptically polarized. Circularly polarized wave is a special case of elliptical polarization, when the ellipse becomes a circle. The electric field that traces a circle or ellipse can be in clockwise or counterclockwise sense. If the rotation of the electric field vector is clockwise, it is designated as right-hand circular polarization (RHCP), and counterclockwise as left-hand circular polarization (LHCP)

Axial ratio is the ratio of the major to minor axes of a polarization ellipse. Axial ratio value of 1 or 0 dB means the perfect circular polarization.

Substrate Permittivity: Dielectric Constant and Effective Dielectric Constant

When any dielectric material is subjected to electric field, the electrical charges in the material tend to polarize in response to the field. Permittivity is a measure of the ability of the material to polarize to the electric field. The electric field is reduced and electric field lines are concentrated inside the material. The relative static permittivity or relative dielectric constant (ϵ_r) is a measure of the extent to which it concentrates electrostatic lines of flux.

Microstrip line or patch antenna has a dielectric substrate in between the ground and the patch. It has air above the patch. The electric fields along the edge undergo fringing, as shown in Fig. A1. In other words, some of the fields are within the dielectric material, and some are in the air. Therefore, an effective dielectric constant (ϵ_{eff}) is necessary to be considered, which will be less than ϵ_r . For small thickness of the dielectric material, the effective dielectric constant is given by [2]:

$$\epsilon_{eff} = \frac{\epsilon_r + 1}{2} + \frac{\epsilon_r - 1}{2} \left(1 + \frac{10h}{L} \right)^{-\frac{1}{2}} \quad (A2)$$

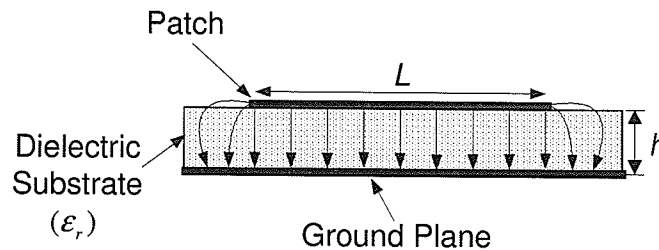


Fig. A1: Microstrip patch antenna on a substrate with fringing electric field lines.

Appendix B: MATLAB code to calculate the power lost in single lossy material with normal incidence of uniform plane wave

```
% The program calculates the coefficients of the electric and magnetic
% fields to find the reflection and transmission of a lossy material
% Program inputs: thickness of the material, frequency range, material
% properties.
```

```
clear all;
clear;
clc
format short
format long e
%-----
-
Sigma = 10^3; % Conductivity of the material

Eps0 = 8.854187818*10^(-12); % Free space permittivity
Muo = 4*pi*10^(-7); % Free space permeability

Epsr1 = 1; Epsr2 = 1; Epsr3 = 1; % Relative permittivities of the three 3
                                % dielectrics
Eps1 = Eps0*Epsr1;
Eps2 = Eps0*Epsr2;
Eps3 = Eps0*Epsr3;
Mur1 = 1; Mur2 = 1; Mur3 = 1; % Relative permeabilities: 3 dielectrics
Mul = Muo*Mur1; Mu2 = Muo*Mur2; Mu3 = Muo*Mur3;

%frequency range
r = 100;
fmax = 10*10^9;
df = fmax/r;
F = (1:df:fmax); %Frequency in Hz

%thickness
d = 1*10^(-8); % thickness of the metal

%Matrix components

for k = 1:length(F)
    f = F(k);

%Propagation factors
    k1 = 2*pi*f*sqrt(Eps1*Mul); % In free-space region
    k2 = 2*pi*f*sqrt(Mu2*Eps2)*sqrt(1-j*Sigma/(2*pi*f*Eps2)); % In the lossy material
    k3 = 2*pi*f*sqrt(Eps3*Mu3); % In the free-space region
%Matrix components
    A11 = -1;
```

```

A12 = 1;
A13 = 1;
A14 = 0;

A21 = k1/(2*pi*f*Mu1);
A22 = k2/(2*pi*f*Mu2);
A23 = -k2/(2*pi*f*Mu2);
A24 = 0;

A31 = 0;
A32 = exp(-j*k2*d);
A33 = exp(j*k2*d);
A34 = -exp(-j*k3*d);

A41 = 0;
A42 = (k2/(2*pi*f*Mu2))*exp(-j*k2*d);
A43 = -(k2/(2*pi*f*Mu2))*exp(j*k2*d);
A44 = -(k3/(2*pi*f*Mu3))*exp(-j*k3*d);

% The matrix
A = [A11, A12, A13, A14;
     A21, A22, A23, A24;
     A31, A32, A33, A34;
     A41, A42, A43, A44];

B11 = 1;
B12 = k1/(2*pi*f*Mu1);
B13 = 0;
B14 = 0;

B = [B11; B12; B13; B14];

C = A\B;
D(k) = C(1);
E(k) = C(4);
end

R = (abs(D)).^2;
T = (abs(E)).^2;

% POWER BALANCE
Power = 1/(2*sqrt(Muo/Eps0)) - R/(2*sqrt(Muo/Eps0)) -
T/(2*sqrt(Muo/Eps0)); %Losses
plot(F, Power, 'o')
grid on
Hold on
title(['Power loss vs. Frequency']);
xlabel('Frequency (Hz)');
ylabel('Power Loss');

```

Appendix C: MATLAB code to calculate the power lost in multiple laminated conducting materials with normal incidence of uniform plane wave

```
% The program calculates the coefficients of the electric and magnetic
% fields to find the reflection and transmission of a planar conductor
% with several laminated conducting material layers.
% Program inputs: thickness of each layer, frequency range, material
% properties.

clear all;
clear;
clc
format short
format long e
%-----
%
Sigma = 10^3; % Conductivity of conducting material

Eps0 = 8.854187818*10^(-12); % Free space permittivity
Muo = 4*pi*10^(-7); % Free space permeability

Epsr1 = 1; Epsr2 = 1; Epsr3 = 1; % Relative permittivities of the
dielectrics
Eps1 = Eps0*Epsr1;
Eps2 = Eps0*Epsr2;
Eps3 = Eps0*Epsr3;
Murm = 1; Murl = 1; % Relative permeabilities
Mum = Muo*Murm; Mul = Muo*Murl;

%frequency range
r = 100;
fmax = 10*10^9;
df = fmax/r;
F = (1:df:fmax); %Frequency in Hz

% No of layers
N=101;

%Matrix initialization
A = zeros(2*N+2);
Y = zeros(2*N+2,1);

% Thickness
tm = 1*10^(-6); % thickness of each conducting material layer
tl = 0.2*10^(-4); % thickness of each laminating dielectric layer

for m = 1 : 2 : 2*N
```

```

    a_odd(m) = ((m+1)/2)*tm + ((m-1)/2)*tl;
end

for m = 2 : 2 : 2*N
    a_even(m) = (m/2)*(tm + tl);
end

for k = 1:length(F)
    f = F(k);

% Propagation factors
    ko = 2*pi*f*sqrt(Eps0*Muo); % In air region
    km = 2*pi*f*sqrt(Mum*Eps2)*sqrt(1+j*Sigma/(2*pi*f*Eps2)); % In the conducting material
    kl = 2*pi*f*sqrt(Mul*Eps3); % In the laminating dielectric

%Matrix components
    A(1,1) = -1; A(1,2) = 1; A(1,3) = 1;
    A(2,1) = ko/(2*pi*f*Muo); A(2,2) = km/(2*pi*f*Mum); A(2,3) = -
    km/(2*pi*f*Mum);

    for m = 1 : N

        if (mod(m,2) == 1) %if m is odd
            for q = 3:4:(2*N-3)
                A(q,q-1) = exp(-j*km*a_odd(q-(q+1)/2));
                A(q,q) = exp(j*km*a_odd(q-(q+1)/2));
                A(q,q+1) = - exp(-j*kl*a_odd(q-(q+1)/2));
                A(q,q+2) = - exp(j*kl*a_odd(q-(q+1)/2));
            end
            for q = 4:4:(2*N-2)
                A(q,q-2) = (km/(2*pi*f*Mum))*exp(-j*km*a_odd(q-
(q+2)/2));
                A(q,q-1) = -(km/(2*pi*f*Mum))*exp(j*km*a_odd(q-
(q+2)/2));
                A(q,q) = -((kl/(2*pi*f*Mul)))*exp(-j*kl*a_odd(q-
(q+2)/2));
                A(q,q+1) = ((kl/(2*pi*f*Mul)))*exp(j*kl*a_odd(q-
(q+2)/2));
            end

            elseif (mod(m,2) == 0) %if m is even
                for q = 5:4:(2*N-1)
                    A(q,q-1) = exp(-j*kl*a_even(q-(q+1)/2));
                    A(q,q) = exp(j*kl*a_even(q-(q+1)/2));
                    A(q,q+1) = - exp(-j*km*a_even(q-(q+1)/2));
                    A(q,q+2) = - exp(j*km*a_even(q-(q+1)/2));
                end
                for q = 6:4:2*N
                    A(q,q-2) = (kl/(2*pi*f*Mul))*exp(-j*kl*a_even(q-
(q+2)/2));
                    A(q,q-1) = -(kl/(2*pi*f*Mul))*exp(j*kl*a_even(q-
(q+2)/2));
                    A(q,q) = -((km/(2*pi*f*Mum)))*exp(-j*km*a_even(q-
(q+2)/2));

```

```

        A(q,q+1) = ((km/(2*pi*f*Mum)))*exp(j*km*a_even(q-
(q+2)/2));
    end

    q = 2*N + 1;
    A(q,q-1) = exp(-j*km*a_odd((q+1)/2-1));
    A(q,q) = exp(j*km*a_odd((q+1)/2-1));
    A(q,q+1) = - exp(-j*ko*a_odd((q+1)/2-1));

    q = 2*N + 2;
    A(q,q-2) = (km/(2*pi*f*Mum))*exp(-j*km*a_odd((q/2)-1));
    A(q,q-1) = -(km/(2*pi*f*Mum))*exp(j*km*a_odd((q/2)-1));
    A(q,q) = - (ko/(2*pi*f*Muo))*exp(-j*ko*a_odd((q/2)-1));

    end

end

Y(1) = 1; Y(2) = ko/(2*pi*f*Muo);

X = A;
C = X\Y;
D(k)=C(1);
E(k)=C(2*N+2);;
end

R = (abs(D)).^2;
T = (abs(E)).^2;

% POWER BALANCE
Power = 1/(2*sqrt(Muo/Epso)) - R/(2*sqrt(Muo/Epso)) -
T/(2*sqrt(Muo/Epso)); %Losses
plot(F, Power, 'red*')
grid on
Hold on
title(['Power loss vs. Frequency']);
xlabel('Frequency (Hz)');
ylabel('Power Loss');

```


Appendix D: Skin Depth for Different Conductivity

Skin depth is calculated based on the equation below:

$$\delta = \frac{1}{\sqrt{\pi f \mu \sigma}} \quad (\text{C.1})$$

Table D.1: Skin depths for frequencies with $\sigma = 10$

Frequency (GHz)	Skin depth (m)
1	5.03×10^{-3}
2	3.56×10^{-3}
5	2.25×10^{-3}
10	1.6×10^{-3}

Table D.2: Skin depths for frequencies with $\sigma = 10^2$

Frequency (GHz)	Skin depth (m)
1	1.6×10^{-3}
2	1.13×10^{-3}
5	0.71×10^{-3}
10	0.5×10^{-3}

Table D.3: Skin depths for frequencies with $\sigma = 10^3$

Frequency (GHz)	Skin depth (m)
1	5.03×10^{-4}
2	3.56×10^{-4}
5	2.25×10^{-4}
10	1.6×10^{-4}

Table D.4: Skin depths for frequencies with $\sigma = 10^4$

Frequency (GHz)	Skin depth (m)
1	1.6×10^{-4}
2	1.13×10^{-4}
5	0.71×10^{-4}
10	0.5×10^{-4}

Table D.5: Skin depths for frequencies with $\sigma = 10^5$

Frequency (GHz)	Skin depth (m)
1	5.03×10^{-5}
2	3.56×10^{-5}
5	2.25×10^{-5}
10	1.6×10^{-5}

Table D.6: Skin depths for frequencies with $\sigma = 10^6$

Frequency (GHz)	Skin depth (m)
1	1.6×10^{-5}
2	1.13×10^{-5}
5	0.71×10^{-5}
10	0.5×10^{-5}

Table D.7: Skin depths for frequencies with $\sigma = 10^7$

Frequency (GHz)	Skin depth (m)
1	5.03×10^{-6}
2	3.56×10^{-6}
5	2.25×10^{-6}
10	1.6×10^{-6}

Appendix E: Reduction in Antenna Gain Due to Mismatch Loss

Return loss is a measure of how much of the incident energy is reflected back to the input due to impedance mismatch. Lower S_{11} values for the return loss indicates better impedance match. If the antenna is not well matched to the input circuit, then it suffers from the mismatch loss, which is the same effect as reducing the antenna gain [79]. If the specified return loss is 9.5 dB, the mismatch loss is 0.5 dB. This has the effect of reducing the antenna gain by 0.5 dB. The table below shows the commonly specified return losses and their corresponding mismatch losses, and therefore the reduction in gain:

Table E: Reduction in gain due to mismatch loss

Return loss (dB)	Mismatch loss (dB)	Reduction in gain (dB)
14	<0.2	<0.2
9.5	0.5	0.5
6	1.25	1.25
4	2.2	2.2

References

- [1] K. Hirasawa and M. Haneishi, "*Analysis, design and measurement of small and low-profile antennas*", Artech House, Boston, MA, USA, 1992.
- [2] R. Garg, P. Bhartia, I. J. Bahl, A. Ittipibon, "*Microstrip antenna design handbook*", Artech House, Norwood, MA, 2001.
- [3] P. S. Hall, and J. R. James, "*Handbook of microstrip antennas*", Peter Peregrinus, London, 1989.
- [4] A. K. Skrivervik, J. F. Zurcher, O. Staub and J. R. Mosig, "PCS antenna design: the challenge of miniaturization", *IEEE Antennas Propagat. Mag.*, vol. 43, no. 4, August 2001, pp. 12-23.
- [5] P. M. Bafrooei, and L. Shafai, "Characteristics of single- and double-layer microstrip square ring antennas", *IEEE Trans. Antennas Propagat.*, vol. 47, no. 10, October 1999, pp. 1633–1639.
- [6] R. Garg and V. S. Reddy, "Edge feeding of microstrip ring antennas", *IEEE Trans. Antennas Propagat.*, vol. 51, no. 8, 2003, 1941-1946.
- [7] V. Palanisamy, and R. Garg, "Analysis of circularly polarized square ring and crossed strip microstrip antennas", *IEEE Trans. Antennas Propagat.*, vol. 34, no. 12, November 1986, pp. 1340–1346.
- [8] R. Q. Lee, and K. F. Lee, "Characteristics of a two-layer electromagnetically coupled rectangular patch antenna", *Electron. Lett.*, vol. 23, no. 20, September 1987, pp. 180–181.

- [9] F. E. Gardiol, J. F. Zurcher, "Broadband patch antennas- a SSFIP update", *Proc. 1996 IEEE AP-S Intl. Symp.*, Baltimore, MD, vol. 1, July 1996, pp. 2-5.
- [10] G. Kumar and K.P. Ray, "*Broadband microstrip antennas*", Artech House, Norwood, MA, 2003.
- [11] J. F. Zurcher, and F. E. Gardiol, "*Broadband patch antennas*", Artech House, Norwood, MA, USA, 1995.
- [12] R. B. Waterhouse, "Design of probe-fed stacked patches", *IEEE Trans. Antennas Propagat.*, vol. 47, no. 12, December 1999, pp. 1780-1784.
- [13] R. B. Waterhouse, "Stacked patches using high and low dielectric constant material combinations", *IEEE Trans. Antennas Propagat.*, vol. 47, no. 12, December 1999, pp. 1767-1771.
- [14] J. L. Drewniak, and P. E. Mayes, "ANSERLIN: A broad-band, low-profile, circularly polarized antenna", *IEEE Trans. Antennas Propagat.*, vol. 37, no. 3, March 1989, pp. 281-288.
- [15] K. Fujimoto, and J. R. James, Eds., "*Mobile antenna systems handbook*", 2nd Ed., Artech House, Boston, MA, USA, 2001.
- [16] K. L. Wong, "*Compact and broadband microstrip antennas*", John Wiley & Sons, Inc., New York, NY, USA, 2002.
- [17] W. S. Chen, C. K. Wu, and K. L. Wong, "Single-feed square-ring microstrip antenna with truncated corners for compact circular polarization operation", *Electron. Lett.*, vol. 34, no. 11, May 1998, pp. 1045-1047.

- [18] W. S. Chen, C. K. Wu, and K. L. Wong, "Square ring microstrip antenna with a cross strip for compact circular polarization operation", *IEEE Trans. Antennas Propagat.*, vol. 47, no. 10, October 1999, pp. 1566–1568.
- [19] I. Saha, and S. K. Chowdhury, "Experiments on impedance and radiation properties of concentric microstrip ring resonators", *Electron. Lett.*, vol. 31, no. 6, March 1995, pp. 421-422.
- [20] I. S. Misra, and S. K. Chowdhury, "Study of impedance and radiation properties of a concentric microstrip triangular-ring antenna and its modeling techniques using FDTD method", *IEEE Trans. Antennas Propagat.*, vol. 46, no. 4, April 1998, pp. 531-537.
- [21] A. K. Bhattacharyya, and L. Shafai, "A wider band microstrip antenna for circular polarization", *IEEE Trans. Antennas Propagat.*, vol. 36, no. 2, February 1988, pp. 157-163.
- [22] S. -S. Oh, and L. Shafai, "Investigation into the cross-polarization of loaded microstrip ring antennas", *Proc. 2005 IEEE AP-S Intl. Symp., USNC/URSI Meeting*, Washington, D. C., USA vol. 1A, July 3-8, 2005, pp. 243 – 246.
- [23] S. -S. Oh, and L. Shafai, "Antenna miniaturization using open square-ring microstrip geometries", *Electron. Lett.*, vol. 42, no. 9, April 2006, pp. 500-502.
- [24] S.-S. Oh, and L. Shafai, "Compact open-ring microstrip antennas fed by capacitive coupling", *Proc. 2005 Intl. Symp. Antennas Propagat. (ISAP2005)*, Seoul, Korea, August, 2005, pp. 109-112.
- [25] A. M. Clogston, "Reduction of skin effect losses by use of laminated conductors", *Proc. IRE*, vol. 39, no.7, July 1951, pp. 767 – 782.

- [26] R. F. Pease, and O.-K. Kwon, "Physical limits to the useful packaging density of electronic systems", *IBM J. of Res. Develop.*, vol. 32, September 1988, pp. 636 – 646,.
- [27] S. I. Latif, and L. Shafai, "Dual-layer square-ring antenna (DLLSRA) for circular polarization", *Proc. 2005 IEEE AP-S Intl. Symp.*, Washington, D. C., USA, vol. 2A, July, 2005, pp. 525-528.
- [28] S. I. Latif, and L. Shafai, "Circular polarization from dual-layer square-ring miniaturized microstrip antennas", *Canadian Jour. Elec. Comp. Eng.*, under review.
- [29] S. I. Latif, and L. Shafai, "Hybrid perturbation scheme for wide angle circular polarisation of stacked square-ring microstrip antennas", *Electron. Lett.*, vol. 43, no. 20, September 2007, pp. 1065-1066.
- [30] S. I. Latif, and L. Shafai, "Microstrip square-ring antenna with capacitive feeding for multi-frequency operation", *Proc. 2008 IEEE AP-S Intl. Symp.*, July 2008, San Diego, CA, USA.
- [31] M. Sanad, "Effects of shorting posts on short circuit microstrip antennas", *Proc. 1994 IEEE AP-S Intl. Symp.*, Seattle, Washington, USA, vol. 2, June 1994, pp. 794-797.
- [32] R. B. Waterhouse, "Small microstrip patch antenna", *Electron. Lett.*, vol. 31, no. 8, April 1995, pp. 604-605.
- [33] R. B. Waterhouse, S. D. Targonski and D. M. Kokotoff, "Design and performance of small printed antennas", *IEEE Trans. Antennas Propagat.*, vol. 46, no. 11, November 1998, pp. 1629-1633.
- [34] J. S. McLean, "A re-examination of the fundamental limits on the radiation Q of electrically small antennas", *IEEE Trans. Antennas Propagat.* vol. 44, no. 5, May 1996, pp. 672-675.

- [35] H. A. Wheeler, "Fundamental limitations of small antennas", *Proc. IRE (IEEE)*, vol. 35, December 1947, pp. 1479-1484.
- [36] R. C. Johnson, "Antenna engineering handbook", 3rd Edition, McGraw-Hill Inc., USA, 1994.
- [37] H. A. Wheeler, "Small antennas", *IEEE Trans. Antennas Propagat.* vol. 23, no. 4, July 1975, pp. 462 - 469.
- [38] L. J. Chu, "Physical limitations of omni-directional antennas", *J. Appl. Phys.*, vol. 19, 1948, pp. 1163 - 1175.
- [39] H. G. Schantz, "Introduction to ultra-wideband antennas", *Proc. 2003 IEEE Conf. Ultra Wideband Systems and Technologies (UWBST)*, Reston, VA, USA, 16-19 November 2003, pp. 1 - 9.
- [40] R. F. Harrington, "Effects of antenna size on gain, bandwidth, and efficiency", *J. Res. National Bureau of Standards — D, Radio Propagation*, vol. 64, no. 1, January-February 1960, pp. 1—12.
- [41] R. C. Hansen, "Electrically small, superdirective, and superconducting antennas", John Wiley and Sons Inc., NJ, USA, 2006.
- [42] R. E. Collin and S. Rothschild, "Evaluation of antenna Q", *IEEE Trans. Antennas Propagat.*, vol. 12, no. 1, January 1964, pp. 23–27.
- [43] R. L. Fante, "Quality factor of general idea antennas", *IEEE Trans. Antennas Propagat.*, vol. 17, no. 2, March 1969, pp. 151–155.
- [44] W. Geyi, "A method for the evaluation of small antenna Q", *IEEE Trans. Antennas Propagat.*, vol. 51, no. 8, August 2003, pp. 2124–2129.

- [45] G. A. Thiele, Phil L. Detweiler, and Robert P. Penno, "On the lower bound of the radiation Q for electrically small antennas", *IEEE Trans. Antennas Propagat.*, vol. 51, no. 6, June 2003, pp. 1263-1268.
- [46] A. D. Yaghjian and S. R. Best, "Impedance, bandwidth, and Q of antennas", *IEEE Trans. Antennas Propagat.*, vol. 53, no. 4, April 2005, pp. 1298–1324.
- [47] S. Collardey, A. Sharaiha, and K. Mahdjoubi, "Calculation of small antennas quality factor using FDTD method", *IEEE Antennas Wireless Propagat. Lett.*, vol. 5, 2006, pp. 191-194.
- [48] W. J. Bergman and F. V. Schultz, "The circular traveling-wave antenna", *IRE Int. Conv. Rec.*, vol. 3, pt. 1, 1955, pp. 40–50.
- [49] Y. S. Wu and F. J. Rosenbaum, "Mode for microstrip ring resonator", *IEEE Trans. Microwave Theory Tech.*, vol. MTT-21, no. 7, July 1973, pp. 487.
- [50] I. J. Bahl, S. S. Stuchly, and M. A. Stuchly, "A new microstrip radiator for medical application", *IEEE Trans. Microwave Theory Tech.*, vol. MTT-28, p. 1464, pp. 1464–1468, Dec. 1980.
- [51] V. Palanisamy, and R. Garg, "Analysis of arbitrarily shaped microstrip patch antennas using segmentation technique and cavity model", *IEEE Trans. Antennas Propagat.*, vol. 34, no. 10, pp. 1208–1213, Oct. 1986.
- [52] G. Mayhew-Ridgers, J. W. Odendaal, and J. Joubert, "New feeding mechanism for annular-ring microstrip antenna", *Electron. Lett.*, vol. 36, no. 7, March 2000, pp. 605–606.
- [53] J. S. Row, "Design of square-ring microstrip antenna for circular polarisation", *Electron. Lett.*, vol. 40, no. 2, January 2004, pp. 93-95.

- [54] K. L. Chung, and A. S. Mohan, "A systematic design method to obtain broadband characteristics for singly-fed electromagnetically coupled patch antennas for circular polarization", *IEEE Trans. Antennas Propagat.*, vol. 51, no. 12, December 2003, pp. 3239-3248.
- [55] R. Q. Lee, T. Talty, and K. F. Lee, "Circular polarisation characteristics of stacked microstrip antennas", *Electron. Lett.*, vol. 26, no. 25, December 1990, pp. 2109-2110.
- [56] W. L. Langston, and D. R. Jackson, "Impedance, axial-ratio, and receive-power bandwidths of microstrip antennas", *IEEE Trans. Antennas Propagat.*, vol. 52, no. 10, October 2004, pp. 2769-2773.
- [57] M. A. Sultan, "The mode features of an ideal-gap open-ring microstrip antenna", *IEEE Trans. Antennas Propagat.*, vol. 37, no. 2, February 1989, pp. 137-142.
- [58] T. Teshirogi, M. Tanaka, and W. Chujo, "Wideband circularly polarized array antenna with sequential rotations and phase shift of elements", *Proc. Intl. Symp. Antennas Propagat. (ISAP)*, August 1985, pp. 117-120.
- [59] GPS Modernization, "http://www.faa.gov/about/office_org/headquarter_offices/ato/service_units/techops/navservices/gnss/gps/policy/modernization/index.sfm"
- [60] A.J. Van Dierendonck, C. Hegarty, W. Scales, and S. Ericson, "Signal specification for the future GPS civil signal at L5", *Proceedings of ION Annual Meeting 2000*, San Diego, CA, June 26-28, 2000. pp. 232-241.
- [61] S. S. Jan, "Analysis of a three-frequency GPS/WAAS receiver to land an airplane", *Proc. 15th International Technical Meeting of the Institute of Navigation*, ION GPS 2002, September 24 - 27, 2002, Portland, Oregon, pp. 2576 - 2586.

- [62] D.M. Pozar and S.M. Duffy, "A dual-band circularly polarized aperture coupled stacked microstrip antenna for global positioning satellite", *IEEE Trans. Antennas Propagat.*, vol. 45, no 11, November 1997 pp.1618 – 1625.
- [63] C. M. Su and K. L. Wong, "A dual-band GPS microstrip antenna", *Microwave Opt. Tech. Letters*, vol.33, no. 4, April 2002, pp.238-240.
- [64] X. F. Peng, S. S. Zhong, S. Q. Xu and Q. Wu, "Compact dual-band GPS microstrip Antenna", *Microwave Opt. Tech. Letters*, vol. 44, no. 1, November 2005, pp. 58-61, 2005.
- [65] L. Boccia, G. Amendola, and G. D. Massa, "A shorted elliptical patch antenna for GPS applications", *IEEE Antennas Wireless Propagat. Letters*, vol. 2, no.1, 2003, pp. 6 – 8.
- [66] B. Rama Rao, M. A. Smolinski, C. C. Quach, and E. N. Rosario, "Triple-band GPS trap-loaded inverted L antenna array", *Microwave Opt. Tech. Letters*, vol. 38, no. 1, May 2003, pp. 35 – 37.
- [67] Y. Zhou, G. Kiziltas, S. Koulouridis, and J. L. Volakis, "A miniature four-arm antenna for tri-band GPS applications", *Proc. 2005 IEEE AP-S Intl. Symp.*, Washington, D. C., USA vol. 3A, July 3-8, 2005, pp. 872- 875.
- [68] Y. Zhou, C.-C. Chen, and J. L. Volakis, "Dual band proximity-fed stacked patch antenna for tri-band GPS applications", *IEEE Trans. Antennas Propagat.*, vol. 55, no. 1, January 2007, pp. 220–223.
- [69] Y. Zhou; C. -C. Chen, J. L. Volakis, "Single-fed circularly polarized antenna element with reduced coupling for GPS arrays", *IEEE Trans. Antennas Propagat.*, vol. 56, no 5, May 2008, pp.1469 – 1472.

- [70] S. I. Latif, and L. Shafai, "Gap-loaded microstrip square ring for antenna miniaturization", *Proc. 12th Intl. Symp. Antenna Tech. Applied Electromagnetics (ANTEM)*, Montreal, QC, Canada, July 2006, pp. 49-52.
- [71] S. I. Latif, and L. Shafai, "Investigation on probe-fed open-ring microstrip antenna for miniaturization", *Microwave Opt. Tech. Lett.*, vol. 48, no. 11, November 2006, pp. 2175-2179.
- [72] J. A. Stratton, "Electromagnetic theory", McGraw-Hill Inc., New York, USA, 1941.
- [73] D. K. Cheng, "Field and wave electromagnetics", Addison-Wesley, Reading, MA, 1989.
- [74] J. A. Kong, "Electromagnetic wave theory", EMW Publishing, Cambridge, MA, USA, 2000.
- [75] R. F. Harrington, "Time-harmonic electromagnetic fields", McGraw-Hill Inc., New York, NY, USA, 1961.
- [76] S. I. Latif, C. Shafai, and L. Shafai, "Reduction in ohmic loss of small microstrip antennas using multiple copper layers ", *Proc. 2006 IEEE AP-S Intl. Symp.*, July 9-14, 2006, Albuquerque, NM, USA, pp. 1625-1628.
- [77] S. I. Latif, and L. Shafai, "Gain enhancement of small microstrip antennas using multilayered laminated conductors", *Proc. Electromagnetic Theory Symp. (EMTS 2007)*, Ottawa, ON, Canada, July 26-28, 2007.
- [78] H. T. Nguyen, S. Noghianian, and L. Shafai, "Microstrip patch miniaturization by slots loading", *Proc. 2005 IEEE AP-S Intl. Symp*, vol. 1B, July 2005, pp. 215 – 218.
- [79] OBERON Application Note, http://www.oberonwireless.com/WebDocs/Partner_Resources/ImprovingWirelessLANAntennaGainandCoverage_3.pdf.

- [80] C. A. Balanis, "Antenna theory, analysis and design", 3rd Ed., John Wiley and Sons, New York, USA, 2005.